



Michigan Technological University  
*Create the Future* Digital Commons @ Michigan Tech

---

Dissertations, Master's Theses and Master's  
Reports - Open

Dissertations, Master's Theses and Master's  
Reports

---

2008

## Studies of spatial clustering of inertial particles in turbulence

Ewe Wei Saw  
*Michigan Technological University*

Follow this and additional works at: <https://digitalcommons.mtu.edu/etds>

 Part of the [Physics Commons](#)


Copyright 2008 Ewe Wei Saw

---

### Recommended Citation

Saw, Ewe Wei, "Studies of spatial clustering of inertial particles in turbulence", Dissertation, Michigan Technological University, 2008.  
<https://doi.org/10.37099/mtu.dc.etds/118>

Follow this and additional works at: <https://digitalcommons.mtu.edu/etds>

 Part of the [Physics Commons](#)

STUDIES OF SPATIAL CLUSTERING OF INERTIAL PARTICLES IN TURBULENCE

By

EWE WEI SAW

A DISSERTATION

Submitted in partial fulfillment of the requirements

for the degree of

DOCTOR OF PHILOSOPHY

(Physics)

MICHIGAN TECHNOLOGICAL UNIVERSITY

2008

© 2008 Ewe Wei Saw



This dissertation, "Studies of spatial clustering of inertial particles in turbulence",  
is hereby approved in partial fulfillment of the requirements for the degree of DOCTOR  
OF PHILOSOPHY in the field of Physics.

DEPARTMENT:  
Physics

Signatures:

Dissertation Advisor \_\_\_\_\_  
Prof. Raymond A. Shaw

Department Chair \_\_\_\_\_  
Prof. Ravi Pandey

Date \_\_\_\_\_



# Abstract

We present studies of the spatial clustering of inertial particles embedded in turbulent flow. A major part of the thesis is experimental, involving the technique of Phase Doppler Interferometry (PDI). The thesis also includes significant amount of simulation studies and some theoretical considerations. We describe the details of PDI and explain why it is suitable for study of particle clustering in turbulent flow with a strong mean velocity. We introduce the concept of the radial distribution function (RDF) as our chosen way of quantifying inertial particle clustering and present some original works on foundational and practical considerations related to it. These include methods of treating finite sampling size, interpretation of the magnitude of RDF and the possibility of isolating RDF signature of inertial clustering from that of large scale mixing. In experimental work, we used the PDI to observe clustering of water droplets in a turbulent wind tunnel. From that we present, in the form of a published paper, evidence of dynamical similarity (Stokes number similarity) of inertial particle clustering together with other results in qualitative agreement with available theoretical prediction and simulation results. We next show detailed quantitative comparisons of results from our experiments, direct-numerical-simulation (DNS) and theory. Very promising agreement was found for like-sized particles (mono-disperse). Theory is found to be incorrect regarding clustering of different-sized particles and we propose an empirical correction based on the DNS and experimental results. Besides

this, we also discovered a few interesting characteristics of inertial clustering. Firstly, through observations, we found an intriguing possibility for modeling the RDF arising from inertial clustering that has only one (sensitive) parameter. We also found that clustering becomes saturated at high Reynolds number.

# Acknowledgments

This thesis would not be possible without the contributions from many people. Foremost, i would like to thank Dr. Raymond Shaw who has been a wonderful advisor and a good friend. I have greatly enjoyed working with him. Credits also go to him and his children (Ben and Alex) for their help in carrying many bottles of distilled water during the experiments.

Gratitude goes to my research committees, Dr. Jacek Borysow, Dr. Will Cantrell and Dr. Franz Tanner, for their time and efforts in making this thesis better.

Gratitude also goes to the Physics department and its staff which I think are friendly and have made things much easier for the students.

Many thanks go to collaborators who had significantly contributed to the materials in this thesis. This includes Lance Collins, Juan Salazar, Armann Gylfason, Sathyanarayana Ayyalasomayajula, Zellman Warhaft, Patrick Chuang.

I would also like to thank many from whom I had learned from or benefited from significantly in some ways during my years in graduate school. This includes Eli Ochshorn, Evan Variano, Nicole Sharp, Jacob Fugal, Sergiy Gerashchenko, Alexander Kostinski, Haitao Xu, Stephanie Neuscamman, Jennifer Small, Eberhard Boden-



schatz, Hansen Nordsiek, Jiang Lu, Papi Zhong, James Wee, Kah Chun Lau, Chee Huei Lee, Chee Seng Fong, staff of Artium Inc and perhaps more that I had missed.

Lastly I would like to acknowledge the funding agencies: NSF, NASA, Max Planck Institute for Dynamics and Self-Organization, Michigan Tech..

# Contents

<b>Abstract</b>	<b>v</b>
<b>Acknowledgments</b>	<b>vii</b>
<b>List of Figures</b>	<b>xx</b>
<b>List of Tables</b>	<b>xxi</b>
<b>1 Introduction</b>	<b>1</b>
1.1 Fluid Turbulence . . . . .	3
1.2 Inertial particle clustering in turbulent flow . . . . .	6
1.2.1 Theories and quantification of inertial clustering . . . . .	6
1.2.2 Other computational and experimental works . . . . .	10
1.3 Outline . . . . .	10
<b>2 Phase Doppler Interferometry</b>	<b>13</b>
2.1 Background . . . . .	14

2.2	Basic working principles . . . . .	15
2.2.1	Velocity measurement . . . . .	16
2.2.2	Size measurement . . . . .	18
2.3	Our Phase Doppler Interferometer . . . . .	19
2.3.1	The probe body's design . . . . .	21
2.3.2	Slit aperture and measurement volume . . . . .	23
2.3.3	Arrival time accuracy . . . . .	24
2.3.4	Velocity accuracy and range . . . . .	25
2.3.5	Sizing accuracy and range . . . . .	26
2.4	Observing particle clustering with PDI . . . . .	29
<b>3</b>	<b>Radial distribution function (RDF) in application</b>	<b>33</b>
3.1	Definition from basic probability . . . . .	34
3.1.1	Relevance to particle clustering in turbulence . . . . .	36
3.2	Calculating the RDF from a particle field . . . . .	37
3.2.1	Extension to finite interrogation volume . . . . .	40
3.2.2	Sample edge treatment . . . . .	43
3.2.3	Averaging the RDF over many small samples . . . . .	44
3.3	Characteristics of the RDF . . . . .	46
3.3.1	Relation of RDF to scales of clustering . . . . .	46

3.3.2	Inertial clustering and turbulent mixing . . . . .	48
<b>4</b>	<b>The wind tunnel experiment</b>	<b>55</b>
4.1	Background . . . . .	56
4.1.1	Homogenous-isotropic turbulence . . . . .	56
4.1.2	Grid turbulence . . . . .	57
4.2	Experimental setup and methods . . . . .	57
4.2.1	Active grid and turbulence generation . . . . .	58
4.2.2	Droplet generation . . . . .	60
4.2.3	Influence of Sprays on turbulence . . . . .	62
4.2.4	PDI positioning and particle equilibration . . . . .	64
4.3	Data analysis . . . . .	66
4.3.1	Obtaining inter-particle distances from particle arrival times .	66
4.3.2	Calculation of radial distribution function . . . . .	67
4.4	Error analysis . . . . .	68
<b>5</b>	<b>Stokes similarity in inertial clustering (a published paper)</b>	<b>73</b>
5.1	Introduction . . . . .	74
5.2	Experiment . . . . .	78
5.3	Results and Discussion . . . . .	79

5.4	Supplementary: Large scale spatial inhomogeneity of particle density and how to correct for it . . . . .	85
<b>6</b>	<b>Quantitative comparison: experiment, simulation and theory</b>	<b>89</b>
6.1	Direct Numerical Simulation (DNS) . . . . .	91
6.1.1	Simulating the fluid turbulence . . . . .	91
6.1.2	Simulating the particles . . . . .	92
6.2	Results and Discussions . . . . .	95
6.2.1	Comparing DNS results with theory: mono-disperse . . . . .	97
6.2.2	Effects of poly-dispersity on RDF . . . . .	101
6.2.3	Comparing Experimental and DNS results: poly-disperse . . .	104
6.2.4	Relationship between $c_1$ and $c_0$ . . . . .	111
6.2.5	Asymptotic behavior at large Reynolds number . . . . .	113
6.2.6	Comparing DNS with theory: bi-disperse RDF . . . . .	114
6.2.7	Comparing Experiment with DNS: bi-poly-disperse RDF . . .	120
6.3	Further discussions . . . . .	122
6.3.1	Consistency of data between Cornell-1 and Cornell-2. . . . .	122
<b>7</b>	<b>Summary and conclusions</b>	<b>127</b>
<b>Appendix A</b>	<b>Details on characterization of active grid turbulence</b>	<b>131</b>

<b>Appendix B Copyright information</b>	<b>133</b>
---	------------

<b>References</b>	<b>135</b>
-------------------	------------



# List of Figures

2.1	Schematic showing basic operating principle of phase Doppler Interferometry. The off-axis angle ( $\phi$ ) is measured in the ‘major plane’ (normal to the plane of the beams and containing the main axis). . . . .	16
2.2	Particles as a lenses that project the measurement volume fringes onto the detectors. Figure from Chuang et al. (2008). For copyright information, see Appendix B. . . . .	19
2.3	Two photos showing the Artium flight-PDI. Panel (a) shows the instrument mounted vertically onboard a research aircraft. Panel (b) shows the laser beams scatter off small water droplets. The beams emerge from the upper arm, The scattered light collected through the window of the lower arm and is sensed by three photo-detectors(internal). Panel (c) Front view of the two arms and the rough location of the view volume. The instrument body is 28 x 56 x 6.6 cm; each arm is 30 cm long and 4 cm in diameter; the arms are 15 cm apart. Figure from Chuang et al. (2008). For copyright information, see Appendix B. . .	22
2.4	Truncated measurement volume resulting from the used of slit aperture (light gray area). Particle trajectories are into the page, detectors are located far away (not shown) downward and to the right. $l'_s$ is the magnified slit width. . . . .	24



3.1	Caricature of a one dimensional particle field made up of randomly distributed blocks of particles (without overlap). All blocks has the same size (say $b$ ) and within each block, particles are uniform-randomly distributed. . . . .	47
4.1	A schematic (not to scale), showing the experimental setup. Figure from supplementary material of Saw et al. (2008). . . . .	57
4.2	Picture showing the active grid and the configuration of the droplet sprays. Figure obtained from (Gylfason, 2006), courtesy of the author (See Appendix B). . . . .	59
4.3	Probability density function of water droplets generated by the spray nozzles. The broader distribution (blue) is obtained when the water/air pressures are is set to 32/32.5 psi ( $\pm 0.5$ psi). This setting was used in works whose results will discussed in Chap. 5 (Cornell-1). The other distribution (green) that has smaller drops corresponds to condition of water/air pressures equals 40/35 psi and was used in works to be presented in Chap 6 (Cornell-2). . . . .	61
4.4	Energy spectra of turbulence at $X=5\text{m}$ , fan-speed=20Hz obtained using several different methods (via Hot-wire anemometry, phase Doppler interferometry, etc). . . . .	63
5.1	(color online) $\eta(r)$ versus $\hat{r} (\equiv r/r_k)$ with error bars of $2\sigma_{\eta(r)}$ , and with $\eta(r)$ parameterized by $St$ from experiment 3m30Hz. Consistent with theoretical expectations, $\eta(r)$ increases in magnitude with increasing Stokes number in the dissipation range. Each line is $\eta(r)$ calculated from droplets within the specified range of $St$ (from bottom to top corresponding to successively larger $St$ ). The errors are evaluated as $2\sigma_{\eta(r)}$ (details in text) . . . . .	81

5.2	(color online) Stokes-similarity results shown in two panels for clarity. <b>Left:</b> $St$ -similarity for droplets with $St=0.01-0.3$ (circles) and $St=0.7-1.1$ (triangles). Plots for other $St$ groups from ig. 5.1, 3m30Hz, are shown in the background for comparison. The marker colors represent $\eta(r)$ from different experiments (blue=3m20Hz, green=3m30Hz, red=5m20Hz, cyan=5m30Hz). <b>Right:</b> $St$ -similarity for $St=0.3-0.7$ (circles) and $St=1.1-1.5$ (triangles). . . . .	82
5.3	Error-bar plots of RDF ( $\equiv \eta(r) + 1$ ) for $St = 0.1 \rightarrow 0.5$ from various experimental runs (in logarithmic axes). Colors represent different experimental runs: purple is 3m25Hz; green is 3m30Hz; black is 3m40Hz; gold is 5m20Hz; cyan is 5m25Hz; red is 5m40Hz. In addition, to aid differentiation, results from 3 $m$ and 5 $m$ downstream are marked as triangles and circles respectively. The present of a ‘shoulder region’ at $r/r_k \geq 50$ is likely the result of large scale inhomogeneity in the spatial distribution of droplets (see text). . . . .	86
5.4	Error-bar plots of corrected RDF for $St = 0.1 \rightarrow 0.5$ from various experimental runs (in logarithmic axes). Each RDF is multiplied by a constant factor such that its values at $r/r_k \simeq 80$ are equal to one. Colors represent different experimental runs: purple is 3m25Hz; green is 3m30Hz; black is 3m40Hz; gold is 5m20Hz; cyan is 5m25Hz; red is 5m40Hz. In addition, to aid differentiation, results from 3 $m$ and 5 $m$ downstream are marked as triangles and circles respectively. The RDF’s show clear evidence of Stokes similarity in their average steepness at small scales ( $r/r_k \leq 10$ ). . . . .	87
6.1	Snapshots of particle fields from the DNS taken at the same instance in (simulated) time and in the same spatial sub-domain (a ‘slice’ of $3r_k$ thick and $2\pi \times 2\pi$ across). Left, particles with $St=0.1-0.4$ ; Right, particles with $St=0.5-0.8$ . . . . .	96

6.2	Quasi mono-disperse RDF calculated from 3D particle positions. Individual RDF represent Stokes number of (increasing from bottom top): 0.04, 0.2, 0.36, 0.52, 1.0. . . . .	97
6.3	Clustering exponent ( $c_1$ ) versus Stokes number ( $St$ ). Blue, DNS; Cyan, theory. . . . .	99
6.4	Poly-disperse RDF on logarithmic axes. Each $g_{3d}(r)$ is based on particles with Stokes number within $(St_{mid} \pm \Delta St)$ where $St_{mid} = 0.4$ . Colors represent different $St$ -bin widths, $\Delta St$ , increasing from top to bottom. The observed trend is representative of results using other values of $St_{mid}$ . The first point of the top two curves are thrown due to poor statistical convergence. . . . .	102
6.5	Power-law exponent, $c_1$ , as a function of $\Delta St$ for $St_{mid} = 0.4$ . Red line is a linear fit on points satisfying $\Delta St \leq 0.08$ . Trend representative of results using other values of $St_{mid}$ . . . . .	104
6.6	Poly-disperse RDF on logarithmic axes. Colors represent different $St$ ranges. $St$ increases from bottom to top: blue is $St = 0.01 \rightarrow 0.21$ ; green, $St = 0.09 \rightarrow 0.29$ ; red, $St = 0.25 \rightarrow 0.45$ . The error-bar plots are experimental results $[g_{1d}(r)]$ ; dotted lines, $g_{3d}(r)$ with flat $St$ -bins; dashed lines, $g_{3d}(r)$ with corrected (matching experiment's) $St$ -bins; solid lines, $g_{1d}(r)$ with corrected $St$ -bins. The experimental plots are vertically shifted so that only their trends or slopes are compared (see text). . . . .	106
6.7	Probability distribution function of droplet Stokes number for experiment 5m20Hz whose result is discussed in this section. Black line is a log-normal fit. . . . .	107

6.8	Poly-disperse RDF on logarithmic axes. Colors represent different $St$ ranges. $St$ increases from bottom to top: blue is $St = 0.01 \rightarrow 0.21$ ; green, $St = 0.09 \rightarrow 0.29$ ; red, $St = 0.25 \rightarrow 0.55$ ; purple, $St = 0.40 \rightarrow 1.0$ . Open circles with error-bars are experimental results [ $g_{1d}(r)$ ]; Solid lines with error-bars are $g_{1d}(r)$ from DNS (matching experimental $St$ -bins). The experimental plots are vertically shifted so that only their trends or slopes are of absolute significance. . . . .	108
6.9	The average steepness of the (poly-disperse) RDF's in Fig. 6.8, $c_1$ as function of average Stokes number, $\langle St \rangle$ . Blue is the DNS results; cyan, empirical. $c_1$ is obtained by fitting power-law (straight line in logarithmic axes) to RDF in the window of $r/r_k = 2 \rightarrow 10$ , using the same fitting algorithm used for in Fig. 6.3. . . . .	110
6.10	Bi-disperse RDF from DNS, with one Stokes number fixed, $St_1 = 0.40$ , while the other, $St_2$ , varied. <b>Left</b> ) Blue, $St_2 = 0.40$ (mono-disperse); green, $St_2 = 0.34$ ; red, $St_2 = 0.28$ . <b>Right</b> ) Blue, $St_2 = 0.40$ (mono-disperse); cyan, $St_2 = 0.46$ ; purple, $St_2 = 0.52$ . General trend representative of cases at other Stokes numbers studied. . . . .	115
6.11	The normalized flattening scale $r_c/r_k$ versus $St_2 - St_1$ . For each color, $St_1$ is fixed while $St_2$ is varied. Blue, $St_1 = 0.2$ ; red, $St_1 = 0.4$ ; cyan, $St_1 = 0.7$ ; green, $St_1 = 1.0$ . Magenta dashed line is the theoretical prediction ( $5.0  St_2 - St_1 $ ). All $r_c$ 's were obtained by fitting Eq. 6.9 to $g_{12}(r)$ in the window $r/r_k = 0.1 \rightarrow 4$ . . . . .	117
6.12	$c_1$ versus $St_2$ with $St_1$ fixed at various values. Theoretical prediction of linear dependence of $c_1$ on $St_2$ is not correct (see text). . . . .	118

6.13	Bi-polydisperse RDF with $St_1 = 0.2 \rightarrow 0.3$ (fixed). $St_2$ is varied: blue is $St_2 = 0.01 \rightarrow 0.1$ ; red, $St_2 = 0.1 \rightarrow 0.2$ ; purple, $St_2 = 0.2 \rightarrow 0.3$ (mono-disperse); black, $St_2 = 0.3 \rightarrow 0.5$ ; green, $St_2 = 0.5 \rightarrow 1.2$ . Smooth solid lines are from DNS; circles are from experiments (5m20Hz). Statistical error of experimental points are very well represented by the apparent fluctuation in each curve (which become larger at small $r$ ). Top-left and bottom panels show comparison between DNS and experiment (separated for clarity); top-right panel shows only the experimental results. . . . .	121
6.14	Comparing RDF from Cornell-1 and Cornell-2 experiments. All RDF are for $St = 0.1 \rightarrow 0.5$ . Blue solid line is from Cornell-2, 5m20Hz run. The others are from Cornell-1: red is 3m20Hz; cyan, 3m40Hz; green, 5m30Hz. All plots are vertically shifted to match at $r/r_k = 80 \sim 120$ . Note that Cornell 1 and 2 has different drop Stokes distribution (see Fig. 6.15). . . . .	123
6.15	Comparing Stokes number distribution of droplets from Cornell-1, 3m20Hz with that from Cornell-2, 5m20Hz. Alternatively, for size distributions see Fig. 4.3. . . . .	124
6.16	Comparing RDF from Cornell-1 and Cornell-2 experiments. All RDF are for $St = 0.1 \rightarrow 0.5$ . Blue solid line is from Cornell-2, 5m20Hz run. Yellow is from Cornell-1, 5m20Hz. All plots are vertically shifted to match at $r/r_k = 80 \sim 120$ . Note that Cornell 1 and 2 has different drop size distribution (see Fig. 4.3). . . . .	125

# List of Tables

2.1	Table showing the measurement accuracy and dynamic range of our PDI system as claimed by the manufacturer and the results of our own characterization (not always consistent with manufacturer's). Velocity measurement range is variable, velocity accuracy is reported in percent of measurement range. . . . .	25
5.1	Experiment flow parameters, where $R_\lambda$ is the Taylor-scale Reynolds number, $U$ is the mean and $u$ is the rms fluctuation of the flow speed along the wind tunnel. The last 4 rows are the droplet diameters (in $\mu\text{m}$ ) and corresponding gravitational settling parameters, $S_g$ , for the $St$ bins used in the data analysis. . . . .	80
6.1	Turbulence parameters in arbitrary units (except the first and last, which are dimensionless) in this DNS. $R_\lambda$ is the Taylor microscale Reynolds number, $\varepsilon$ the turbulent energy dissipation rate, $u'$ the turbulent r.m.s. velocity, $\nu$ the fluid kinematic viscosity, $L$ the integral length scale, $\lambda = u' \sqrt{15\nu/\varepsilon}$ the Taylor microscale, $r_k$ the Kolmogorov length scale, $T$ the large eddy turnover time, $\tau_k$ the Kolmogorov time scale, $\Delta t$ the fluid time step, $k_{max}$ the maximum resolved wavenumber of the simulation. . . . .	92



# Chapter 1

## Introduction

It is a common observation, for instance when stirring cream in a cup of tea, that turbulence produced by the stirring action would cause the initially inhomogeneous field of cream to become homogeneously mixed. Such mixing ability is, in fact, a hallmark of turbulent flows. In this mixing process, the randomly rotating and stretching fluid motion in turbulence causes the initially simple geometry of the cream field to be distorted and stretched thus increasing the surface area bordering the ‘creamed’ and clear fluid. When this bordering area grows to become large enough, the rate of molecular diffusion across it becomes dominant and the mixture becomes homogeneous down to sub-micrometer scales\* (see e.g. Villermaux et al., 2001). Similar mixing processes are ubiquitous in nature, such as in mixing of smokestack plumes, pollutants

---

\*but still larger than the scales at which the continuum approximation breaks down.



in turbulent rivers and so on.

One might then expect that the same situation occurs in turbulent atmospheric clouds. Mixing certainly occurs in clouds, however we are in for a surprise. Let us restrict ourselves to the simplest case of liquid clouds. The main theme of this thesis is to show that the distribution of water droplets is in fact, not uniform at small scales ( $\lesssim 10^{-2} m$ ) and to study this clustering phenomenon.

The key to understanding this clustering phenomenon is the inertia of the particles. Unlike the ‘cream’ discussed earlier, which is made of particles with size comparable to molecular scales, water droplets have finite size and have a much higher mass-density than the surrounding fluid. Thus while the former is passively advected by the fluid, and its motion at any time mimics that of the local fluid motion, the latter (inertial particle) may de-correlate from the advecting fluid motion due to its inertia alone (neglecting gravity etc). Currently, it is generally accepted that this inertial de-correlation leads to the clustering of inertial particles in turbulent flow at fine scales (comparable to the smallest structures of turbulence motion).

This phenomenon, referred to in the literature either as inertial clustering or preferential concentration, is of course not restricted only to clouds but applies to many particle laden, unsteady flows such as fuel droplets in combustion engines, dust particles in planet forming regions in astrophysics (Cuzzi et al., 2001) and so on. Inertial clustering may be important for understanding the dynamics of such systems.

For instance, it has been proposed that inertial clustering may lead to increased collision rate of water droplets in clouds, which may help explain the anomalous short time of rain formation (Pinsky and Khain, 1997; Falkovich et al., 2002; Shaw, 2003).

This thesis focuses on the fundamental investigation of inertial clustering, specifically its multi-scale nature and how it depends on dynamical parameters of the fluid and particles ( $St$ ,  $Re$ ,  $S_g$ , to be defined later on). We will present mainly experimental studies, a significant portion of simulation effort and some theoretical considerations. A detailed outline can be found at the end of this chapter.

## 1.1 Fluid Turbulence

This thesis concerns itself with the type of fluid motion that could accurately model many fluid dynamical phenomena in our atmosphere, oceans, rivers and many industrial and domestic flows. In technical terms this is the motion of an incompressible Newtonian fluid and its equation of motion is the Navier-Stokes equation coupled by the (incompressible) continuity equation:

$$\begin{aligned}\frac{\partial \mathbf{u}}{\partial t} + \mathbf{u} \cdot \nabla \mathbf{u} &= -\nabla P + \frac{1}{Re} \nabla^2 \mathbf{u}, \\ \nabla \cdot \mathbf{u} &= 0,\end{aligned}\tag{1.1}$$

where the Navier-Stokes equation is shown in its non-dimensional form with  $\mathbf{u}(\mathbf{x}, t)$  as the fluid velocity field and  $P(\mathbf{x}, t)$  is the fluid pressure field.  $Re$  is the (dimensionless) Reynolds number defined from the characteristic scales of the problem at hand (which were also used to non-dimensionalize the equations):

$$Re = UL/\nu, \quad (1.2)$$

where  $U$  is the characteristic velocity scale;  $L$ , the characteristic length scale and  $\nu$  is the fluid's kinematic viscosity. A closed problem is obtained when the appropriate initial and boundary conditions are imposed. Kinetic energy needed to drive the flow can be included in the boundary conditions (e.g. via jet or fan).

The Reynolds number which can be interpreted as the ratio of the flow's inertial energy to the fluid viscous dissipation, is an important quantity that characterizes the nature of the fluid motion. When Reynolds number is very high,  $Re \sim \mathcal{O}(10^3)$ , the fluid motion becomes turbulent and has the general characteristic of being chaotic and solenoidal (having many vortices).

Alternatively, the Reynolds number based on the Taylor micro-scale,  $R_\lambda$ , is used when studying the small scales of turbulence.  $R_\lambda$  can be defined as:

$$R_\lambda = u' \lambda / \nu, \quad (1.3)$$

where  $u'$  is the root mean square fluctuation of the fluid velocity and  $\lambda$  is the Taylor micro (length) scale which is defined as:

$$\lambda = u' \sqrt{15\nu/\varepsilon}, \quad (1.4)$$

where  $\varepsilon$  is the average dissipation rate of kinetic energy in the fluid (into heat) and other quantities are as defined previously. These two versions of Reynolds number can be roughly related via:

$$Re = 0.15 R_\lambda^2. \quad (1.5)$$

as derived in Pope (2000).

Turbulent flows can be viewed, through the paradigm of Fourier analysis, as a compilation of unsteady fluid motions on a wide range of length scales. Following this picture, an energy cascade model for turbulence was proposed (see e.g. Tennekes and Lumley, 1972), where the largest scales of motion receive kinetic energy from the forcing mechanism and this energy is cascaded to a long series of smaller scales. The cascade mechanism is thought to be due to inviscid instability in which large vortical structures (eddies) become unstable thus breaking up into smaller eddies. At the smallest scale of turbulent motion, viscosity becomes dominant and kinetic energy is dissipated into heat. Kolmogorov (1941) presented a theory along this energy cascade picture that would become important in the foundation of turbulence research. In this, he assumes that the smallest scales of turbulence are universal and do not depend

on the specifics of the large scale forcing (the ‘memory’ of the large scales is lost in the random nonlinear cascade). It is then deduced that the small scale motions are fully governed by the fluid viscosity and the kinetic energy dissipation rate per unit mass of the fluid,  $\varepsilon$ . With this Kolmogorov arrives at a measure of the smallest scales of motion:

$$r_k = (\nu^3/\varepsilon)^{1/4}, \quad (1.6)$$

while similar expressions for the velocity scale,  $v_k$ , and time scale,  $\tau_k$ , can be obtained in terms of  $\nu$  and  $\varepsilon$  via dimensional analysis. The Reynolds number, in this context, gives a measure of the separation between the energy injection scale ( $L$ ) and the Kolmogorov scale ( $r_k$ ).

## 1.2 Inertial particle clustering in turbulent flow

### 1.2.1 Theories and quantification of inertial clustering

It has been proposed that inertial clustering of particles in turbulence is the result of particles being centrifuged out of regions of high fluid vorticity (highly rotating) as a result of their inertia and thus preferentially concentrating in the regions of high strain. In fact, evidence of inertial particles preferentially concentrating in regions of low vorticity and high strain is abundant (see e.g. Maxey, 1987; Eaton and Fessler,

1994).

However, later simulation studies (e.g. Reade and Collins, 2000; Chun et al., 2005), found that inertial clustering may be strong even at scales much smaller than the scales of turbulent vortices (Kolmogorov length scale). The general consensus now is that the radial distribution function (RDF), a scale resolving measure of particle clustering (to be described in Chap. 3), continues to grow with the inverse of spatial scales in a manner satisfying a power-law down to scales  $10^3$  times smaller than Kolmogorov length scale:

$$g(r) = c_0(r_k/r)^{c_1}, \quad (1.7)$$

where  $g(r)$  is the RDF,  $r_k$  is the Kolmogorov length scale and  $r$  is the spatial correlation scale. In this thesis, we shall call  $c_0$  the power-law pre-factor (or simply pre-factor) and  $c_1$  the power-law exponent (or clustering exponent). This observation called into question the completeness of the vortex-ejection picture of inertial clustering since it is not obvious how the sub-Kolmogorov-scale clustering can be fully explained by the super-Kolmogorov-scale vortical structure of turbulence.

Following that, theoretical attempts have been made to reproduce this power-law scaling of the RDF (or the equivalent) by Balkovsky et al. (2001); Zaichik and Alipchenkov (2003); Chun et al. (2005). These studies performed a perturbative expansion about a fluid particle trajectory with the particle inertia serving as the small parameter in order to obtain the clustering statistics of inertial particles. The

essential result was that in the limit of  $St \ll 1$ ,

$$c_1 \propto St^2, \quad (1.8)$$

where  $St$  is the particle Stokes number characterizing the particle's inertial with respect to the flow dynamics and is defined as the ratio of the particle inertial response time  $\tau_p$  to the Kolmogorov time scale  $\tau_k$  (see e.g. Tennekes and Lumley, 1972):

$$St \equiv \frac{\tau_p}{\tau_k} = \frac{1}{18} \left( \frac{\rho_p}{\rho} \right) \left( \frac{d}{r_k} \right)^2, \quad (1.9)$$

where  $\rho_p$  is the particle mass density,  $d$  is the particle diameter, and  $r_k$  the Kolmogorov length scale. The particle inertial response time,  $\tau_p$ , is obtained assuming Stokes flow ( $Re < 1$ ) around a spherical particle<sup>†</sup>. Other assumptions that go into the theory include: particle size much smaller than flow structures ( $d/r_k \ll 1$ ); effect of gravitational settling of particle is negligible which can be stated in terms small gravitational settling parameter,  $S_g \equiv v_g/v_k$ , where  $v_g = \tau_p g$  is the particle terminal falling speed; negligible flow modification by the particles which implies dilute particle loading (besides small particles).

According to Chun et al. (2005), the sub-Kolmogorov clustering arises because inertial particle at an average have a drift relative velocity that tends to bring particles

---

<sup>†</sup>Where the Stokes drag force is given as  $\mathbf{F}_d = 6\pi\mu a\mathbf{v}$ , with  $\mu$ , the fluid's dynamic viscosity;  $a$ , particle radius;  $\mathbf{v}$ , fluid velocity relative to the particle.

closer together. The steady form of the RDF results from the balance between this drift velocity and the dispersing effect of chaotic fluid motion.

Our own line of research is significantly influenced by this school of thoughts as can be seen from our methods of analysis of empirical data. However, we must point out that alternative theoretical approaches to this problem exist and should not be ignored (see e.g. Goto and Vassilicos, 2008; Duncan et al., 2005; Elperin et al., 2002; Bec et al., 2007). Of potential relevance to this thesis is the fractal interpretation of inertial clustering. Following Bec et al. (2007), inertial clustering is understood as resulting from the dynamic equations of motion (of the particle and fluid) being of the dissipative kind which leads to contraction of phase space of the system. Since the dissipation becomes strong in sub-Kolmogorov scales (where fluid strain is strong), particles will converge to a dynamically evolving attractor (a set of geometrical points). The cluster field will become fractal due to scale-invariant dynamics at these scales. A measure for clustering can be provided via the (fractal) correlation dimension  $\mathcal{D}_2$  (see Bec et al.). It is claimed (although never explicitly proven) that the correlation dimension and the clustering exponent are related via:

$$c_1 = 3 - \mathcal{D}_2. \quad (1.10)$$

In this sense our results casted in the language of  $c_1$  are also relevant to this line of work.



### 1.2.2 Other computational and experimental works

Recent and contemporary experimental studies of inertial particle clustering includes: Aliseda et al. (2002); Wood et al. (2005); Salazar et al. (2008). Each have shown evidence of inertial clustering in turbulence and found reasonable agreement with results from computation and theory. Here we strive to complement these studies with an independent and more comprehensive investigation of inertial clustering at high Reynolds numbers ( $R_\lambda > 400$ ).

Simulation works involving "direct numerical simulation" (DNS) method are also plentiful (besides those cited in previous section, see also e.g. Wang and Maxey, 1993; Falkovich and Pumir, 2004; Bec et al., 2007). Each of these publications have discerned interesting aspects of inertial clustering. Here we will also present a DNS study, in collaboration with colleagues from Cornell University (J. Salazar and L. Collins), which focuses on the effect of poly-dispersity (particle with a broad range of Stokes number) that has not been investigated in detail in previous studies.

## 1.3 Outline

We begin with a detailed description of the phase Doppler interferometry (PDI) technique and our PDI instrument in Chapter 2. This is followed by a description of how

this technique (in particular our PDI instrument) can be used to effectively study inertial particle clustering in Sec. 2.4.

In Chapter 3, we introduce the method of our choice for quantifying particle clustering: the radial distribution function (RDF). We motivate this choice by pointing out its origin in fundamental probabilistic reasoning and its usefulness in application. We also discuss how the RDF can be calculated in practice and how certain technical difficulties can be overcome. In Sec. 3.3, we discuss foundational issues regarding the interpretation of the RDF and consider the situation when more than one kind of inhomogeneity are present in the data (which is important to our experiment).

In Chapter 4, we describe our experimental setup and procedures in detail.

In Chapter 5, we present the first batch of our experimental results in form of a published paper. The main emphasis of the study is on the concept of Stokes number similarity.

In Chapter 6, we present the second batch of experimental results and also results from our poly-disperse DNS effort. Here we perform systematic (direct and indirect) comparison of results between theory, experiment and simulation. We also use the available data to aid understanding of inertial clustering by discussing the implications of our data for certain topics or questions regarding inertial clustering.

Chapter 7 summarizes and concludes this thesis.

## Chapter 2

# Phase Doppler Interferometry

Here we describe the fluid measurement technique central to all of the studies in this thesis. Phase Doppler interferometry (PDI) is a laser-optical method capable of measuring velocity and diameter of individual, spherical particles as they traverse the instrument's measurement volume. We will begin by describing its general working principle. This is followed by a description of the specifics of our own PDI instrument and an explanation of how this technique can be used for studying particle clustering in turbulence.

## 2.1 Background

The main capability of phase Doppler interferometry (PDI) is the measurement of velocity (up to three components) and diameter of spherical particles as they traverse its measurement volume. PDI is an extension of its simpler and older cousin, laser Doppler velocimetry (LDV) which measures only velocity (particle sphericity not required). LDV first appeared in the scientific literature in the 1960s while the phase Doppler extension was first conceived in 1975 and successfully realized physically in the early 1980s (Albrecht et al., 2002, Sec. 1.1). Since then, both techniques have matured and found popularity as research tools, with commercial PDI systems available as early as the late 1980s. For further historical details and current developments, see (Albrecht et al., 2002, Sec. 1.1).

Today, PDI and LDV are widely used in fluid dynamics experiments for making fixed-point measurement of fluid motion (flow seeded with tracer particles) and also to study dynamics of particles embedded in fluid or otherwise. Some of the often quoted novelties of the Doppler techniques include: non-intrusiveness, directional sensitivity, high spatial and temporal resolution and high accuracy.

## 2.2 Basic working principles

This section describes the general operation of PDI and only covers the complexity of the subject to a degree sufficient for the understanding of this thesis. More complete treatments can be found in (Albrecht et al., 2002, Chap. 2, 5).

Figure 2.1a shows the typical, basic setup of a PDI system. Two laser beams of nearly the same frequency are focused by a converging lens and cross each other at their respective beam waist (point of minimum beam cross section). This beam crossing region defines the measurement volume of the interferometer which has the approximate shape of an ellipsoid, a result from the gaussian profile of the laser beams typically used. Figure 2.1b depicts qualitatively the light intensity profile of the measurement volume in the  $x$ - $z$  plane. Such is the result of interference between the two beams. By considering two crossing plane waves (Albrecht et al., 2002, Sec. 2.1) one can see that the intensity profile can be reasonably represented by a gaussian enveloped, sinusoidal function of  $x$  position, similar to the Doppler burst shown in Figure 2.1a.

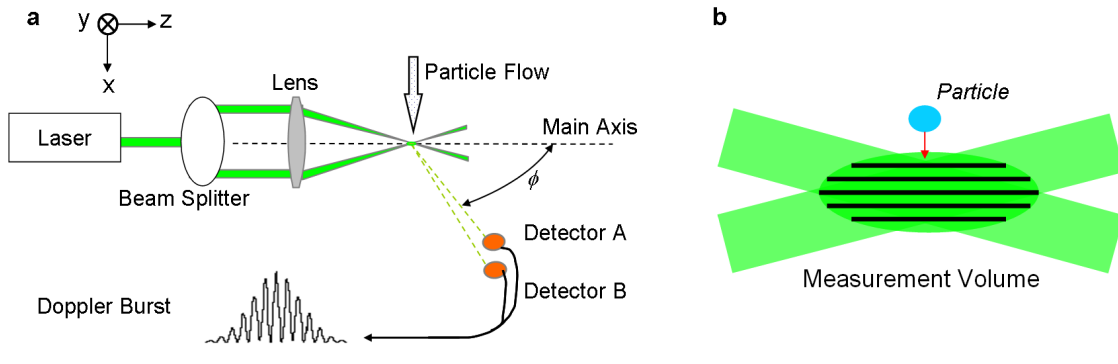


**Figure 2.1:** Schematic showing basic operating principle of phase Doppler Interferometry. The off-axis angle ( $\phi$ ) is measured in the ‘major plane’ (normal to the plane of the beams and containing the main axis).

### 2.2.1 Velocity measurement

Here we will proceed with a more intuitive interpretation of the velocity measurement of PDI; an alternative interpretation starting from Doppler effect can be found in (Albrecht et al., 2002, Chap. 2). Both methods are equivalent in the sense that they yield the same physical outcomes, while the former has the advantage of being more intuitive, the later is more explicit in showing the center role of Doppler effect in the theory of measurement.

Following the conceptual picture described in Sec. 2.2, when a particle traverses the measurement volume in the forward direction, it scatters light projecting the intensity profile of the measurement volume. One or more light detectors collect the scattered light and turn it into an electrical signal. A typical temporal evolution of the observed signal is depicted in Figure 2.1a and is commonly termed a ‘Doppler burst’. The frequency of each Doppler burst (Doppler frequency) is directly proportional to

the magnitude of the particle's velocity in the  $x$  direction:

$$|v_x| = f_d \delta, \quad (2.1)$$

where  $v_x$  is the  $x$  component of particle's velocity,  $f_d$  is the Doppler frequency and  $\delta$  is the fringe spacing of the intensity profile in the measurement volume satisfying the relation:

$$\delta = \frac{\lambda_b}{2 \sin \frac{\Theta}{2}}, \quad (2.2)$$

where  $\lambda_b$  is the laser beam wavelength and  $\Theta$  is the minor angle between the two crossing beams.

In practice, the direction ambiguity of  $v_x$  is broken by shifting the laser frequency of one of the beams relative to the other by  $\Delta f_b$  (e.g. by using acousto-optic modulator), resulting in:

$$v_x = (f_d - \Delta f_b) \delta \quad \text{for} \quad v_f \geq -|\Delta f_b \delta|. \quad (2.3)$$

When this is done the intensity fringes in the measurement volume will have uniform motion in one direction, in the present case the negative  $x$  direction, thus shifting the velocity corresponding to zero Doppler frequency to a negative value.



### 2.2.2 Size measurement

Here we continue with the same picture provided above, restricting ourselves to consider only particles that are spherical, optically homogenous-isotropic, non-opaque and of size sufficiently larger than the laser wavelength so that geometrical optics is a good approximation. Under these conditions, one can interpret the function of a detected particle as a optical lens (or mirror) that images the intensity fringes in the measurement volume to the surrounding space. This image of the fringes is then picked up by the detectors as depicted in Figure 2.2 showing an instantaneous snapshot of how the fringes are projected in space by the particle. The magnification of the fringes scales inversely as the particle size since that determines the curvature of the lens (or mirror). Multiple detectors placed at different locations effectively measures the spatial frequency of the magnified fringes by registering different phase of the fringes. The phase shift between the Doppler bursts measured by any detector pair is then monotonically related to the size of the particle. The exact relation between particle diameter and phase difference depends on the scattering mode considered (reflection, 1st order refraction, etc) and the physical setup of the instrument.

In practice, the detectors are place at scattering angles that favor only one scattering mode. When this is done and with a few additional assumptions (plane wave incident light, small particle compared to its distance from detectors), it can be shown that the diameter-phase relation for any detector pair is linear (Albrecht

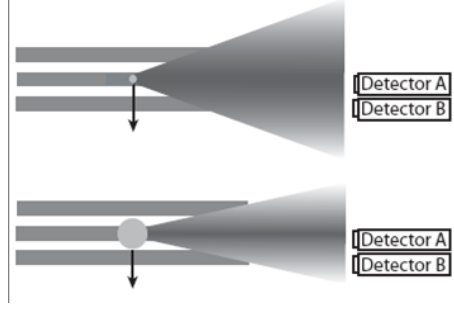


**Figure 2.2:** Particles as a lenses that project the measurement volume fringes onto the detectors. Figure from Chuang et al. (2008). For copyright information, see Appendix B.

et al., 2002, Chap. 5) :

$$d = F_{\Phi}(\lambda_b, \Theta, \phi, \psi_1, \psi_2) \Delta\Phi, \quad (2.4)$$

where  $\Delta\Phi$  is the phase difference;  $F_{\Phi}$  is the phase conversion factor, a function of laser wavelength and optical geometry of the system which includes beams-cross angle ( $\Theta$ ), off axis angle ( $\phi$ ) measured in the ‘major plane’ (see Fig. 2.1), and the elevation angles of the detectors ( $\psi_i$ ), measured relative to the major plane.

## 2.3 Our Phase Doppler Interferometer

Our PDI system is designed and manufactured by Artium Technologies Inc. The system consists of three sub units: the flight probe, the signal processor, and a personal computer with the data acquisition software.

The flight probe shown in Figure 2.3, contains a compact solid state laser

( $\lambda_b = 532 \text{ nm}$ , continuous wave), optical components, three photo-multiplier-tubes (PMT) as light detectors and supporting electronics. The detectors are all positioned at an off-axis angle ( $\phi$ ) of  $\sim 40$  degrees where first order refraction is the dominant scattering mode. The three detectors have small but different elevation angles so that three independent size measurement are made for each particle (one per each detector pair). This redundancy allows for extension of the range of measurable particle size, besides improving measurement accuracy and particle detection fidelity (Albrecht et al., 2002, Sec. 8.2).

After some pre-amplification, the output from the photo-detectors are fed to the signal processor, which digitizes the analog signals, performs Doppler burst detection\*, measures the raw burst's signal amplitude, performs signal filtering and further amplification. The output from the processor is passed via an interface card to a personal computer, where Fast Fourier Transform (FFT) is performed on each burst to obtain complex Fourier coefficients from which the frequency and phase can be extracted. The particle velocity and size is then calculated from the extracted frequency and phases as described in Section 2.2. Following that, the computer performs a burst validation routine to filter away false triggers based on a number of adjustable criteria, including phase difference consistency among the three signal channels, frequency consistency, signal to noise ratios in each channel, etc. In addition, the software in

---

\*For the interested reader, this is done (in principle) via continuous low resolution discrete Fourier transform and a potential burst is declared when there is a peak in the transform that exceeds a threshold

the computer is also capable of calculating various data statistics in near realtime. Finally, data is saved to disk including the raw sampled bursts, burst amplitudes, etc.

We will now discuss specific details of our PDI system that are relevant to this thesis.

### 2.3.1 The probe body's design

The probe body shown in Figure 2.3 is made of anodized aluminium with dimensions of the main section as 28 x 56 x 6.6 cm; each arm is 30 cm long and 4 cm in diameter, and the two arms are 15 cm apart (center to center). The probe body is designed so that it can make non-intrusive, in situ measurement of particle laden flow with finite mean velocity. When deployed with the arms pointing upstream, the measurement volume is well outside the body's boundary layers and far upstream of stagnation points. Specifically, this is achieved when the mean flow speed is above several centimeters per second and that the direction of the incoming flow is within 10 degrees of normal.

Modeling of the flow around the probe body was done using a commercial fluid dynamic package (Fluent). It was found that at a mean follow speed of  $2 \text{ ms}^{-1}$  normal to probe, there is a slight uniform increase of the flow speed around the measurement volume due to the contraction of flow by the arms. More relevant to

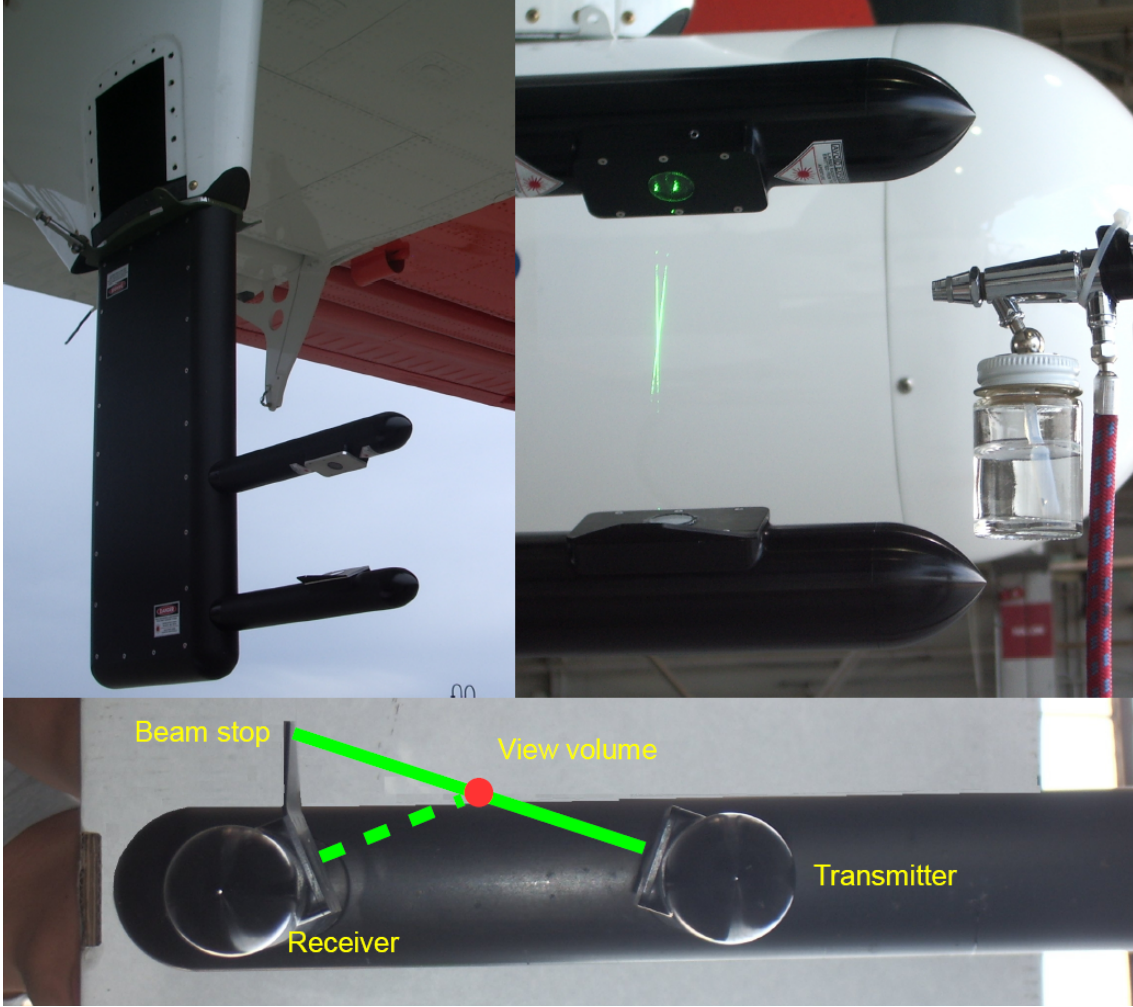


**Figure 2.3:** Two photos showing the Artium flight-PDI. Panel (a) shows the instrument mounted vertically onboard a research aircraft. Panel (b) shows the laser beams scatter off small water droplets. The beams emerge from the upper arm, The scattered light collected through the window of the lower arm and is sensed by three photo-detectors(internal). Panel (c) Front view of the two arms and the rough location of the view volume. The instrument body is 28 x 56 x 6.6 cm; each arm is 30 cm long and 4 cm in diameter; the arms are 15 cm apart. Figure from Chuang et al. (2008). For copyright information, see Appendix B.

this thesis is when particle trajectories are calculated (also using Fluent), there is at most a few percent deviation of particle velocity and relative position compared to the undisturbed upstream values. More details are available in Chuang et al. (2008).

### 2.3.2 Slit aperture and measurement volume

In order to have a better defined measurement volume and to allow for the flexibility of changeable measurement volume size, an adjustable slit aperture is added in the receiving optics to truncate the measurement volume in the  $z$  direction as shown in Figure 2.4. The slit width,  $l_s$ , is selectable between 50, 100, 200, 500 and 1000  $\mu m$ . The slit aperture is imaged onto the measurement volume where it has a magnified width of  $l'_s$  and thus the measurement volume width in the  $z$  direction,  $l_z$ , follows  $l'_s / \sin \phi$ .

However, other factors (i.e. diffraction and beam edges) may compromise the above result from geometrical optics. This is especially true for the case of narrowest and widest slit. From our measurement of intermediate cases (100 to 500  $\mu m$ ), we found that  $l_z$  is roughly 2 to 3 times the slit width ( $l_s$ ). The uncertainty of this result is rather large due to ambiguity of how the measurement volume edge should be defined and the fact that measurement volume is particle size dependent (details in Chuang et al. (2008)).

The other dimensions of the measurement volume, namely  $l_x$  and  $l_y$ , take the value of the beam width, which is found to be  $\sim 230 \mu m$ .

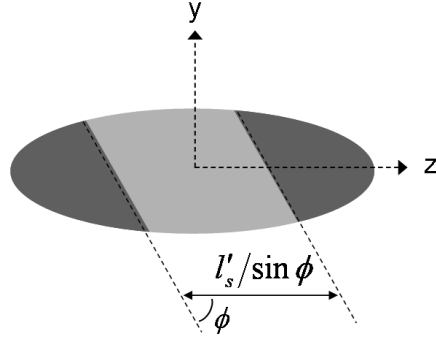


**Figure 2.4:** Truncated measurement volume resulting from the used of slit aperture (light gray area). Particle trajectories are into the page, detectors are located far away (not shown) downward and to the right.  $l'_s$  is the magnified slit width.

### 2.3.3 Arrival time accuracy

Especially important to this thesis is the accuracy of droplet arrival time or detection time which is typically not reported by manufacturers. We determined the corresponding accuracy by setting up the PDI system to measure a stream of monodisperse (single sized) droplets generated at uniform time interval with adjustable period. The droplets are generated via a drop-on-demand droplet generator by MicroFab Technologies. The arrival time accuracy of the PDI is calculated from the measured statistical distribution of the inter-particle arrival times (interval between subsequently detected particle). Since droplets are generated at nearly uniform intervals, the resulting distribution is a sharp, bell like curve. An upper bound of the single particle arrival time measurement is calculated from the standard deviation of this distribution. This provides an upper bound because some of the spread of the distribution is obviously due to error in the droplet generation timing and other environmental effects on the

	Advertised	Our Findings
Drop arrival time accuracy	n/a	$< 3.5\mu s$
Drop Size measurement range	0.5 to $> 1000\ \mu m$	n/a
Estimated accuracy	$\pm 0.5\ \mu m$	7 to 20% (see text)
Estimated resolution	$\pm 0.5\ \mu m$	n/a
Velocity measurement range	-100 to 300 m/s	n/a
Velocity accuracy	to $\pm 1\%$	$\pm$ a few percents
Volume Flux accuracy	to $\pm 15\%$	n/a

**Table 2.1:** Table showing the measurement accuracy and dynamic range of our PDI system as claimed by the manufacturer and the results of our own characterization (not always consistent with manufacturer’s). Velocity measurement range is variable, velocity accuracy is reported in percent of measurement range.

droplet trajectory from nozzle to measurement volume. The upper-bound was found to be  $3.5\ \mu s$ .

### 2.3.4 Velocity accuracy and range

Table 2.1 shows the various measurement accuracies and dynamic ranges of our system copied directly from the brochure published by the manufacturer. Since these numbers are likely to be general and represent best case scenario, we carried out independent measurements in our lab to determine the various accuracies of our system.

Velocity measurement precision of the PDI system is independently calibrated in our lab by measuring the velocity of optical fiber core attached to a spin-wheel of a mechanical laser-chopper with precisely controlled spinning frequency (Thorlabs, model MC1000). The test was set up with both the probe and the spin-wheel fixed



in space so that a fixed point on the fiber core (acting as particle) cuts through the measurement volume in every spinning-cycle. The standard deviation of the velocities measured gives the measurement precision which varies from less than 1% to a few percent, corroborating the manufacturer’s claim of 1% accuracy. The mean velocity measured is also in agreement (within measurement error) with those calculated from spin-frequency multiplied by radius of circular motion. Besides this, we have many ‘in field’ observations that provide inter-comparison between the measurements of our PDI system with other independently calibrated instruments including Hot-wire Anemometry (HWA) and another PDI system. The results show agreement in mean flow velocity to within 10% or less, suggesting insignificant systematic bias in the measurement at least at the level required by our experiments (Sec. 4.3.1 and Sec. 4.4). Further details on velocity accuracy including some theoretical discussion and inter-instrumental comparison can be found in Chuang et al. (2008).

### 2.3.5 Sizing accuracy and range

We calibrate the size (diameter) measurement using droplets from the monodisperse droplet generator (with diameter  $\simeq 55\mu m$ ) and two sets of precision solid glass microspheres (Duke Scientific, series 9000) with mean diameters  $10.0 \pm 1.0\mu m$ ,  $30.1 \pm 2.1\mu m$  and standard deviation of their distribution of  $1.4\mu m$ , and  $2.0\mu m$ , correspondingly. Results for the droplets showed that PDI measurement has precision of

$\sim 0.1 \mu m$ , based on standard deviation of the measured diameters. This is consistent with the manufacturer's claim (cf. Table 2.1). We could not use the droplets to study the bias since we do not know the droplet size *a priori*. Results for the glass microspheres, after correcting for their own internal standard deviations, yield precision of the PDI system of 2 to  $3 \mu m$  and no discernible bias at this precision (difference in mean is less than the uncertainty). The reason the microspheres studies yield a poorer instrumental precision is very likely explained by the important phenomenon discussed in the following paragraphs.

It was found that the size measurement is affected by the edge of the measurement volume imposed by the slit aperture (cf. Fig. 2.4). Since the droplet stream emerging from our droplet generator sustains a straight line motion for a finite distance, we were able to make the droplet traverse through the measurement volume with highly localized  $y$ - $z$  position (see Fig. 2.4). Care has been taken to ensure that drop shape oscillation is negligible by gradually moving the drop emitting nozzle away from the measurement volume along the  $x$  direction. When we move the droplet stream about the  $y$ - $z$  plane, we observed that droplet diameters reported by the PDI vary significantly when droplets are near the edges of the measurement volume.

For instance, referring to Figure 2.4, if we initially position the droplet stream at a position centered in  $y$  but with a  $z$  position close to the positive edge of the effective measurement volume (right edge of the light gray area) and then start to

move the stream in the  $+y$  direction, the diameter reported would at first remain constant and then the value will increase slightly (by  $\sim 4\%$ , with  $55\ \mu m$  drops) followed by a steep decrease ( $\sim 20\%$ , with  $55\ \mu m$  drops). In the decrement zone, the Doppler bursts' amplitudes are relatively small and only a fraction of the droplets are validated, signifying some edge is reached. The same is not observed if we move the stream in the opposite ( $-y$ ) direction. It was also found that the point where the reported diameter starts to vary is shifted outward (towards  $+y$ ) if a wider slit aperture is chosen.

A general mechanism of this 'slit effect' based on geometrical optics can be found in Albrecht et al. (2002, Sec. 8.3). The main idea is that an unwanted scattering mode (reflection) becomes dominant at the  $+z$  end of the slit due to blockage of the preferred first order refraction mode. However we found that this does not provide a complete description of our observations. For instance, we also found similar diameter drop-off at the  $-z$  end of the slit where the first order refraction is not blocked.

The slit effect provides an explanation for the relatively poor PDI sizing precision reported for glass microspheres as compared to the droplet stream. The explanation being that because the microspheres were simply sprinkled onto the measurement volume, they sampled the whole measurement volume including the edges where inaccurate sizes would be reported.

In real experiments, it is reasonable to assume that the measurement volume

would be uniformly traversed by the particles, thus the true diameter precision is therefore significantly worse than claimed and will be dependent on the width of the slit aperture. Furthermore there would also be a weak bias towards smaller diameters. From the various calibrations we have done for the case of slit aperture width of  $200\ \mu m$  (most relevant to this thesis), we found that the precision (standard deviation) goes from  $2\ \mu m$  at mean diameter of  $10\ \mu m$  to  $3\ \mu m$  at  $30\ \mu m$  and  $4\ \mu m$  at  $55\ \mu m$ . The only statistically significant bias was observed for the  $55\ \mu m$  case with the rough value of negative  $1.5\ \mu m$ .

To summarize, the sizing precision of the PDI system when droplets are constraint to traverse only the interior cross-section of the measurement volume is of the order of  $0.1\ \mu m$  with negligible bias, as claimed by the manufacturer. However some form of non-fully understood slit effect deteriorates the precision and accuracy in real experiments. With the most typical choice of  $200\ \mu m$  slit aperture, the effective precision was found to goes from 20% at  $10\ \mu m$  to 7% at  $55\ \mu m$ .

## 2.4 Observing particle clustering with PDI

The PDI method, particularly our PDI system, is suitable for studies of particle clustering when the probe is oriented such that there is a strong mean flow in the  $x$  direction. Examples of this suitable situation include when the probe is placed

inside a wind tunnel, turbulent or otherwise and when the probe is flown through atmospheric clouds. To be more precise, we are interested in situations where the mean flow velocity is much stronger than the average deviation of particle velocities from the mean flow. Such deviation may be caused by the presence of turbulence or other forces like gravity.

Under this condition, one can calculate inter-particle distances in the  $x$  axis from the arrival times of each particle as shall be discussed in section 4.3.1. This essentially contains information on the one dimensional distribution of the particles in space, from which further analysis can be made.

The ability to measure the size of individual particles allows the experimentalist to condition the analysis on particle size and to study how particle size influence the particle (spatial) distribution or clustering. In addition, one can also study the cross-correlation between particles of different sizes.

Finally the velocity measurement allows one to characterize turbulent statistics of the ambient flow. With this information, one can study how turbulence affects the particle distribution and vice-versa. However, in practice certain turbulent statistics can only be measured reliably with either very high particle detection rate or a long enough sampling time (which may not be readily attainable in some experiments). A challenging turbulence statistics for the PDI is the energy spectrum of the turbulence<sup>†</sup>,

---

<sup>†</sup>Still an area of active research.

and examples of the turbulent spectrum obtained with our PDI system in wind tunnel will be discussed in chapter 4 (cf. Fig. 4.4 and corresponding text).



## Chapter 3

# Radial distribution function (RDF) in application

In this chapter, we will introduce the main mathematical tool used for quantifying particle clustering in our experimental analysis. We present the derivation of the RDF from fundamental probability theory followed by a detailed description of its calculation from particle position data. This is followed by a discussion of certain theoretical aspects of the RDF related to its application in the analysis of experimental data.



### 3.1 Definition from basic probability

The radial distribution function (RDF) is essentially a measure of correlation of particle position in space as compared to uniform-random distribution of particles (the Poisson point process). Here we present its definition following the works of others (Shaw et al. 2002; Larsen 2006; McQuarie 2000, Sec. 13-2).

We begin by considering a field of particles in space. We restrict ourselves to the case of statistical homogeneity in space and statistically identical particles in the sense that any single particle has equal probability to be anywhere in space. Under this scheme, any inhomogeneities in the particle density field are interpreted as correlations between particle positions. A discussion of why inertial particle advected by homogenous-isotropic turbulence satisfy these conditions (at the long time limit) is attempted in Section 3.1.1. Generalization that allows for statistical inhomogeneity (at scales larger than the scales of the correlation of interest) is discussed in Section 3.3.2.

We first define two infinitesimal volumes —  $\delta V_1$  and  $\delta V_2$  — in the space containing the particles and let  $\vec{r}$  be the displacement of  $\delta V_2$  relative to  $\delta V_1$ . With these, we define the RDF, written as  $g(\vec{r})$ , based on basic probability:

$$g(\vec{r}) = \frac{P(1, 2)}{P(1) P(2)}, \quad (3.1)$$

or alternatively:

$$g(\vec{r}) = \frac{P(2|1)}{P(2)}, \quad (3.2)$$

where  $P(1)$  is the probability that  $\delta V_1$  is occupied by a single particle and  $P(2)$  is similarly defined with respect to  $\delta V_2$ ,  $P(1,2)$  is the joint probability that both infinitesimal volumes are occupied and  $P(2|1)$  is the conditional probability that  $\delta V_2$  is occupied given that  $\delta V_1$  is. Some important observations:

- Since the definition is based on infinitesimal volume elements, the probability of occupancy of two or more particles is negligible.
- The RDF can thus be interpreted as a measure of enhanced probability of finding other particles as function of relative displacement from a particle.
- If the system of particles satisfies isotropy (as are most cases in this thesis), then one can write the RDF as  $g(r)$ .

Apart from being a suitable quantification of particle clustering in turbulence, the RDF has the advantage of being directly useful in theories of particle fields where clustering plays a role. For instance, it was shown that  $g(r)$  is directly involved in the equation for particle collision rate in turbulence by Sundaram and Collins (1997) (the same work shows enhancement of collision rate due to clustering) and also in radiation extinction inside a field of clustered particles (Kostinski and Shaw, 2001).

Alternatively, a more practical definition of RDF starting with a finite  $\delta V_2$  is possible\*. However, in practice, this has not been done as it is more convenient to calculate what would amount to a volume-weighted average of  $g(r)$  as will be discussed in Section 3.2.

### 3.1.1 Relevance to particle clustering in turbulence

In this section, we discuss the relevance of the concept of the RDF as derived in Section 3.1 to particle clustering in homogenous and isotropic turbulence which is at the core of the experimental efforts in this thesis. Specifically we wish to motivate that particles advected by turbulent flow satisfy the conditions used in deriving the radial distribution function, namely spatial statistical homogeneity and identically distributed particles.

Considering a set of particles placed into a turbulent flow field at some time. Indifferent to their initial positions, after sufficiently long time compared to turbulent time scales, each and every particle would have equal probability to be at any point satisfying the two conditions due to the homogenous and isotropic nature of the driving turbulence. Implicit to this statement is the fact that we have ignored the determinism of classical fluid mechanics while appealing to the apparently chaotic nature of turbulent flow that deems impossible the ability of the experimenter to

---

\*Such a definition however would not be directly applicable in theories discussed above.

specify the initial or boundary conditions sufficiently well for any deterministic prediction. Although perhaps philosophically debatable, this is especially relevant for real experiments such as those reported in this thesis where particles are repeatedly injected into a statistically stationary turbulent flow in a wind tunnel<sup>†</sup>.

## 3.2 Calculating the RDF from a particle field

Here we consider the problem of estimating  $g(\vec{r})$  given a sample (or realization) of a particle field with sample size  $V$  much larger than any clustering scales. This shall allow us, later on, to estimate the true average particle density as the sample's average particle density.

For convenience we first reproduce the definition of the RDF (Eq. 3.2) here:

$$g(\vec{r}) = \frac{P(2|1)}{P(2)}. \quad (3.3)$$

Since the definition is based on infinitesimal volumes, we shall proceed correspondingly before considering finite volumes. Our first task is to estimate  $P(2|1)$ . The close relation between  $g(\vec{r})$  and  $P(2|1)$  turns out to be a fruitful one here. Since  $P(2|1)$  is a statistic conditioned on the presence of a single particle, this allows one to break down the calculation to the single particle level and thus enjoy much flexibility

---

<sup>†</sup>In this case, statistical homogeneity is only guaranteed sufficiently far away from physical boundaries.

in composing the estimation procedure. This flexibility, for instance, allows one to correct for error due to sample boundaries (Sec. 3.2.2) and to handle the problem of small sample size (Sec. 3.2.3).

We estimate  $P(2|1)$  (the conditional probability of finding an occupied  $\delta V_2$  at  $\vec{r}$  from any given particle) by the standard ‘*successes/trials*’ method. Each particle that is present is a valid trial and we define a success as finding a particle in the infinitesimal volume  $\delta V_2$  at  $\vec{r}$  from the trial particle under consideration (strictly, it is the  $\delta V_2$ ’s that serve as trials). We thus have:

$$P(2|1) = S(\vec{r})/N_t, \quad (3.4)$$

where  $S(\vec{r})$  is the number of successes (number of trial particles that see a neighbor particle in  $\delta V_2$  at position  $\vec{r}$  relative to itself) and  $N_t$  is the number of trials. It is important to note that  $N_t$  need not be the total number of available particles as long as the selection of trials is fair — neither favoring particles within a cluster nor otherwise. This reflects the fact that the calculation may be broken down to the level of single trial particles as mentioned earlier. Section 3.2.2 shows how this flexibility can be utilized to avoid estimation bias due to sample edges.

On another note,  $P(2)$  may be estimated from Poisson statistics taking the

infinitesimal volume limit (Larsen, 2006, Sec. 2.4):

$$P(2) = \lim_{\delta V_2 \rightarrow 0} 1 - \exp(-n \delta V_2) = \frac{(N-1) \delta V_2}{V}, \quad (3.5)$$

where on the far right, we have substituted  $n$  — the expected particle number density assuming zero correlation of particle positions — with the sample’s average number density<sup>‡</sup>:  $(N-1)/V$ . With these, we have an operational definition of the RDF as:

$$g(\vec{r}) = \frac{S(\vec{r})/N_t}{(N-1) \delta V_2/V}, \quad (3.6)$$

where again  $S(\vec{r})$  is the number of trial particles having a neighbor particle in  $\delta V_2$  at  $\vec{r}$  from itself,  $N_t$  is the total number of trial particle considered, and so on.

We now present two important corollaries:

1. If isotropy is satisfied by the system under consideration, then we can average Eq. 3.6 over spherical shells for each  $r$ , thus giving us the commonly seen, isotropic radial distribution function:

$$g(r) = \frac{\psi(r)/N_t}{(N-1) \delta V_r/V}, \quad (3.7)$$

---

<sup>‡</sup>This follows from the fact that  $V$  is much larger than any correlation scales. The ‘ $-1$ ’ term is added in observation that the trial particle must be excluded from the pool of possible occupants of  $\delta V_2$  consistent with the scenario of  $P(2|1)$ .

where now,  $\psi(r)$  is the sum over ‘numbers of particles found at distance  $r$  from each trial particle’ and  $\delta V_r$  is the volume of the infinitesimal shell (e.g.  $4\pi r^2 \delta r$  in 3D).

2. Furthermore, if the sample edge effect is negligible, — for example when the sample has periodic boundaries or when  $N$  and  $V$  is large enough that errors due to edges are small — then one may, without loss of accuracy, use all particles as trial particles ( $N_t \rightarrow N$ ). As a result,  $\psi(r)$  will become equal to  $2N_p(r)$  with  $N_p(r)$  defined as the total number of particle pairs in the sample separated by distance  $r$  (the factor of 2 arising as a result of double counting). Hence we have:

$$g(r) = \frac{2N_p(r)/N}{(N-1)\delta V_r/V} . \quad (3.8)$$

This result has many interesting interpretations which we shall only discuss after we consider the case of finite  $\delta V_r$ .

### 3.2.1 Extension to finite interrogation volume

Here we consider the more practical case of finite interrogation volumes ( $\delta V_2$  or  $\delta V_r$ ) which is unavoidable in any realistic analysis of experimental data. We will focus only on the case of isotropic RDF since it is the most commonly encountered and also the case of relevance to the analysis in this thesis. For simplicity, we also restrict ourselves

to the case of negligible sample edge effects (cf. Eq. 3.8). Generalization to account for sample edge effect should be fairly straight forward since it is an independent effect from our subject matter here. However, the same cannot be said of the isotropy condition. We shall see that, due to isotropy, we need to discriminate between data of different dimensionality<sup>§</sup> since the consequence of finite interrogation volume on them are different.

Strictly, Eq. 3.8 is a valid estimator of the RDF only in the limit of vanishing  $\delta V_r$ . However, in the analysis of real experimental data, one needs to do some averaging over  $\delta V_r$ . The common practice, including that of this thesis, is to simply extrapolate Eq. 3.8 for the finite case. For clarity, here we rewrite Eq. 3.8 substituting  $\delta V_r$  with its finite counterpart  $\Delta V_r$ :

$$g_{\Delta r}(r) = \frac{2N_p(r)/N}{(N-1)\Delta V_r/V}, \quad (3.9)$$

where everything has the same meaning except that  $\Delta V_r$  is now a finite volume (e.g.  $4/3\pi(r_2^3 - r_1^3)$  in 3D) and correspondingly  $N_p(r)$  is now the number of pairs separated by  $r \pm \Delta r/2$ . Some observations:

- It can be seen that Eq. 3.9 no longer reflects the fundamental probabilities (as in Eq. 3.3) by considering, for instance, a simplest yet non trivial case where there are only three particles in  $V$  with two of them being within  $r' \pm \Delta r/2$

---

<sup>§</sup>i.e. data collected in 1, 2, or 3 spatial dimensions.



from the first. Here, the numerator of Eq. 3.9 for the case ( $r = r'$ ) yields  $4/3$  which is greater than 1, thus can no longer be a valid estimate of  $P(2|1)$ .

- Mathematically, one can show that  $g_{\Delta r}(r)$  is related to the infinitesimal one (Eq. 3.8) via:

$$g_{\Delta r}(r) = \frac{1}{\Delta V_r(r)} \int_{\Delta r} g(r') \frac{dV_r(r')}{dr'} dr' . \quad (3.10)$$

In words, the finite volume RDF,  $g_{\Delta r}(r)$ , is the interrogation-volume-weighted average of the infinitesimal one.

- One interesting aspect of  $g_{\Delta r}(r)$  as written in Eq. 3.9 is that it affords multiple interpretations apart from being a volume-weighted average of the (fundamental) RDF. If we write:

$$g_{\Delta r}(r) = \frac{2N_p(r)/(N \Delta V_r)}{(N-1)/V} , \quad (3.11)$$

then we see that it is the ratio of average density at distance  $r$  from each particle *to* the expected density if a uniform-random distribution is assumed.

Alternatively we may write:

$$g_{\Delta r}(r) = \frac{N_p(r)/\Delta V_r}{N(N-1)/2V} , \quad (3.12)$$

and then we have a ratio of pair density *to* the expected pair density under a uniform random distribution (Holtzer and Collins, 2002).

The consequence of the volume-weighted averaging effect when using Eq. 3.9 for analysis of data is as follows: For 3D or 2D particle position data, the estimated RDF would be biased towards larger  $r$  within each  $\Delta r$  bin (as compared to the infinitesimal RDF). This is because isotropic shells of larger  $r$  have larger volumes (with constant  $\Delta r$ ). On the other hand, for 1D particle position data collected through a thin line, the volume-weighted averaging reduces to simple averaging without any bias.

Thus if one wishes to have an unbiased estimate of the infinitesimal RDF related to fundamental probability as discussed in Section 3.1, it is desirable to use very fine bins ( $\Delta r$ ) when processing 3D or 2D data via Eq. 3.9. This can then be followed by a simple averaging manually to suppress statistical noise. For 1D data however, Eq. 3.9 may be used with finite  $\Delta r$ , as will be done in this thesis.

### 3.2.2 Sample edge treatment

When the data available has a sample size ( $N$  and/or  $V$ ) that is small enough such that edge effects become important, Eq. 3.8 and Eq. 3.9 are no longer an accurate estimate of the RDF. This is because particles that are close to the sample edges (closer than the scale at which  $g(r)$  is evaluated) have truncated interrogation volumes and thus should not be normalized by the full isotropic shell volumes  $\Delta V_r$ .

To treat this, one could utilize the fact that the RDF estimation can be broken

into those based on single trial particles (as discussed below Eq. 3.3). The simplest way to do this is to exclude these ‘edge particles’ from the pool of trial particles by rolling back to the more general Eq. 3.7 while allowing  $\delta V_r$  the flexibility to also represent a finite shell.

The full treatment of the edges, albeit more computationally intensive, can be done by appending to the above procedure, individual treatments of the edge particles via Eq. 3.7 with  $\delta V_r$  substituted by the truncated interrogation volumes of each of them, then followed by a  $(N_t \Delta V)$ -weighted averaging of all the results. Note that Weighting by  $N_t$  simply reflects the modularity of the calculation at the single trial particle level while weighting by  $\Delta V$  stems from the isotropic averaging done in going from Eq. 3.6 to Eq. 3.7. Full treatment of the edges is used in the analysis of experimental data in thesis and will be discussed in Sec. 4.3.2.

### 3.2.3 Averaging the RDF over many small samples

When sample size  $V$  is comparable to the clustering scales, estimation of  $g(r)$  from a single sample using Eq. 3.7 is essentially biased because the value of its denominator fluctuates with the location of the sample (due to the clustering itself) and does not reflect the global average. However, if we have a big set of small samples taken in different locations and/or times, then it is possible to form a unbiased estimator of

$g(r)$  by averaging over many such samples (ensemble average).

Let us consider samples taken in a fixed location at different times. If we can assume statistical stationarity and that the sampling is done without prejudice (not favoring either clusters or voids), then each sample is an independent realization of the same physical system. We can then average over many such samples to obtain an estimate of the RDF. Referring back to Eq. 3.3, all we need are estimates of  $P(2)$  and  $P(2|1)$  that average over multiple samples. Following Eq. 3.4, we may construct:

$$P(2|1) = \frac{\sum S(\vec{r})}{\sum N_t}, \quad (3.13)$$

where the summation is over the samples. Note that here we have utilized again the particle-by-particle flexibility of the estimation scheme. Independently, from Eq. 3.5, we saw that  $P(2)$  is directly related to the (uniform-random equivalent) particle number density  $n$ . To that end, although the local number density in each sample inadvertently fluctuates away from  $n$  (due either to particle correlation or fundamental Poisson fluctuation), the average of number density over many such samples would approach  $n$  given that the sampling process is without prejudice. Thus we may write:

$$P(2) = \frac{(\sum N - 1) \delta V_2}{\sum V}. \quad (3.14)$$

With these, the estimator under the condition of isotropy, finite interrogation

volumes and with edge particles excluded is given by:

$$g(r) = \frac{\sum \psi(r) / \sum N_t}{(\sum N - 1) \Delta V_r / \sum V}, \quad (3.15)$$

which can be seen as a generalization of Eq. 3.7. It is also worth noting that, the volume-weighted averaging effects of  $\Delta V_r$  (Sec. 3.2.1) are still in effect independent of the averaging over samples since both processes are linear and independent.

## 3.3 Characteristics of the RDF

### 3.3.1 Relation of RDF to scales of clustering

Here we give a few words on the relation of the RDF to the scales of clustering. Earlier works (Shaw et al., 2002; Kostinski and Shaw, 2001) have shown that the RDF<sup>¶</sup> does not have ‘memory’ of the smaller scales — the values of  $g(r)$  at a given  $r$  is not influenced by any clustering at scales smaller than  $r$ . In relation to that, here we wish to show that the converse —  $g(r)$  has no ‘memory’ of larger scales — may not be true depending on what one means by ‘scales of clustering’.

In general  $g(r)$  has the following behavior: when the particle field has no clustering at all (uniform-randomly distributed), then its value would be unity at all

---

<sup>¶</sup>In these papers, it was the pair correlation function (equivalent to  $g(r) - 1$ ) that was discussed.



**Figure 3.1:** Caricature of a one dimensional particle field made up of randomly distributed blocks of particles (without overlap). All blocks has the same size (say  $b$ ) and within each block, particles are uniform-randomly distributed.

scales ( $r$ ). When there is clustering,  $g(r)$  would be greater than unity below some scales related to the scales of clustering (signifying the enhanced probability of finding neighboring particles), while becoming slightly lower than unity for larger scales.

We now consider a particle field, in 1D space for simplicity, which is made up of randomly distributed blocks of particles (without overlap), where inside each block the particles are uniform-randomly distributed (illustrated in Figure 3.1). Let the blocks all have equal size,  $b$ . For some, this particle field would be described as having a single clustering scale – the size of the block clusters,  $b$ . However if one calculates  $g(r)$  for this particle field, the result would be a curve that increases quasi-linearly for  $r \lesssim b$ . This can be seen clearly considering when  $r$  becomes smaller, the success rate of finding neighboring particles is higher while everything else remain unchanged (cf. Eq. 3.6). Similar argument may be extended for three dimensional data and were also found to be consistent with simulated results.

Thus one needs to be careful with what one means by the terms ‘size of the clusters’ and ‘clustering scales’ when relating to the magnitude trends of  $g(r)$ . For

the block clusters considered here, if we insist that the magnitude of  $g(r)$  represent the extent of clustering, then we must interpret these block clusters as having clustering that increases with decreasing scale despite the notion that inside each block the particles are uniform-randomly distributed.

Regardless of how we wish to interpret the meaning of ‘clustering scales’, the application of  $g(r)$  in other theories as earlier discussed in Section 3.1 is fundamentally sound since they stem from its mathematical definition.

### 3.3.2 Inertial clustering and turbulent mixing

The radial distribution function, traditionally defined (Sec. 3.1 and reference therein), does not discriminate between the mechanisms of correlation between particle positions. In turbulence, particles may have correlations in their number density caused by other effects apart from the mechanism of inertial clustering. All of these inhomogeneities will appear in the RDF calculated via the family of equations that follows from Eq. 3.7.

Particularly important to this thesis, apart from inertial clustering itself, is the inhomogeneity due to particle injection into an otherwise homogenous and isotropic turbulent flow. Due to the random stirring and mixing effect of turbulence, these density inhomogeneities would be slowly smoothed. However their residues would

blend into the observed RDF (via Eq. 3.7 or the likes) in addition to the signature of inertial clustering of interest. Here we shall show that, due to the distinct scales of the two processes (the residual turbulent mixing being at large scales), the effect of the mixing residues on the inertial clustering signature is simply a multiplicative factor on the  $g(r)$  of the otherwise pure signature of inertial clustering and that this factor is nearly a constant (over the clustering scales) when the two scales are well separated. (This finding will be utilized in our data analysis to isolate the influence of mixing over the signatures of inertial clustering.)

Although the main intention here is to address the relation between mixing and inertial clustering, the mathematical result here may be extended to other system satisfying similar conditions. We begin with some definitions and assumptions:

- We assume that the inhomogeneity of the particle density field is driven by two classes of processes with distinct scales and that they are mutually uncorrelated. Particularly for our case of interest, the inhomogeneous initiation of the particle field into turbulence should have no effect on how particles are clustered due to small scale vortices<sup>||</sup>. Thus the role of the large scale inhomogeneity is just to introduce a landscape of varying local densities within which the particles are clustered by the local vortices.
- We define  $m(\vec{r})$  as the local number density dictated only by the large scale

---

<sup>||</sup>This is true as long as the injection process itself has little effect on the turbulence field



inhomogeneity. Precisely, this may be defined as the (idealized) density profile when the system hosts only a large number of particles that are unaffected by the small scale clustering (in our case, a field of passive scalars) while satisfying all initial conditions of the problem (such as the particle injection geometries). Experimentally,  $m(\vec{r})$  can be approached by averaging the observed particle density over a scale much larger than the small scale clustering yet much smaller than the large scale inhomogeneity.

- We define  $g_m(r)$  as the RDF that corresponds to the large scale inhomogeneity and that can be computed from  $m(\vec{r})$ . When there is no such large scale inhomogeneity, in other words when ‘large scale averaged’ particle density is constant everywhere,  $g_m(r)$  would be equal to unity at all  $r$ .
- We define  $g_n(r)$  as the ‘normal’ RDF calculated from a sample using the traditional method derivable from Eq. 3.7, that is when a global particle density is used and any inhomogeneities are interpreted as particle spatial correlations.
- We use  $g(r)$  to represents the ‘pure’ RDF signature of the small scale clustering that is of interest. It will be recovered by  $g_n(r)$  when large scale particle density,  $m(\vec{r})$ , is indeed constant everywhere. Otherwise,  $g_n(r)$  would be some composite of  $g(r)$  and  $g_m(r)$ .
- We shall be interested in the theoretical or mathematical relation between  $g_n(r)$ ,  $g_m(r)$  and  $g(r)$ . To that end, the ‘limits of large numbers’ will be assumed

throughout the development to follow. This means we will be considering the idealized situation where we have infinitely many particles (so that density is well defined) inside an infinitely large sample (so that all RDF estimators approaches the true values), and other idealizations.

With these we proceed to consider the case of particle distributed in one dimension for sake of simplicity, conceptual clarity, direct relevance to this thesis and also for the fact that the finite volume version of RDF in 1D is unbiased (Sec. 3.2.1). (Generalization to higher dimension seems straight forward but will not be attempted here.) We first write down the formula for  $g_n(r)$ , the normally calculated RDF (cf. Eq. 3.7) for the one dimensional case:

$$g_n(r) = \frac{\sum_{i=1}^{N_t} S_i(r)}{N_t n \delta r}, \quad (3.16)$$

where  $S_i(r)$  is the number of particles found at position  $r \pm \delta r$  from the  $i$ th trial particle and  $n$  is the sample's global average particle density (in 1D). Next, we introduce in the summation the local (large scale) particle density at position  $r$  relative to each trial particle,  $m_i(r)$ :

$$g_n(r) = \frac{\sum_i^{N_t} \frac{S_i(r)}{m_i(r)} m_i(r)}{N_t n \delta r}. \quad (3.17)$$

We now take the key step of grouping the summation according to various values of  $m_i(r)$ , which we denote as  $m_j$  (where  $j = 1, 2, 3 \dots$ ):

$$g_n(r) = \frac{\sum_j \sum_i^{N_j} \frac{S_{ij}(r)}{m_j} m_j}{N_t n \delta r}. \quad (3.18)$$

Here  $N_j$  is the number of trial particles belonging to the  $j$ th group — those that see, at position  $r$  relative to each, other particles with number density of value  $m_j$ . Note that  $N_t = \sum_j N_j$ . Bringing everything that are independent of  $i$  out of the summation over  $i$ , introducing  $N_j$  and bringing  $\delta r$  inside the summation over  $j$  :

$$g_n(r) = \frac{\sum_j \left\{ N_j m_j \frac{\sum_i^{N_j} S_{ij}(r)}{\delta r N_j m_j} \right\}}{N_t n} . \quad (3.19)$$

Here we recognize that the quotient inside the parenthesis is an unbiased estimator of  $g(r)$  (the small scale clustering signature) for every  $m_j$ . The reason for this is because the trial particles under the summation over  $i$  all see the same density  $m_j$  at  $r$  relative to them. Hence the quotient is a construct much like an RDF estimator averaged over many small yet statistically identical samples (Sec. 3.2.3). We thus write it as  $g_j^{Est}(r)$  in what follows. Next, multiplying and dividing the whole right hand side with  $\sum N_j m_j$  ; and rearranging, we have:

$$g_n(r) = \frac{\sum_j N_j m_j}{N_t n} \left( \frac{\sum_j N_j m_j g_j^{Est}(r)}{\sum_j N_j m_j} \right) . \quad (3.20)$$

We quickly see that the inside of the parenthesis is a weighted average of  $g_j^{Est}(r)$  and since we are taking the ‘limits of large numbers’, it will approach the true RDF signature of small scale clustering,  $g(r)$ . Before we continue, it is worth noting as a corollary that this provides us with a means of recovering directly the small scale

clustering signature even when large scale inhomogeneity is present, that is:

$$g(r) = \frac{\sum_j N_j m_j \frac{\sum_i^{N_j} S_{ij}(r)}{\delta r N_j m_j}}{\sum_j N_j m_j} = \frac{\sum_i^{N_t} S_i(r)}{\delta r \sum_j N_j m_j}. \quad (3.21)$$

Turning back to Eq. 3.20, at the ‘limits of large numbers’, the quotient outside the parenthesis would become  $g_m(r)$ . This can be seen clearer if we consider:

$$\frac{\sum_j N_j m_j}{N_t n} = \frac{\sum_j N_j (m_j \delta r)}{N_t n \delta r}, \quad (3.22)$$

where the numerator reads: sum over the ‘expected number of other particles found at  $r$  from each trial particle’ as dictated by the density field  $m(\vec{r})$ . Hence we have established the general relation:

$$g_n(r) = g_m(r) g(r). \quad (3.23)$$

In words: the RDF calculated using global average density (Eq. 3.16) is the product of the RDF that would result from large scale inhomogeneity (e.g. mixing residue) and that of the small scale.

Finally, if the scales of the two families of inhomogeneities is sufficiently separated, then  $g_m(r)$  would be almost constant in the range of small  $r$  where  $g(r)$  is of interest. We shall see that this is true to a good degree with the experimental data

in this thesis.

# Chapter 4

## The wind tunnel experiment

In this chapter, we describe our experimental setup, procedures and analysis methods.

The chapter begins with an introduction to the turbulent flow of our choice — grid generated turbulence in wind tunnel. This is followed by a description of experimental details including a discussion of various assumptions made and related subtleties.

Experimental results shall be presented in the coming chapters (Chap. 5 and 6).

## 4.1 Background

### 4.1.1 Homogenous-isotropic turbulence

The Navier-Stokes equation is notoriously difficult to solve at high Reynolds number due to its nonlinearity (see e.g. Shinbrot, 1973). Moreover, since turbulent solutions are apparently chaotic, the detailed evolution of the velocity field is perhaps of less theoretical value compared to some form of statistical physics of turbulence.

Most theoretic-statistical understanding of turbulence to date is based on the idealized homogenous-isotropic turbulence. From a physicist's point of view, homogenous-isotropic turbulence plays the role much like point mass in Newtonian mechanics where it provides a good starting point for discovery of universal characteristics of turbulence itself and also how turbulence relates to other flow related phenomena (e.g. inertial particle dynamics). For this reason, homogenous-isotropic turbulence has been studied extensively in theory, experiment and numerical simulation. Due to its simplicity and the broadly available knowledge about it, we thus choose homogenous-isotropic turbulence as a starting point for the study of inertial particle clustering in turbulence.

### 4.1.2 Grid turbulence

Experimentally, homogenous-isotropic turbulence may be approximately achieved through what is called grid turbulence. Grid turbulence is typically generated in a wind tunnel where a cross-stream array of periodic obstructions (e.g. grid) is placed in the path of the otherwise uniform flow. Down-stream, the sheared flow develop into decaying yet nearly homogenous and isotropic turbulence.

## 4.2 Experimental setup and methods

A schematic diagram of our experimental setup is shown in Figure 4.1. The experiment was conducted in an open circuit, suction wind-tunnel in the DeFrees Hydraulics

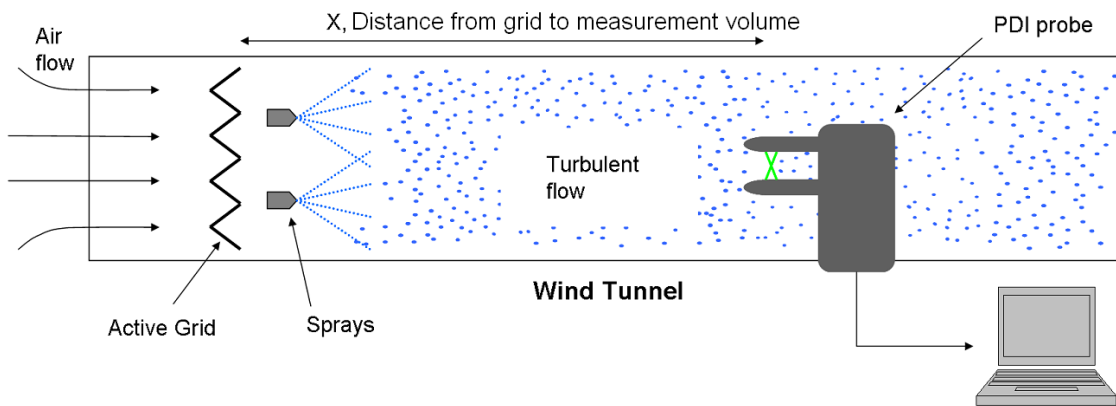


**Figure 4.1:** A schematic (not to scale), showing the experimental setup. Figure from supplementary material of Saw et al. (2008).



Laboratory (School of Civil and Environmental Engineering, Cornell University). The wind-tunnel is  $20m$  in length and  $0.95m \times 1.00m$  across (height  $\times$  width) with achievable mean velocity of 1 to 15 m/s. Air is sucked into the wind-tunnel by a fan (not drawn in figure) connected to the end of the wind tunnel (far right). Turbulence is generated via the active grid, and down stream of that four spray nozzles produce water droplets (inertial particles) in a broad range of sizes ( $\sim 1 - 50 \mu m$ ). Ample time is allowed for the development of the turbulence and also for interaction between droplets and turbulence before measurements of the droplet statistics and turbulent flow are made by the phase Doppler interferometer (PDI).

The PDI has been discussed in detail in Chapter 2. Here we proceed to discuss other specific aspects of the experimental setup.

### 4.2.1 Active grid and turbulence generation

The main advantage of an active grid over the traditional passive grid is in the generation of high intensity (thus high Reynolds number) turbulence. The wind-tunnel does not have the traditional flow stabilizers (e.g. screens, honeycomb) and contraction to condition the flow before it enters the test section. Instead, the flow is allowed to settle in the early section (left) of the wind tunnel before it passes through the turbulence generating active grid (Gylfason, 2006). Another advantage

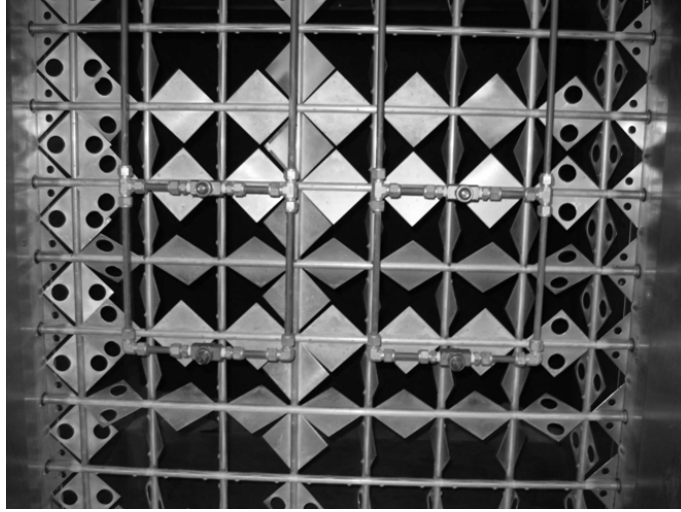


**Figure 4.2:** Picture showing the active grid and the configuration of the droplet sprays. Figure obtained from (Gylfason, 2006), courtesy of the author (See Appendix B).

of the active grid is that it produces large scale mixing which renders the flow input inhomogeneities insignificant further downstream where measurements are made.

The design of the active grid followed that of Makita (1991) with some modifications (picture in Fig. 4.2). It is made up of a series of horizontal and vertical rods with triangular winglets attached to them. Each rod is powered by a stepper motor and in operation would rotate with randomly switching directions. There are eight horizontal and seven vertical rods made of aluminium with outer diameter of 1.27 cm, and with mesh spacing,  $M$ , of 11.4 cm between neighboring rods (the outermost vertical rods are  $M/2$  from the tunnel walls). The winglets are also made of aluminium with thickness of 0.64 mm. Near the walls, ‘static winglets’ with calibrated holes are added to ensure good cross-stream homogeneity of the flow.

The active grid generates turbulence by inducing random shears in the traversing flow. These then developed into a nearly homogenous-isotropic turbulence further downstream ( $\gtrsim 25M$ ) with turbulent kinetic energy that decays with downstream distance following a power law.

The turbulence in the present setup is well characterized and was found to be homogeneous and isotropic enough for the present studies of small scale turbulence (at least as good as any passive grid turbulence, see Appendix A). An example of the turbulence spectrum obtained in the present setup can be found in Fig. 4.4. The implication of the addition of water sprays to the turbulence characteristics will be discussed in Section 4.2.3.

### 4.2.2 Droplet generation

We have chosen to study water droplets embedded in air due to its relevance to atmospheric clouds, which was the main motivation that initiated this work. The droplets are generated via four commercial air-atomizing sprays bought from Spraying Systems Co. (model: 1/4JN-SS, SU11DF-ss). The spray nozzles are evenly positioned just downstream of the active grid as shown in Figure 4.2. In operation, pressurized air and water are internally mixed inside the nozzle while upon exiting, air-induced breakup of water produces a jet of small water droplets. The droplet size distribution

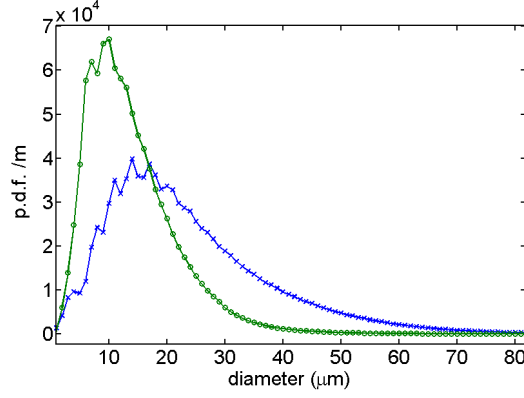


**Figure 4.3:** Probability density function of water droplets generated by the spray nozzles. The broader distribution (blue) is obtained when the water/air pressures are set to 32/32.5 psi ( $\pm 0.5$  psi). This setting was used in works whose results will be discussed in Chap. 5 (Cornell-1). The other distribution (green) that has smaller drops corresponds to conditions of water/air pressures equal to 40/35 psi and was used in works to be presented in Chap 6 (Cornell-2).

(diameter) is broad and is controlled by the pressure of the supplied air/water and is generally in the range of 1-50  $\mu\text{m}$  with a log-normal like distribution (see Fig. 4.3).

Distilled water is stored in a pressurized stainless steel container, pressurized by compressed air. The water and atomizing air pressures are regulated by electro-pneumatic controllers (Bellofram 3212), which use an (in-built) closed loop control to regulate the output pressure to be a linear function of the voltage of an analog control signal.

### 4.2.3 Influence of Sprays on turbulence

One legitimate concern is whether the jets from the spray and the presence of the droplets affect the background turbulent flow. The former seems to be avoidable as long as the flow rate of the tunnel itself is much greater than those of the jets and that the measurement is carried out far enough downstream of the sprays. Regarding the later, in our experiments the liquid-to-air volume (mass) ratio is less than  $2.3 \times 10^{-5}$  ( $4.8 \times 10^{-2}$ ). This has been shown to be sufficiently small (coupled with the fact that droplet sizes are smaller than  $r_k$ ) that flow modulation by the droplets can be ignored (Geiss et al., 2004).

However to be more certain, we did comparative measurements (at downstream distance most relevant to our experimental studies,  $X=3-5$  m) using hot-wire anemometry (HWA) with sprays turned off and using phase-Doppler interferometry (PDI) with sprays turned on\*. The results from the two instruments show agreement well within experimental error (an example is shown in Fig 4.4) corroborating the dilute limit assertion and show that the impact of the jets is negligible. Due to this finding, we have the option of characterizing the turbulent flow in the wind-tunnel using the HWA data (with sprays off) when the use of PDI data is inconvenient (e.g. does not have enough statistical convergence). This also allows us to use the extensive turbulence characterization from previous works using HWA (details in Appendix A).

---

\*Note: HWA is only suitable for fluid measurement without seeding while vice-versa for PDI.

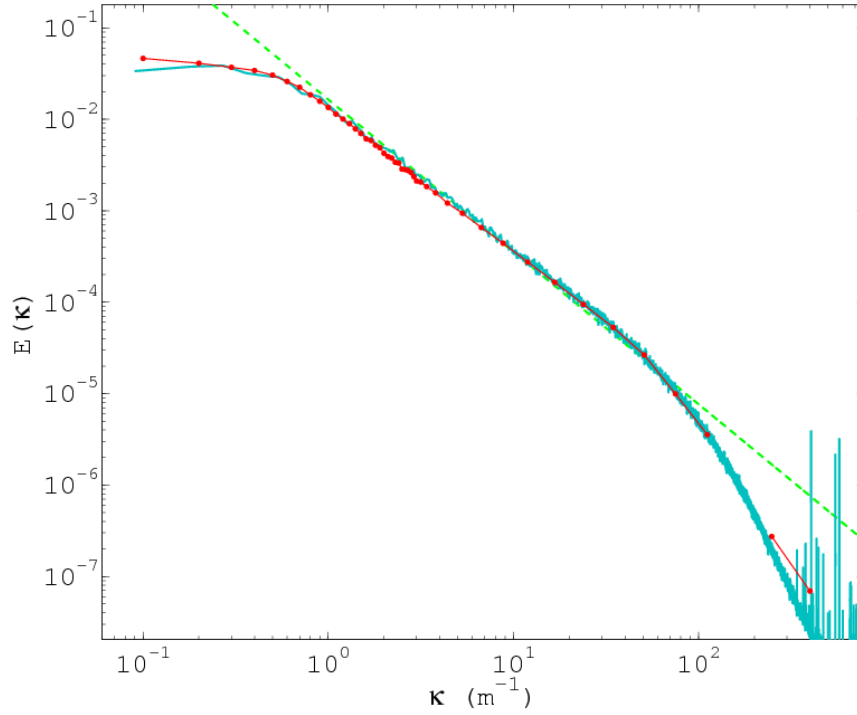


**Figure 4.4:** Energy spectra of turbulence at  $X=5\text{m}$ , fan-speed= $20\text{Hz}$ . Cyan continuous line is the result via HWA. Red with dots is the result via PDI (using small droplets ( $< 10\mu\text{m}$ ), we first obtained the longitudinal structure function of the droplet velocities from which the velocity autocorrelation function can be simply derived. The spectrum results from Fourier transform of the velocity autocorrelation. The spectrum was also averaged with exponentially increasing bins to reduce noise at high  $\kappa$ ). Green dotted line is defined as  $0.5 \varepsilon^{-2/3} \kappa^{-5/3}$ , where  $\varepsilon$  is obtained empirically from HWA data (this is the prediction of Kolmogorov (1941) theory for homogenous-isotropic turbulence). The ability to obtain turbulence spectrum via PDI that is so closely consistent with HWA is a remarkable finding.

In some cases, HWA data is preferable since they yield more direct and precise determination of the turbulence statistics (HWA does not use discrete particle and boasts high sampling frequencies).

#### 4.2.4 PDI positioning and particle equilibration

The position of the PDI from the grid,  $X$ , has to be far enough downstream in order to provide sufficient time for the development of the turbulence and for the particle dynamics to achieve equilibrium with the turbulence. In all our experiments,  $X$  is greater than 3 m, which gives the droplets  $\gtrsim 0.34$  s to equilibrate. This is equivalent to 0.5 to a few integral time scales of the turbulent flows ( $\tau_L$ ) and is in the order of  $10^2 \tau_\eta$  ( where  $\tau_\eta$  is the Kolmogorov time scale, cf. Sec. 1.1). All results shown in this thesis are for  $St \lesssim 1$  (thus  $\tau_p \lesssim \tau_\eta$ ) and it has been shown via direct numerical simulation (DNS) that in this parameter range the time for both the particle positions and velocity dynamics to achieve equilibrium with the flow is on the order of  $10\tau_\eta$  (see e.g. Cencini et al., 2006; Chun et al., 2005). Furthermore, a recent experiment (Yang and Shy, 2005) suggests that clusters of inertial particles are well developed (at least qualitatively) from initially uniform distribution given time of the order of  $10\tau_\eta$  (or even less in some cases; see the paper for details).

Through private communication with Prof. Lance. R. Collins (Cornell Univ.) and from our own experience, results from DNS suggest that finer features of inertial clustering take longer time to develop. Specifically, while the feature at scales  $\sim \eta$  and greater were found to equilibrate after a few  $10\tau_\eta$ , features at smaller scales take considerably longer time. This however has not been methodically observed in experiment. To this end, since our experiments do not resolve clustering features

smaller than  $\eta$ , it is thus safe to assume that what we observe has already achieved equilibrium.

Another closely related and perhaps more pressing question is whether one can consider the droplets to be interacting with stationary turbulence with quasi-constant mean energy dissipation rate ( $\varepsilon$ ) given that grid turbulence is decaying. To address this, we consider the decay rate of  $\varepsilon$  experienced by the droplets as they move downstream. Specifically, we calculate the fractional reduction of  $\varepsilon$  for every  $20 \tau_\eta$  (assuming that is the time needed for the droplets to equilibrate with the turbulence). Writing  $\beta_\varepsilon$  as the reduction, we have:

$$\beta_\varepsilon = \frac{|\frac{d\varepsilon}{dX}|U \times 20\tau_\eta}{\varepsilon} . \quad (4.1)$$

For the data reported here,  $\beta_\varepsilon$  is between 0.12-0.19. Therefore until this matter is further studied, our results should be interpreted with the caveat that the values of  $\varepsilon$  used are representative of a quantity that actually varies by up to  $\sim 10\%$ . Finally it is worth noting that in high Reynolds number turbulence,  $\varepsilon$  is a highly intermittent quantity, thus a 10% decay in its mean value may not be physically significant.



## 4.3 Data analysis

From the collected particle statistics we calculate the RDF (cf. Chap. 3) of each experimental set, which allows us to study the dependence of clustering on flow parameters ( $St$ ,  $R_\lambda$ , etc). This section discusses our methods of obtaining the RDF's experimentally.

### 4.3.1 Obtaining inter-particle distances from particle arrival times

A Phase Doppler interferometer (cf. Chap. 2) measures the arrival time, velocity and diameter of each detected particle. When particles share a strong average velocity, the series of arrival times can be transformed into a one dimensional distribution of particles in space. This idea is similar to Taylor's frozen turbulence hypothesis (see e.g. Tennekes and Lumley, 1972; Taylor, 1938) which states that when there is a strong mean flow, the spatial structures of the turbulence do not change appreciably while they are advected passed a fixed point in space. Thus, these structures are captured as a function of time by any Eulerian measurement (measurement carried out at a fixed point). In our case, one can write:

$$\Delta x_i = U \Delta t_i, \tag{4.2}$$

where  $U$  is the mean velocity component shared by droplets and background fluid motion;  $\Delta x_i$  are the inter-particle distances and  $\Delta t_i$  are the inter-particle arrival times. The error from invoking Taylor’s hypothesis will be discussed in Section 4.4.

### 4.3.2 Calculation of radial distribution function

Given a sample of inter-particle distances, we calculate the RDF using the 1D version of Eq. 3.7 with finite interrogation volume (Sec. 3.2.1) and full edge treatment (Sec. 3.2.2). The correct formulation is given by:

$$g(r) = \frac{N_p(r)}{\left[ N_{in}(r) + \frac{1}{2}N_{ex}(r) \right] \Delta r (N - 1)/L}, \quad (4.3)$$

where  $N_p(r)$  is the total number of particle pairs separated by distance  $r \pm \Delta r/2$ ,  $N_{in}(r)$  is the number of interior particles — particles that are at least at distance  $r$  from sample edges,  $N_{ex}(r)$  is the number of edge particles — particles closer than  $r$  from the sample edges,  $N$  is the total number of particles in the sample and  $L$  is the total length of the sample.

To see how Eq. 4.3 results from doing full edge treatment to 1D data, let us imagine a plot of particle positions along a horizontal line from left to right. Following the procedure outlined in Section 3.2.2, we treat the interior and edge particles

separately using Eq. 3.7, reproduced here for the 1D case:

$$g(r) = \frac{\psi(r)/N_t}{(N-1)2\Delta r/L}, \quad (4.4)$$

where  $\psi(r)$  is the sum over ‘numbers of particles found at distance  $r$  from each trial particle’. We have written  $L$  in place of  $V$  (the full sample volume) and  $2\Delta r$  in place of  $\delta V_r$  (in 1D, an isotropic shell reduces to two symmetric bins).

We use all particles as trial particles and apply a full edge treatment in order to achieve maximum statistical convergence. Each interior trial particle provides us with two interrogation volumes  $\Delta r$ , one on its left and one on its right. However, for each edge particle, there is only one such  $\Delta r$ , since the data is truncated on the other side. Thus when combined, we obtain a formula for  $g(r)$  much like Eq. 4.4 but with the total number of interrogation volumes  $2N_t$  substituted with  $2N_{in} + N_{ex}$ . This coupled with the fact that  $\psi(r)$  becomes  $2N_p(r)$  when all particles are used in the calculation, gives us Eq. 4.3.

## 4.4 Error analysis

In this work we are interested in the radial distribution function,  $g(r)$ . To calculate  $g(r)$  we need the inter-particle distances of the detected droplets. In practice, the

PDI registers droplet arrival times. The inter-droplet distances are then obtained from this time series via a time-to-space transformation, equivalent in principle to the Taylor frozen turbulence hypothesis: Eq. 4.2. After that,  $g(r)$  is calculated using Eq. 4.3. Sources of error in estimating  $g(r)$  include:

1. Bias from using finite interrogation volumes. As discussed in Sec. 3.2.1, this only affects  $g(r)$  calculated from 2D and 3D data. In our case, the effect of using finite  $\Delta r$  is just a simple averaging of  $g(r)$  over  $\Delta r$ , which washes out possible fine features (not of interest to present studies).
2. Error in measurement of droplet arrival times. Particle arrival time accuracy was found to be better than  $\simeq 3.5 \mu s$  (see Sec. 2.3.3), which we shall see is just a few percent of the smallest inter-droplet arrival time studied. This error has the same effect as the next error to be discussed but it is one order smaller in magnitude. We thus ignore this in the error analysis.
3. Error from time-space transformation. The use of Eq. 4.2 essentially assumes that all droplets are advected downstream with velocity equal to the mean flow velocity  $U$ . This is, by definition, incorrect because droplets are embedded in a turbulent flow. The resulting estimates of inter-droplet distances,  $\Delta x$ , thus contain random errors. The resulting error is on the order of  $(u/U) \Delta x$ , where  $u$  is the r.m.s velocity fluctuation. In our experiments,  $u/U$  never exceeds 20%, thus resulting in errors of less than 20% in  $\Delta x$ .

Since we are ultimately interested in  $g(r)$ , which is derived from counting the number of droplet pairs separated by distances satisfying  $r - \delta r/2 < \Delta x < r + \delta r/2$  (cf. Eq. 4.3), random errors in  $\Delta x$  imply that some droplet pairs are wrongly accounted into neighboring inter-droplet-distance bins. This is essentially equivalent to a low-pass filtering on  $g(r)$ . However, since we report coarse grained RDF (with finite interrogation volumes,  $\Delta r > 0.1r$ ), the probability of particle pairs being wrongly binned is suppressed, and therefore the low-pass filtering effect of this error is masked. Because of the loss of possible fine features due to low-pass filtering or  $r$ -coarse graining, the conclusions reached in this study, such as observations of Stokes similarity, are limited to the coarse trends of the  $g(r)$  curves.

Lastly, due to the geometry of the problem there is an additional, more subtle bias that arises from the use of the time-space transformation, to be discussed in point 5 below.

4. Finite sample volume and one-dimensional sampling. The PDI has a measurement cross-section with height  $\approx 230\mu m$  and width of roughly 2-3 times the slit aperture (selectable between 50, 100, 200, 500, 1000 $\mu m$ ). This has the implication that the  $\Delta x$  estimated via Eq. 4.2 has a tendency to underestimate the true inter-particle distance. Proceeding from this line of reasoning, Holtzer and Collins (2002, hereafter as H&C) showed that  $g(r)$  obtained from one-dimensional sampling of a droplet distribution could systematically deviate

from the true (three dimensional)  $g(r)$  due to averaging effects from a finite instrument sampling volume or resolution. The same study also shows that this deviation is negligible for  $r$  greater than the sample volume dimensions. In this work, we have reported only  $g(r)$  at scales satisfying this condition. Furthermore, following the analysis of H&C we have estimated that at the scales reported in this thesis the maximum decrement of any single point of  $g(r)$  from its 3D counterpart is  $\approx 0.4$ , most deviations in the  $g(r)$  curves due to this spatial averaging are much smaller than this. For the results we shall present in Chapter 5, this bias is within the average statistical error and thus is not treated. The same cannot be said of results in Chapter 6.

5. An additional error from the time-space transformation. A similar bias to that described in point 4, but not discussed in H&C, results from uncertainty in  $\Delta x$  due to the time-to-space transformation. A simplistic way to explain this is that because the use of Eq. 4.2 does not allow for any displacement of droplets in the plane normal to the mean flow direction, it always tends to underestimate the true particle separation distance: Lateral droplet motion during the time interval between detection of two droplets is not measured, and this results in an underestimate of the inter-particle distance. It is similar to the bias discussed in H&C in that the error results essentially from a collapse of three spatial dimensions into one. However, starting from an error of 20% in  $\Delta x$ , we estimate that the ‘scale of averaging’ is less than 4% of  $r$ , which implies that the

resulting bias is negligible at small  $r$ . Even at  $r \sim 10 r_k$  (the largest scales at which inertial clustering is observed), this bias is less than half the magnitude of that resulting from finite measurement volume. The combined effect is thus still insignificant for the results presented in this thesis.

6. Shot noise. Because  $g(r)$  is derived from counting droplets within a particular interval (cf. Eq. 4.3), it is subjected to Poisson statistics. From this, one can derive the sampling uncertainty to be:

$$\sigma_{g(r)} = \sqrt{\langle g(r) \rangle / N n_p \Delta r}, \quad (4.5)$$

where  $N$  is the total number of droplets detected in the whole experiment,  $n_p$  is the globally averaged droplet density, and  $\Delta r$  is the width of the interrogation bin. A large sample is usually required to minimize this noise. Even with that, this noise dominates the error in our  $g(r)$  results in Chapter 5. Therefore in that chapter, we will show our error bars as  $2\sigma$  in the plots of  $g(r)$ , which we assume as an upper bound of the combined effect of sampling and other less significant errors. In Chapter 6 however, only one  $\sigma$  is used in the error bars.

# Chapter 5

## Stokes similarity in inertial clustering (a published paper)

In this chapter, we present the major results from our earlier experiments (done in winter of 2004) in a form of a published paper. The paper was published in Physical Review Letters under the title: Inertial Clustering of Particles in High-Reynolds-Number Turbulence (Saw et al., 2008)\*. Notes for readers: Reading the introduction section in this paper is optional since most of the contents has been discussed in earlier chapters. Cross references and formats of the paper has been modified to be compatible with the organization of this thesis.

---

\*Reprinted here with permission (see Appendix B).



## Abstract

We report experimental evidence of spatial clustering of dense particles in homogeneous, isotropic turbulence at high Reynolds numbers. The dissipation-scale clustering becomes stronger as Stokes number increases and is found to exhibit similarity with respect to the droplet Stokes number over a range of experimental conditions (particle diameter and turbulent energy dissipation rate). These findings are in qualitative agreement with recent theoretical and computational studies of inertial particle clustering in turbulence. Due to the large Reynolds numbers a broad scaling range of particle clustering due to turbulent mixing is present, and the inertial clustering can clearly be distinguished from that due to mixing of fluid particles.

## 5.1 Introduction

It is a common observation that a ‘passive’ tracer injected non-uniformly into a turbulent flow (e.g. a substance that only marks but does not modify the flow, such as smoke in air or milk in tea) will soon be stirred and mixed by the random vortices in the turbulence until it attains a uniform distribution. Such high mixing power is in fact a hallmark of turbulent flow (Tennekes and Lumley, 1972). One might reasonably ask if the same holds true when the substance is no longer a perfect fluid tracer, such as one that consists of macroscopically discrete particles possessing finite

inertia, like the distribution of water droplets in turbulent clouds (e.g., actively convective cumulus clouds). In fact, water droplets with mass density  $10^3$  times greater than that of air are dynamically stubborn and do not exactly follow the motion of the host fluid. As a result, these ‘inertial particles’ should have a steady state spatial distribution differing from that of a uniform field of fluid particles (Eaton and Fessler, 1994; Elperin et al., 1996; Maxey, 1987; Sundaram and Collins, 1997; Balkovsky et al., 2001).

The inertial clustering phenomenon has implications for a wide range of problems in nonlinear and fluid dynamics, including the formation of rain by droplet collisions in atmospheric clouds (Falkovich et al., 2002; Pinsky and Khain, 1997; Shaw, 2003). Because the droplet collision rate is proportional to droplet density squared, spatial correlations due to inertial clustering can result in accelerated rain formation. Considerable progress has been made in computational and theoretical studies of inertial clustering, but experimental results are sparse (Aliseda et al., 2002; Wood et al., 2005) and the nature of inertial clustering at high Reynolds numbers remains an open problem (Collins and Keswani, 2004). Qualitatively, inertial clustering can be understood as the result of particles being centrifuged out of turbulent vortices and thus congregating in regions of high strain (Eaton and Fessler, 1994; Sundaram and Collins, 1997). Turbulence is a multi-scale process in which energy injected at large scales (of order  $l$ ) ‘cascades’ to progressively smaller scales through nonlinear interactions such as vortex stretching. Over most of these spatial scales, known as the

inertial range, fluid inertia dominates over viscous forces; the scales at which viscosity becomes important lie in the dissipation range. The clustering of inertial particles is significant at dissipation scales and below because it is in this range that turbulent vorticity and accelerations are strongest (Wang and Maxey, 1993; Falkovich et al., 2002; Chun et al., 2005). It should be noted, however, that alternate interpretations and approaches exist (Chen et al., 2006; Duncan et al., 2005; Elperin et al., 2002; Ghosh et al., 2005; Zaichik and Alipchenkov, 2003), adding impetus to the need for experimental data capable of elucidating mechanisms and constraining theory. To that end, it is the purpose of this paper to describe an experimental study of inertial clustering and its dependence on particle size and turbulence conditions at high Reynolds numbers.

Suitable quantification of clustering is provided by the particle pair correlation function  $\eta(r)$  (Sundaram and Collins, 1997; Shaw, 2003), whose magnitude characterizes the strength of clustering at scale  $r$ . Intuition on the properties of  $\eta(r)$  can be gained by examining how it is calculated in our experiment for one-dimensional sampling of the particle spatial distribution (Holtzer and Collins, 2002):

$$\eta(r) = \frac{\tilde{Q}(r)/\delta r}{Q/L} - 1, \quad (5.1)$$

where  $\tilde{Q}(r)$  is the number of particle pairs separated by a distance within  $[r - \delta r/2, r +$

$\delta r/2$ ];  $Q$  is the total number particle pairs in the sample;  $L$  is the sample length. Previous theoretical and Direct-numerical-simulation studies (Balkovsky et al., 2001; Chun et al., 2005; Falkovich et al., 2002; Reade and Collins, 2000; Kerstein and Krueger, 2006), suggest that under ideal conditions (homogenous and isotropic turbulence, single-size particle population, particle-fluid coupling following Stokes’s law, dilute particle loading, and negligible role of gravity)  $\eta(r)$  satisfies a simple power law<sup>†</sup>:

$$\eta(r) \propto (r/r_k)^{-f(St)}, \quad (5.2)$$

where  $r_k$  is the Kolmogorov length scale (characterizing the dissipation range), and  $f(St) > 0$  increases monotonically with  $St$  for  $St < 1$ . Here, the Stokes number  $St$  characterizes the particle’s inertial response to the flow and is defined as the ratio of the particle inertial response time  $\tau_d$  to the Kolmogorov time  $\tau_k$  (coherence time scale for the dissipation range) (see e.g. Tennekes and Lumley, 1972):

$$St = \frac{\tau_d}{\tau_k} = \frac{1}{18} \left( \frac{\rho_d}{\rho} \right) \left( \frac{d}{r_k} \right)^2, \quad (5.3)$$

where  $\rho_d$  is the particle mass density,  $d$  is the particle diameter, and the Kolmogorov

---

<sup>†</sup>While it is usually stated that the theories apply to the limit  $r/r_k \ll 1$ , in fact the power-law form is predicted to continue to the correlation scale of velocity gradients. That scale is on the order of  $r/r_k \sim 10$  (see A. S. Monin and A. M. Yaglom, *Statistical Fluid Mechanics: Mechanics of Turbulence*, Vol. II (MIT Press, 1975), Sec. 23.4 and Fig. 77; and S. G. Saddoughi and S. V. Veeravalli, J. Fluid Mech. **268**, 333 (1994), Sec. 3.2.1 and Fig. 10.

microscale  $r_k = (\nu^3/\varepsilon)^{1/4}$  depends on the kinematic viscosity  $\nu$  of the fluid (air) and the turbulent kinetic energy dissipation rate  $\varepsilon$ .

## 5.2 Experiment

The experimental setup, which is further detailed in chapter 4, consists of a wind tunnel with well-characterized turbulence, sprays for particle generation, and a particle detector. Homogenous and nearly isotropic turbulent flow is generated by a motorized ‘active grid’ capable of achieving high Reynolds number (Mydlarski and Warhaft, 1996; Ayyalasomayajula et al., 2006). Water droplets are introduced via four spray nozzles, with the resulting size distribution being broad ( $\bar{d} = 22 \mu\text{m}$ ,  $\sigma_d = 13 \mu\text{m}$ ). Downstream, a phase-Doppler interferometer (PDI) (Chuang et al., 2008) simultaneously measures the diameter ( $d_i$ ), downstream speed ( $v_i$ ), and arrival time ( $t_i$ ) of all droplets that traverse its view volume (which has cross-section of approximately  $150 \mu\text{m} \times 210 \mu\text{m}$ ). Table 5.1 lists the flow parameters for the various experiments carried out in the wind tunnel: the experiments differ in  $R_\lambda$  and  $\varepsilon$ , and therefore have different  $r_k$ . Each experiment is referred to by a name based on the distance downstream from the active grid (in meters) where measurements are taken and the speed of the fan (in Hz) that drives the wind tunnel.

The PDI is stationed far enough downstream ( $X = 3$  and  $5$  m, where  $X$  is the

distance from the active grid) such that the small scale spatial distribution of the droplets reported here have ample interaction time with the turbulence to achieve equilibrium. This follows from the fact that the transit time of droplets is much larger than the Kolmogorov time scale (at least  $200\tau_k$ ; see Sec. 4.2.4 for additional details). To obtain the droplet spatial distribution ( $x_i$ ) needed for the evaluation of  $\eta(r)$  using 5.1, we adopt a method equivalent to Taylor’s frozen turbulence hypothesis (Tennekes and Lumley, 1972) in which the time series is converted into a spatial one ( $x_i = t_i U$ ). Within each experiment, the dependence of clustering on particle inertia is studied by selecting droplets from a small range of Stokes numbers  $St \pm \Delta St$  and then evaluating  $\eta(r)$  for that subset of droplets. In practice,  $\Delta St$  is chosen such that acceptable counting statistics are obtained. Stokes numbers are calculated using Stokes drag (cf. Eq. 5.3), which is accurate to within 10% for the largest droplet diameters used in this study ( $\approx 50 \mu\text{m}$ ). The uncertainty in this study is dominated strongly by the ‘shot noise’ in the value of  $\eta(r)$  due to droplet counting statistics, as detailed in Sec. 4.4.

### 5.3 Results and Discussion

The essential experimental results on particle clustering are presented in Figs. 5.1 and 5.2, which depict the dependence of  $\eta(r)$  on  $\hat{r} \equiv r/r_k$  for various flow conditions (in log-log coordinates, cf. Eq. 5.2). Fig. 5.1 illustrates how  $\eta(r)$  changes with  $St$

Experiment	3m20Hz	3m30Hz	5m20Hz	5m30Hz
$R_\lambda$	520	660	440	590
$\varepsilon$ ( $\text{m}^2 \text{s}^{-3}$ )	1.6	5.4	0.6	2.0
$U$ ( $\text{m s}^{-1}$ )	4.69	6.78	4.59	6.81
$u/U$	0.17	0.18	0.12	0.13
$r_k$ ( $\mu\text{m}$ )	210	150	270	200
$St = 0.3$	18, 0.14	13, 0.05	23, 0.30	16, 0.10
$St = 0.7$	27, 0.32	20, 0.13	35, 0.69	25, 0.26
$St = 1.1$	34, 0.50	25, 0.20	43, 1.04	32, 0.42
$St = 1.5$	39, 0.66	29, 0.27	51, 1.46	37, 0.56

**Table 5.1:** Experiment flow parameters, where  $R_\lambda$  is the Taylor-scale Reynolds number,  $U$  is the mean and  $u$  is the rms fluctuation of the flow speed along the wind tunnel. The last 4 rows are the droplet diameters (in  $\mu\text{m}$ ) and corresponding gravitational settling parameters,  $S_g$ , for the  $St$  bins used in the data analysis.

within a single experiment (3m30Hz). We note that strong clustering is mainly limited to scales  $\hat{r}$  on the order of 10 and below (see footnote just before Eq. 5.2), and that clustering is stronger for droplets of larger  $St$ . Onset of clustering in the dissipation range, and monotonic increase of clustering with  $St$  are consistent with theory for  $St \ll 1$  (Balkovsky et al., 2001; Chun et al., 2005)). Within the inertial range, on the order of  $10 \lesssim \hat{r} \lesssim 1000$ , the correlation functions  $\eta(\hat{r})$  show weakly decreasing clustering with increasing  $\hat{r}$ , and then fall off more strongly at larger  $\hat{r}$ . This inertial-range behavior typifies correlations arising from mixing of a passive tracer by turbulence (e.g.,  $\eta(r)$  scaling as  $1 - (r/l)^{2/3}$ . See e.g. Lumley and Panofsky, 1964, Sec. 2.9). Essentially, large-scale inhomogeneities in the droplet spatial distribution induced by the spray injection are subsequently stretched and distorted in the turbulent cascade, as the droplets are advected downstream.

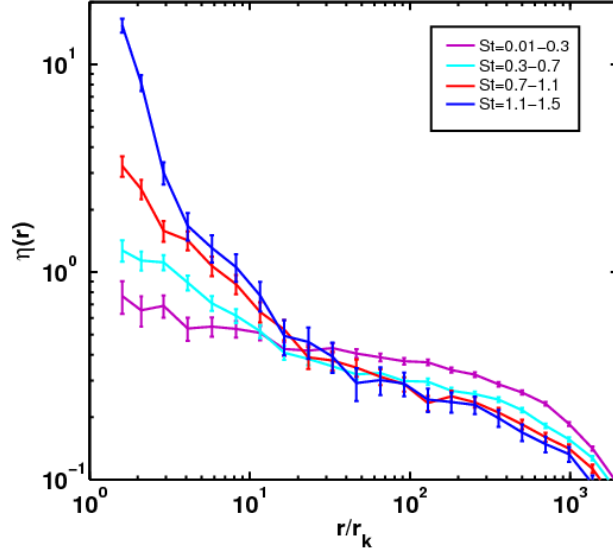


**Figure 5.1:** (color online)  $\eta(r)$  versus  $\hat{r} (\equiv r/r_k)$  with error bars of  $2\sigma_{\eta(r)}$ , and with  $\eta(r)$  parameterized by  $St$  from experiment 3m30Hz. Consistent with theoretical expectations,  $\eta(r)$  increases in magnitude with increasing Stokes number in the dissipation range. Each line is  $\eta(r)$  calculated from droplets within the specified range of  $St$  (from bottom to top corresponding to successively larger  $St$ ). The errors are evaluated as  $2\sigma_{\eta(r)}$  (details in text)

Droplets with different diameters but equal Stokes numbers from the experiments are compared in Fig. 5.2 (zoomed scale), demonstrating ‘Stokes similarity’ consistent with scaling arguments for inertial clustering. The  $\eta(r)$  values for the same  $St$  range coincide to within the experimental error even though each is obtained from different flow conditions and droplet sizes (see Table 5.1). In obtaining such comparison of the dissipation-range clustering, large-scale correlations resulting from inertial-range mixing must be removed. To that end, the  $\eta(r)$  curves in Fig. 5.2 are normalized such that they coincide in the inertial subrange ( $\hat{r} \sim 100$ , see Sec. 5.4 for details). Finally, we note that although Stokes similarity is evident in Fig. 5.2, for one



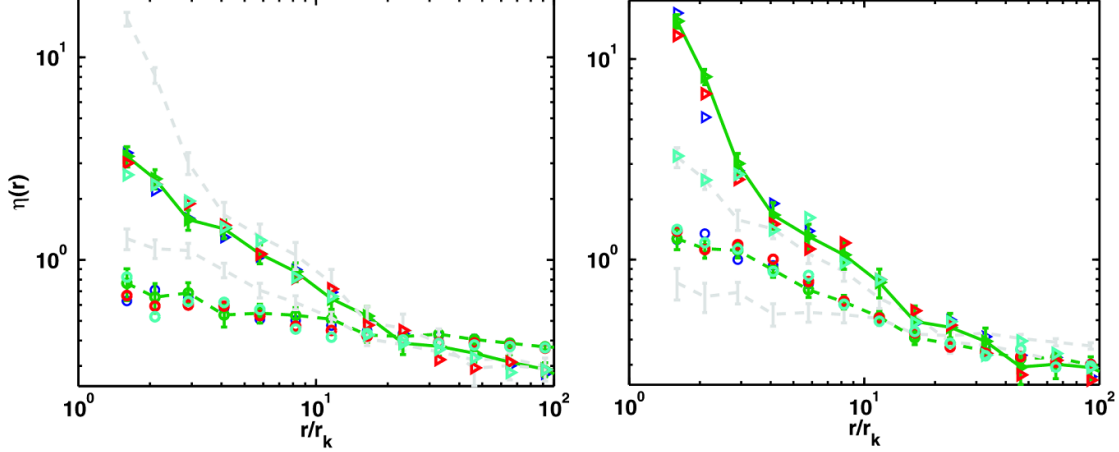


**Figure 5.2:** (color online) Stokes-similarity results shown in two panels for clarity. **Left:**  $St$ -similarity for droplets with  $St=0.01-0.3$  (circles) and  $St=0.7-1.1$  (triangles). Plots for other  $St$  groups from fig. 5.1, 3m30Hz, are shown in the background for comparison. The marker colors represent  $\eta(r)$  from different experiments (blue=3m20Hz, green=3m30Hz, red=5m20Hz, cyan=5m30Hz). **Right:**  $St$ -similarity for  $St=0.3-0.7$  (circles) and  $St=1.1-1.5$  (triangles).

data set a discrepancy is observed for  $1.1 < St < 1.4$ , suggesting that the behavior of droplets with  $St > 1$  merits future investigation<sup>‡</sup>.

A further observation from Fig. 5.2 is the apparent power-law dependence of  $\eta(r)$  in the dissipation range (for  $St \leq 1.1$  data). Although this observation is rather tentative given the level of uncertainty and the limited window of resolvable scales showing constant slope, it suggests that the power law is realized even for droplets with finite Stokes number. Theoretically, the power law is valid for  $St \ll 1$  (see Eq. 5.2) but computational work suggests that the power-law dependence continues to hold for  $St \lesssim 1$  as well (Reade and Collins, 2000), consistent with our results. Detailed

<sup>‡</sup>We later found that this is caused by a problem with the PDI probe at that time which have the tendency to register big drops such as these more than once. This causes spurious increase in the RDF as seen here; except for the 5M30Hz case, which we think is free from this problem.

theoretical and computational accounting of the more realistic case of a finite range of Stokes numbers (i.e.,  $\Delta St > 0$ ) is still lacking, thus a direct comparison of our results with theory is not possible here. Finally, quantitative comparison of theoretical and measured power-law exponents will require greater resolution at low Stokes numbers since the theory is strictly applicable to  $St \ll 1$ .

Recently Wood and colleagues (Wood et al., 2005) also addressed inertial clustering in an experiment with  $R_\lambda = 230$  and obtained results in qualitative agreement with computational work. We are especially interested, however, in the implications of inertial clustering for cloud droplets and its possible influence on the development of precipitation (Shaw, 2003). For geophysical problems the open question of Reynolds number dependence (Collins and Keswani, 2004) is crucial, and therefore we have utilized an experimental system allowing us to attain Reynolds numbers approaching  $10^3$ . This leads to a clear separation of scales (i.e.,  $l/r_k \approx 2000$ ) and reveals the relative roles of inertial-range mixing and dissipation-range clustering due to droplet inertia. This is critical in allowing comparison between controlled laboratory data such as these, to similar particle-counting measurements in clouds, where turbulence characterization is considerably more difficult (Brennguier et al., 1998; Kostinski and Shaw, 2001; Lehmann et al., 2007; Pinsky and Khain, 2003).

Yet to be studied methodically is the role of gravitational settling in inertial clustering. Theoretical findings on this matter are sparse and the problem remains

open. Our experiments have large  $\varepsilon$  relative to many atmospheric clouds, thus the role of gravity is relatively less important. Theoretically, the importance of gravity is expected to scale as the gravitational sedimentation parameter  $S_g \equiv \tau_k/\tau_g$ , where  $\tau_g$  is the time required for a droplet to fall over a distance of  $r_k$  at its terminal speed. In our experiments, the values of this quantity (cf. Table 5.1) suggest that the role of gravity ranges from small ( $S_g \sim 0.01$ ) to significant, but not dominant ( $S_g \sim 1$ ). However, the observation of Stokes similarity in our results (despite the fact that  $S_g$  changes by five to six-fold in each  $St$  range) suggests that the role of gravity in this work is limited relative to that of turbulence for the range of conditions considered.

The experiments described here provide support for the inertial clustering mechanism, and are in qualitative agreement with theoretical predictions. Clustering distinct from that expected for mixing of fluid particles is observed at dissipative scales, where fluid acceleration and vorticity reach a maximum. The magnitude of the clustering increases monotonically with droplet  $St$ , for  $St \lesssim 1$ , where  $St$  is a parameter characterizing coupling between particles and the fluid. Finally, under distinct flow conditions and with varying droplet sizes, the dissipation-range clustering is observed to exhibit Stokes similarity.

## 5.4 Supplementary: Large scale spatial inhomogeneity of particle density and how to correct for it

Figure 5.3 shows RDF's of particles with  $St = 0.1 \rightarrow 0.5$  from various experimental runs (directly calculated from the data without any extra normalization). Each RDF curve has a power-law like region at the smallest scales ( $r/r_k \leq 10$ ), followed by a plateau region at  $r/r_k \simeq 50 \rightarrow 100$ , and then rapid fall-off region at still larger scales. The RDF's measured at the same downstream distance are Stokes similar (coincide with each other). On the other hand, it is clear that the RDF's measured at  $3m$  downstream of the grid (the triangles) lie consistently above those measured  $5m$  downstream counterparts (the circles). As mentioned in Sec. 5.3, we interpret the presence of a 'shoulder region' (plateau then fall off at large scales) in the RDF curve as due to large scale inhomogeneity in the spatial distribution of the droplets, that is not part of inertial clustering. The fact that the plateau in RDF measured at  $5m$  is lower than that in RDF measured at  $3m$ , implies that such inhomogeneity is diminishing as the droplets are advected downstream<sup>§</sup>. The most likely source for this inhomogeneity is the residual inhomogeneity due to droplet injection that is not yet fully homogenized by turbulent mixing as described in Sec. 3.3.2. The time scale for turbulence mixing is close to the turbulence large eddy turnover time (also called integral time scale) and in all our measurements the particles only has a

---

<sup>§</sup>We also have data at  $8m$  downstream that has an even lower plateau region.

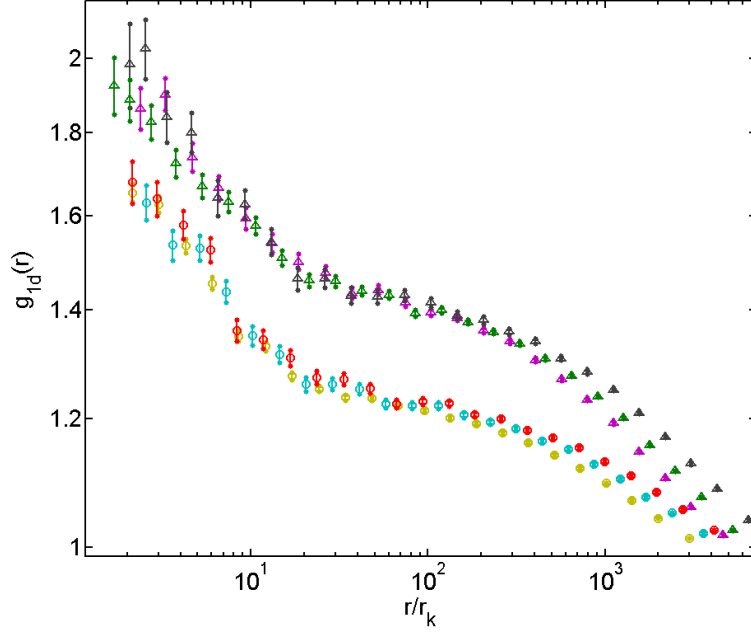


**Figure 5.3:** Error-bar plots of RDF ( $\equiv \eta(r) + 1$ ) for  $St = 0.1 \rightarrow 0.5$  from various experimental runs (in logarithmic axes). Colors represent different experimental runs: purple is 3m25Hz; green is 3m30Hz; black is 3m40Hz; gold is 5m20Hz; cyan is 5m25Hz; red is 5m40Hz. In addition, to aid differentiation, results from 3 *m* and 5 *m* downstream are marked as triangles and circles respectively. The present of a ‘shoulder region’ at  $r/r_k \geq 50$  is likely the result of large scale inhomogeneity in the spatial distribution of droplets (see text).

few eddy turnover times between injection and measurement. It is thus likely that the homogenizing action of turbulent mixing on the initially inhomogeneous field of particles is not yet complete, and this is captured by the RDF as a shoulder region that diminishes with time as mixing progresses.

The fact that the RDF’s measured at the same downstream distance still show Stokes similarity despite the shoulder regions is best explained by the fact that inertial clustering occurs at small scales that are well separated from the scales of the large scale inhomogeneity, and this leads to the result that the RDF signature of inertial

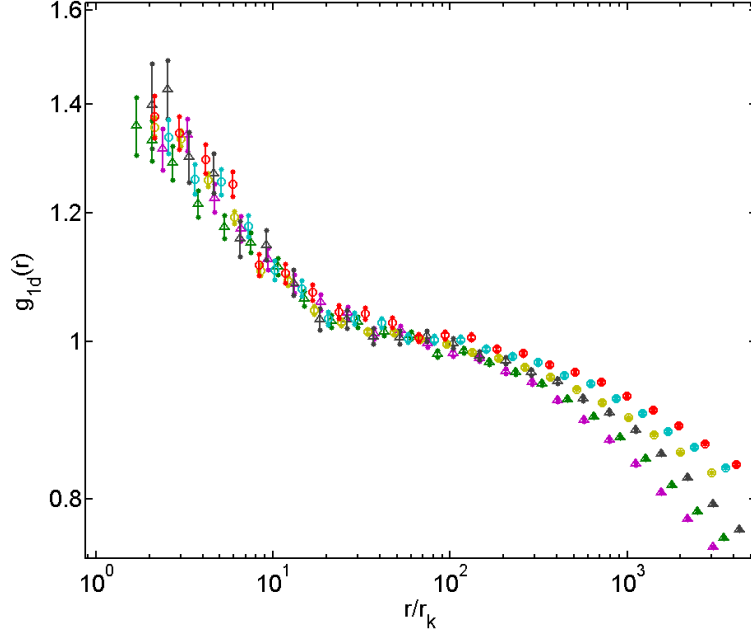


**Figure 5.4:** Error-bar plots of corrected RDF for  $St = 0.1 \rightarrow 0.5$  from various experimental runs (in logarithmic axes). Each RDF is multiplied by a constant factor such that its values at  $r/r_k \simeq 80$  are equal to one. Colors represent different experimental runs: purple is 3m25Hz; green is 3m30Hz; black is 3m40Hz; gold is 5m20Hz; cyan is 5m25Hz; red is 5m40Hz. In addition, to aid differentiation, results from 3m and 5m downstream are marked as triangles and circles respectively. The RDF's show clear evidence of Stokes similarity in their average steepness at small scales ( $r/r_k \leq 10$ ).

clustering is still intact but its magnitude gets multiplied by a constant factor (see Sec. 3.3.2 for details, especially discussion around Eq. 3.23).

In light of Sec. 3.3.2, we now attempt to remove the influence of the large scale inhomogeneity on the RDF's. Figure 5.4 shows the same set of RDF's as the ones shown in Fig. 5.3 but each is vertically shifted (multiplied by a constant factor) so that its values around  $r/r_k = 80$  are equal to one. The RDF's show clear Stokes similarity after this simple treatment.

To conclude, through a combination of observation and theoretical reasoning, we are convinced that the shoulder region in the measured RDF from our experiment is a signature of large scale inhomogeneity and we have found a way to isolate it from the RDF signature of inertial clustering that we are interested in. However, we must point out that this interaction between large scale mixing and inertial clustering merits further (more detailed) study.

## Chapter 6

# Quantitative comparison between experiment, simulation and theory

In the previous chapter, we have shown that our experimental results support certain qualitative (and semi-quantitative) predictions of theories and simulations. Here we present a more detailed quantitative comparison of our experimental findings with those from theory and direct numerical simulations (DNS).

Direct comparison of experimental findings with available theoretical and simulation studies to date is likely to be ambiguous and misleading. This is because



in our experiments (as in most realistic settings of practical interest), inertial particles are inevitably poly-disperse (having more than one size), while theoretical and simulation studies to date only consider mono-disperse (see e.g. Balkovsky et al., 2001; Chun et al., 2005; Cencini et al., 2006) and bi-disperse particles (Chun et al., 2005). As we shall see, the RDF signature of inertial clustering is a strong function of poly-dispersity.

In order to make more meaningful comparisons, we initiated a set of DNS studies involving poly-disperse particles\*. This allows us to compare our experimental findings directly with the DNS results in the poly-disperse and bi-poly-disperse† settings. This is coupled with a direct comparison of the exact same DNS results with theory in the mono-disperse and bi-disperse settings. Under this approach, the DNS study serves as a bridge for an indirect comparison between theory and experiments.

In addition, we shall also use our results (DNS and experimental) to address several questions about the nature of inertial particle clustering in this chapter. Here we list the major questions:

1. What are the essential consequences of poly-dispersity on inertial clustering ?
2. How does the pre-factor ( $c_0$ ) in the power-law model of the RDF relate to other

---

\*This was done in collaboration with colleagues from Cornell University, New York. The simulation was carried out by Juan Salazar and Dr. Lance Collins (both at Cornell). Our role was mainly in the initiation of the effort and post-analysis of the simulation outputs.

†Involving two sets of (different  $St$ ) poly-disperse particles.

quantities ?

3. Does the RDF show asymptotic behavior in the limit of large Reynolds number ?

## 6.1 Direct Numerical Simulation (DNS)

This section describes the simulation performed and is similar to descriptions found in two papers (Salazar et al., 2008; Collins and Keswani, 2004) published by the colleagues directly involved in the simulation.

### 6.1.1 Simulating the fluid turbulence

We simulate homogenous and isotropic turbulence inside a three-dimensional cubic domain with length  $2\pi$  along each side (arbitrary simulation units) with periodic boundary condition. The fluid flow is obtained as a solution to the incompressible Navier-Stokes equations and corresponding continuity equation:

$$\begin{aligned}\frac{\partial \mathbf{u}}{\partial t} + \mathbf{u} \cdot \nabla \mathbf{u} &= -\frac{1}{\rho} \nabla P + \nu \nabla^2 \mathbf{u} + \mathbf{F} \\ \nabla \cdot \mathbf{u} &= 0\end{aligned}\tag{6.1}$$

$R_\lambda$	$u'$	$\varepsilon$	$\nu$	$L$	$\lambda$
$143 \pm 4$	1.68	$0.32 \pm 0.02$	$\sim 0.002$	$1.38 \pm 0.04$	$0.302 \pm 0.009$

$r_k$	$T$	$\tau_k$	$\Delta t$	$N_{grid}$	$k_{max} r_k$
$0.0128 \pm 0.0002$	$0.82 \pm 0.02$	$0.08 \pm 0.002$	$1 \times 10^{-3}$	$256^3$	$\geq 1.5$

**Table 6.1:** Turbulence parameters in arbitrary units (except the first and last, which are dimensionless) in this DNS.  $R_\lambda$  is the Taylor microscale Reynolds number,  $\varepsilon$  the turbulent energy dissipation rate,  $u'$  the turbulent r.m.s. velocity,  $\nu$  the fluid kinematic viscosity,  $L$  the integral length scale,  $\lambda = u' \sqrt{15\nu/\varepsilon}$  the Taylor microscale,  $r_k$  the Kolmogorov length scale,  $T$  the large eddy turnover time,  $\tau_k$  the Kolmogorov time scale,  $\Delta t$  the fluid time step,  $k_{max}$  the maximum resolved wavenumber of the simulation.

where  $\mathbf{u}(\mathbf{x}, t)$  is the fluid velocity field,  $P(\mathbf{x}, t)$  is the fluid pressure field and  $\mathbf{F}(\mathbf{x}, t)$  is a fluid forcing that injects kinetic energy to maintain the flow. The equations are solved in a  $256^3$  grid using the standard pseudospectral technique (involving Fourier transform, for details see Brucker et al. 2007). Energy is continuously injected into the first two wavenumbers to maintain a turbulent flow that is statistically stationary, homogenous and isotropic (Witkowska et al., 1997). Table 6.1 lists the major parameters of the flow.

### 6.1.2 Simulating the particles

Particles of various Stokes numbers are introduced into the flow. Specifically we simulated particles with 250 different discrete Stokes numbers in the range  $St =$

0.01 to 1.2 with uniform increment of  $\delta St = 0.005$  (each Stokes number has 8000 particles). Hereafter we refer each simulated Stokes number as a Stokes number line (in short,  $St$ -line). This unique setup makes it possible to study effects of poly-dispersity and also gives us the flexibility of post-filtering the particle  $St$ -distribution to match any application specific shape, for instance when comparing results with real experiment where the particles are continuously poly-disperse (spanning a continuous range of Stokes numbers). It is important to note here that we are making the assumption that  $\delta St$  of 0.005 is small enough that a combination of adjacent lines provides a good first order model for the case of continuous poly-disperse particles<sup>‡</sup>.

Two simulations were performed, one with an initial particle distribution that is random and uniform over the simulation domain (case UI) while in the other, particles are initially concentrated in a cube (internally uniformly and randomly distributed) of dimensions  $1/4$  that of the full domain along each side (case CI). In both cases the background fluid velocity field is exactly the same at all times. Here we will mainly focus on the UI case (findings from the CI case will only be mentioned where needed). After the inertial clusters have achieve equilibrium with the flow, steady state RDF's were accumulated from particle positions starting from  $18T$  until  $60T$ . The choice of  $18T$  is a very conservative one since RDF's was apparently steady at significantly earlier times. Other authors had use as low as  $6T$  under similar conditions (see e.g. Collins and Keswani, 2004).

---

<sup>‡</sup>This assumption should be reasonable when the finite range of particle Stokes number considered is large compared to the this spacing, true for most cases in this thesis.

The particles are advected in the flow (under the action of Stokes drag) according to the equations:

$$\begin{aligned}\frac{d\mathbf{x}_i}{dt} &= \mathbf{v}_i \\ \frac{d\mathbf{v}_i}{dt} &= \frac{1}{\tau_p}[\mathbf{u}(\mathbf{x}_i) - \mathbf{v}_i]\end{aligned}\tag{6.2}$$

where  $\mathbf{x}_i$  and  $\mathbf{v}_i$  are the position and velocity of the  $i$ th particle, respectively, while  $\mathbf{u}(\mathbf{x}_i)$  is the undisturbed fluid velocity at the particle position,  $\mathbf{x}_i$ . These equations are a simplified version of the Maxey-Riley equations (Maxey and Riley, 1983) under the assumption of heavy ( $\rho_p/\rho_f \gg 1$ ) and small ( $d/r_k \ll 1$ ) particles<sup>§</sup>. Both of these assumptions are well satisfied in the context of this thesis (as for many aerosol containing flows) since  $\rho_p/\rho_f \sim 1000$  for water droplets in air, and  $d/r_k \sim 0.1$  for the range of droplet size used in the experiments<sup>¶</sup>. Also neglected is the influence of the particle volumes on the fluid continuity equation and reverse coupling effect of the particles on the flow owing to small volume loadings ( $\Phi_v \sim 10^{-5}$ ) and small mass loading ( $\Phi_m \sim 10^{-2}$ ) respectively (see e.g. Geiss et al., 2004).

Additionally, we neglect gravitational settling. The DNS work of Wang and

---

<sup>§</sup>Specifically, under these conditions, one may neglect the added mass, Basset history and Faxen corrections that would arise in the complete analysis of the forces acting on particles in time-dependent flows

<sup>¶</sup>Regarding the second condition, it is generally accepted that  $r_k$  under-estimates the smallest scales of fluid velocity gradient by a factor  $\sim 10$ , which makes this condition less stringent (see footnote of Eq. 5.2).

Maxey (1993) found no appreciable effect of gravity on the particle concentration statistics for  $S_g \equiv v_g/u_k < 3$ , where  $v_g = \tau_p g$  is the gravitational settling velocity and  $u_k$  is the Kolmogorov velocity scale. This is consistent with our own experimental finding in Chapter 5 (the definition of  $S_g$  here is equivalent to that used in earlier chapters). In our experiments,  $S_g$  ranges from  $\mathcal{O}(10^{-2})$  to  $\mathcal{O}(1)$ .

Further technical details include the use of two-stage second order Runge Kutta method (Heun’s method) in integrating Eq 6.2 to obtain particle tracks. Fluid velocities at particle centers are obtained via an eighth-order Lagrangian interpolation scheme similar to that described in Berrut and Trefethen (2004). The smallest particles were advanced multiple time steps within each fluid time step in order to account for their much smaller response times relative to  $\tau_k$ .

## 6.2 Results and Discussions

We begin by showing snapshots of particle fields from the DNS in Figure 6.1. Both panels correspond to the same instance in time and the same spatial sub-domain (a ‘thin slice’ of  $3 r_k$  thick and  $2\pi \times 2\pi$  across\*) with the right panel showing particles of higher Stokes number. Clearly, the particles appear clustered with clustering more pronounced at higher Stokes number.

---

\*The whole simulation domain has volume of  $(2\pi)^3$ .

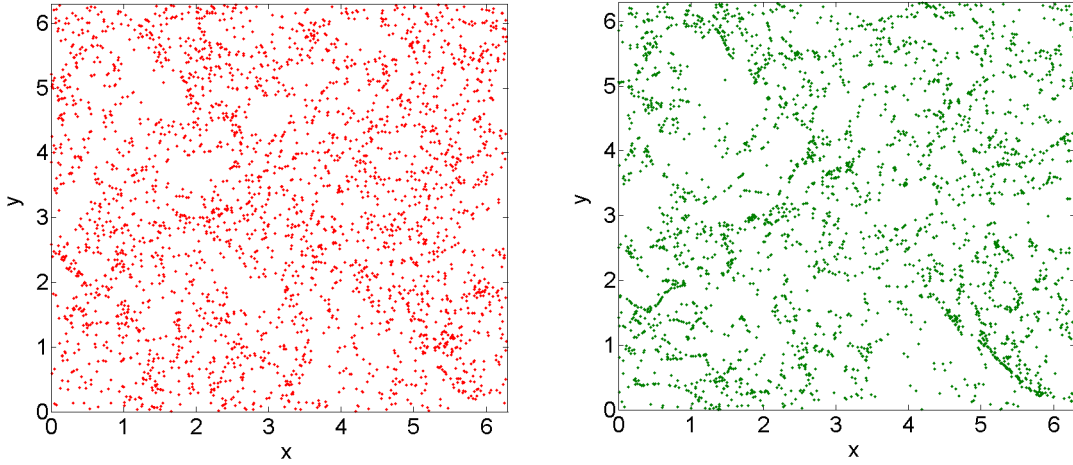


**Figure 6.1:** Snapshots of particle fields from the DNS taken at the same instance in (simulated) time and in the same spatial sub-domain (a ‘slice’ of  $3r_k$  thick and  $2\pi \times 2\pi$  across). Left, particles with  $St=0.1-0.4$ ; Right, particles with  $St=0.5-0.8$

Closer observation of the right panel reveals some geometrical structure of the clusters. Some of the clusters appear as thin lines which suggests that they are two dimensional sheets in three dimensional space. Further geometric analysis shall be the focus of future works. However, here we note that since we learnt from Eq. 1.10 that the clustering exponent ( $c_1$ ) is related to the fractal dimension of the particle field ( $\mathcal{D}_2$ ), sheet like clusters implies that  $c_1$  will have values approaching unity<sup>†</sup>. We shall see in Sec. 6.2.1 that this is indeed the case (cf. Fig. 6.3). Throughout our studies,  $c_1$  has never been found to have value larger than 0.8 (as we shall see) and it is interesting to question whether this tentative upper bound and the sheet like nature of clusters can be theoretically explained.

---

<sup>†</sup>This is because  $\mathcal{D}_2$  will have values close to 2, the value for perfect two dimensional object (see e.g. Strogatz, 2001).

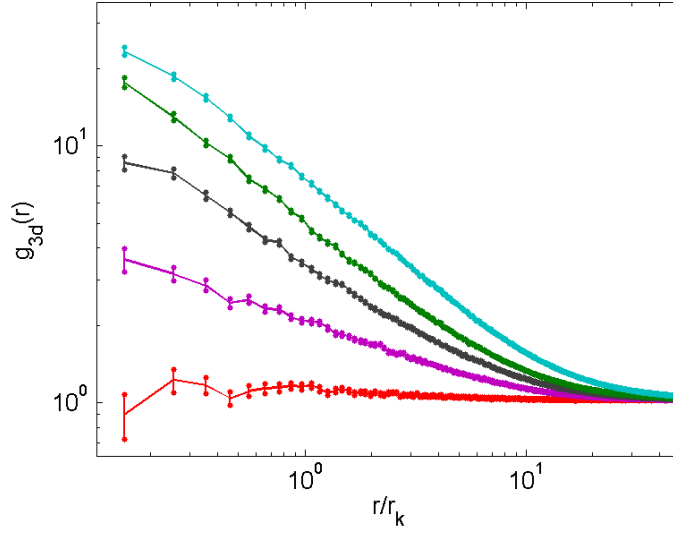


**Figure 6.2:** Quasi mono-disperse RDF calculated from 3D particle positions. Individual RDF represent Stokes number of (increasing from bottom top): 0.04, 0.2, 0.36, 0.52, 1.0.

### 6.2.1 Comparing DNS results with theory: mono-disperse

Figure 6.2 shows some of our DNS results (in terms of RDF) for ‘quasi’ mono-disperse  $g(r)$  calculated using three dimensional particle positions, for various Stokes numbers. Inertial clustering is found to occur for  $r/r_k \lesssim 20$  and increases with  $St$  but starts to show saturation at  $St \sim 1$ .

These results are ‘quasi’ mono-disperse in the sense that particles from more than one  $St$  lines were used in the calculation of each  $g(r)$  in order to have the curve smooth enough for meaningful studies. Specifically, for each  $St$  level studied we included particles of five  $St$ -lines centered on the  $St$  of interest, thus in effect we are considering particle with  $St \pm 0.01$  respectively. (Recall that line spacing is 0.005



and there are 8000 particle per line). Detailed study (see Sec. 6.2.2) convinced us that the effect of this level of  $St$  broadening is just a few percent reduction in power-law exponent (quantity of main interest) of the  $g(r)$  at the length scale that we can resolved here ( $r/r_k \geq 0.1$ ). This reduction is negligible compared with the level of statistical fluctuation in these results<sup>‡</sup>. We thus are confident that these results are relevant for mono-disperse studies to a very high degree although keeping in mind that they strictly represent lower bounds.

Next we compare the power-law exponents (cf. Eq. 1.7), written as  $c_1$ , of these RDF's with the theoretical prediction of Chun et al. (2005)<sup>§</sup>. This is shown in Fig. 6.3 where the solid parabolic curve is from the theory and the (blue) error-bars plot is from the DNS. The theory predicts that  $c_1$  scales as  $St^2$  for  $St \ll 1$  with a coefficient that depends on various turbulent flow statistics. Specifically they found (for  $St \ll 1$ ):

$$c_1 = 0.9 [\sigma_\varepsilon^2 T_{\varepsilon\varepsilon} - \rho_{\varepsilon\zeta} \sigma_\varepsilon \sigma_\zeta (T_{\varepsilon\zeta} + T_{\zeta\varepsilon}) + \sigma_\zeta^2 T_{\zeta\zeta}] St^2 \quad (6.3)$$

where  $\varepsilon(t)$  is the instantaneous kinetic energy dissipation rate,  $\zeta(t)$  is the instantaneous enstrophy (square of vorticity) times the kinematic viscosity,  $\sigma_X$  is the standard deviation of the variable  $X$  normalized by its mean  $\langle X \rangle$ ,  $\rho_{XY}$  is the cross-correlation coefficient and  $T_{XY}$  is the correlation time normalized by Kolmogorov time scale (see

---

<sup>‡</sup>For cases  $St < 0.3$ , we instead calculate  $g(r)$  separately for each  $St$  line and then average  $g(r)$  over five  $St$ -lines. In principle this should give more accurate result, yet we did not see any improvement at the current level of statistical accuracy

<sup>§</sup>Similar theoretical treatments were also published earlier by Falkovich et al. (2002); Zaichik and Alipchenkov (2003)

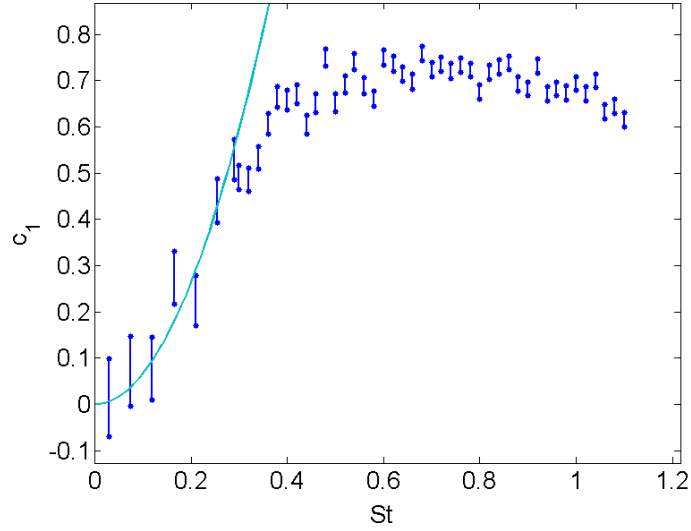


**Figure 6.3:** Clustering exponent ( $c_1$ ) versus Stokes number ( $St$ ). Blue, DNS; Cyan, theory.

Chun et al. for details). In the same work, using semi-empirical inputs from DNS performed at  $R_\lambda = 47.1$ , they obtained a value of 6.6 for the coefficient in front of this  $St^2$ -law.

The figure clearly shows good numerical agreement between the two results for  $St \leq 0.3$  even though it is not clear that our DNS results dictate a  $St^2$  scaling. In fact it is arguable that a linear scaling would be equally likely. We partially address this point by performing a linear fit (method: error accounting least-square fitting using model  $\hat{y} = m\hat{x} + y_o$ ) on the DNS data in the range  $St \leq 0.4$  and found that  $y_o = -0.09 \pm 0.04$ . Since a negative clustering exponent is un-physical for particles with zero Stokes number (fluid tracers) and also for inertial particle in the absent of repelling forces, we conclude that our result supports some kind of curvature for the

$c_1(St)$  curve at this limit (so that  $c_1$  does not cross over to the negative side and will instead cross the origin). However, we can not be certain that this curvature is of the  $St^2$  nature at this point. Similar conclusion can also deduced in Chun et al. (2005).

Theory for finite  $St$  is still open, however the peaking and subsequent decrement of  $c_1$ , starting around  $St = 0.5$ , is likely related to the general conviction that heavier particles, with inertial response time much larger than the coherence time scale of smallest (dissipative) eddies (typical  $\sim \tau_k$ ), do not respond well to the centrifugal effects of these eddies, thus resulting in weaker inertial clustering. Other works (see e.g. DNS results in Bec et al. (2007)) have shown that particles becomes un-clustered again at larger  $St$ .

One point worth addressing here is the fact that the theoretical results rely semi-empirically on a DNS that was done at  $R_\lambda = 47.1$ , lower than in our own simulation ( $R_\lambda = 143$ ). For one, the good numerical agreement suggests that inertial clustering may not be a strong function of Reynolds number. This matter will be addressed more closely in Sec. 6.2.5. On the other hand, if one considers Eq. 6.3, it is not obvious that the complicated coefficient should have only weak Reynolds dependence. Currently we do not have clear answer for this. It will be interesting to see if the coefficient so calculated from our own simulation really gives a value close to 6.6 (these statistics are not available to us for the moment).

Alternatively, Chun et al. also provide a more general form for  $c_1$  (still in the

limit of  $St \ll 1$ ):

$$c_1 = 3.61 St \tau_k^2 [\langle S^2 \rangle_p - \langle R^2 \rangle_p] \quad (6.4)$$

where  $S^2 \equiv S_{lj} S_{lj}$  and  $R^2 \equiv R_{lj} R_{lj}$  (summation over repeated indices implied) are the second invariant of the rate of strain and rate of rotation tensors, respectively<sup>¶</sup>.  $\langle \cdot \rangle_p$  implies averaging over ensemble of particles. Using this formulation and their DNS results for  $\langle S^2 \rangle_p$  and  $\langle R^2 \rangle_p$ , the resulting function  $c_1(St)$  is still a curve but the region of  $St^2$  scaling was limited to  $St \leq 0.05$ . At higher  $St$  this curve was found to be below the theoretical curve of  $6.6 St^2$ . The question of Reynolds dependence raised above is equally valid for this formulation. Our findings here (further strengthened in Sec. 6.2.5) imply that if the theory should be correct, these statistics should be weak functions of Reynolds number.

We conclude that there is a good agreement between theory and DNS at small Stokes number up to  $St \simeq 0.3$ . The disagreement at larger  $St$  is not surprising since these theories only address the limit of  $St \ll 1$ .

### 6.2.2 Effects of poly-dispersity on RDF

Figure 6.4 shows how the RDF changes from the case of (quasi) mono-disperse to poly-disperse. Essentially the slope (power-law exponent) diminishes with poly-dispersity

---

<sup>¶</sup>Further,  $S_{ij} \equiv \frac{1}{2}(\frac{\partial u_i}{\partial x_j} + \frac{\partial u_j}{\partial x_i})$ ,  $R_{ij} \equiv \frac{1}{2}(\frac{\partial u_i}{\partial x_j} - \frac{\partial u_j}{\partial x_i})$ .

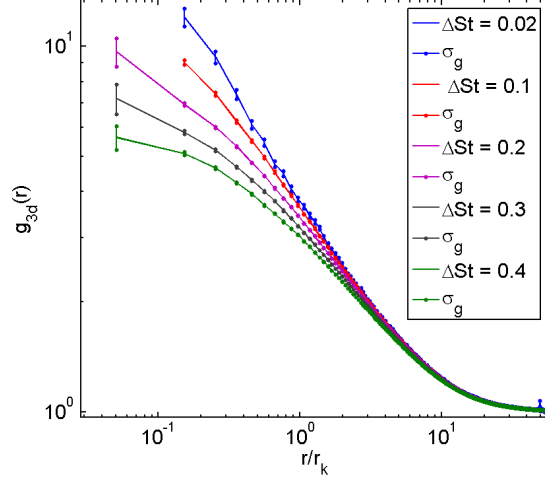


**Figure 6.4:** Poly-disperse RDF on logarithmic axes. Each  $g_{3d}(r)$  is based on particles with Stokes number within  $(St_{mid} \pm \Delta St)$  where  $St_{mid} = 0.4$ . Colors represent different  $St$ -bin widths,  $\Delta St$ , increasing from top to bottom. The observed trend is representative of results using other values of  $St_{mid}$ . The first point of the top two curves are thrown due to poor statistical convergence.

and a plateau region starts to appear at small  $r$  which grows with poly-dispersity. The power-law model for the RDF essentially breaks down when there is significant poly-dispersity. The appearance of the plateau at small scales signifies that one will not see clustering at these scales. Specifically if one were to zoom in on the particle field and look at a box of size corresponding to these scales, the particles should seemed random-uniformly distributed. In probabilistic language, the probability of finding neighbors (around a particle) at any distance shorter than the scale of onset of this plateau is the same (yet it is still higher than at any longer distances).

A physical interpretation for this is that, on average, particles of different  $St$  tend to cluster at slightly offset locations giving rise to a collective field of clusters that

is fuzzy. This is hardly surprising and reflects the simple fact that particle trajectories are deterministic function of their inertia. Mathematically the poly-disperse RDF can be constructed from the mono and bi-disperse RDF via a double integral:

$$g(r, a \leq St \leq b) = \int_a^b \int_a^b g_{12}(r, St_1, St_2) \rho(St_1) \rho(St_2) dSt_1 dSt_2 \quad (6.5)$$

where  $g_{12}(r)$  is the bi-disperse RDF (which becomes the mono-disperse RDF when  $St_1 = St_2$ );  $\rho(St)$  are the relative populations of each  $St$ . It is thus necessary and sufficient to understand the mono and bi-disperse RDF in order to make quantitative prediction on the RDF in any circumstances. Understanding the poly-disperse case is important because poly-dispersity is ubiquitous in nature.

In many situations, one may wish to know how much poly-dispersity can one have but still be able to describe the problem at hand as a mono-disperse problem (e.g. as we did in Sec. 6.2.1). Figure 6.5 answers this by showing the evolution of the clustering exponent,  $c_1$  with increasing poly-dispersity. We have investigated this in the range of  $St$  simulated and found (as seen in this plot) that the Stokes number width at which  $c_1$  is diminished by 10%,  $\Delta St_{10\%}$ , is roughly  $St_{mid}/5$  in the range of Stokes number studied.

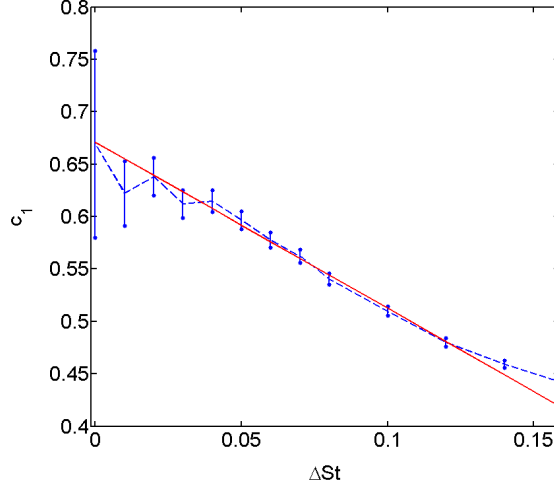


**Figure 6.5:** Power-law exponent,  $c_1$ , as a function of  $\Delta St$  for  $St_{mid} = 0.4$ . Red line is a linear fit on points satisfying  $\Delta St \leq 0.08$ . Trend representative of results using other values of  $St_{mid}$ .

### 6.2.3 Comparing Experimental and DNS results: poly-disperse

Here we present a comparison between empirical and DNS results. The experimental data presented are from the 5m20Hz run (cf. Table 5.1) with  $R_\lambda = 440$ . This is higher than the DNS  $R_\lambda$  of 143. This issue of comparing data at different  $R_\lambda$  will be fully discussed in Sec. 6.2.5, here we will simply state that an earlier study (Collins and Keswani, 2004) suggests that clustering is only weakly dependent on Reynolds at high enough  $R_\lambda$  such as considered here. Moreover, if  $R_\lambda$  should be an important factor, the compared data would reveal this to us.

Figure 6.6 shows some of the experimental and DNS results on the same logarithmic axes. The error-bar plots are the experimental RDF's calculated from one-dimensional inter-particle distances involving (continuous) poly-disperse particles.

Recall that we can not avoid considering particles with finite Stokes number ranges in order to have acceptable statistical convergence of the RDF. The other lines are from DNS which will be described shortly. Three sets of particles are shown here as different colors, starting from bottom in blue are particle with  $St = 0.01 \rightarrow 0.21$ ; green,  $St = 0.09 \rightarrow 0.29$ ; red,  $St = 0.25 \rightarrow 0.45$ . The plots in the figure are vertically shifted so that their plateau regions at large  $r$  ( $30 \lesssim r/r_k \lesssim 60$ ) roughly coincide. We are thus restricted to comparison of trends or slopes (the clustering exponent) between these curves and the DNS results. The reason for such vertical shifting (also mentioned in Sec. 5.3) is to remove the signature of large scale inhomogeneity in particle density from the RDF. Such inhomogeneity is very likely due to the incomplete mixing of cloudy and dry air in the wind tunnel as detailed in Sec. 3.3.2\*.

The DNS results are shown in three different sets for each Stokes number range. This is to discern the relative contribution of each correction made in the process of bringing the DNS to an equal footing with the experiments. We start with the dotted lines which are RDF's calculated with three-dimensional positions ( $g_{3d}(r)$ ) of particles matching the experimental  $St$ -ranges but with flat  $St$ -distribution inside each  $St$  bin. Clearly, these lines are significantly steeper than their measured counterparts. (We choose not to plot the mono-disperse counter part for comparison but in light of Sec. 6.2.2, these results would be more steep than the dotted lines and thus, deviate

---

\*The same section also concludes (theoretically) that when there is a large scale separation between the large scale inhomogeneity and the inertial clustering, the effect of large scale inhomogeneity on the RDF signature of inertial clustering is just a multiplicative constant (at least in the first order). Our experimental finding also supports this conclusion, see Sec. 5.4 for detailed account.



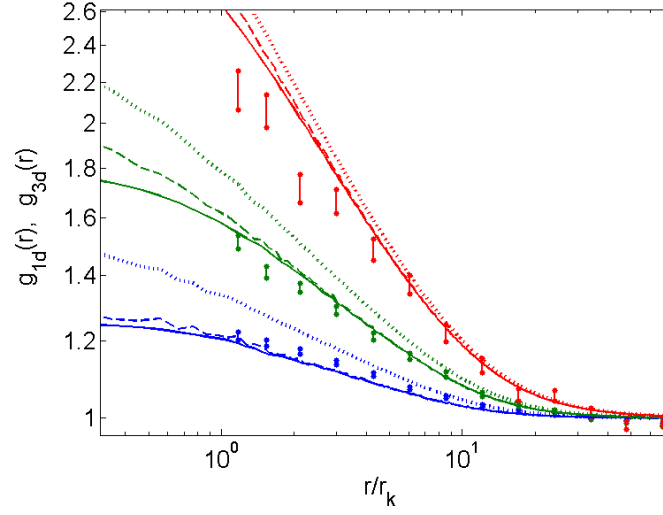


**Figure 6.6:** Poly-disperse RDF on logarithmic axes. Colors represent different  $St$  ranges.  $St$  increases from bottom to top: blue is  $St = 0.01 \rightarrow 0.21$ ; green,  $St = 0.09 \rightarrow 0.29$ ; red,  $St = 0.25 \rightarrow 0.45$ . The error-bar plots are experimental results [ $g_{1d}(r)$ ]; dotted lines,  $g_{3d}(r)$  with flat  $St$ -bins; dashed lines,  $g_{3d}(r)$  with corrected (matching experiment's)  $St$ -bins; solid lines,  $g_{1d}(r)$  with corrected  $St$ -bins. The experimental plots are vertically shifted so that only their trends or slopes are compared (see text).

much more from the measurements.) This suggests the importance of matching the shape of the particle  $St$  distribution when comparing results. The experimental  $St$ -distribution of each  $St$  bin is far from flat (Fig. 6.7), and therefore it is necessary to account for the actual distribution of  $St$  within the bins.

Back to Fig. 6.6. The dashed lines are the further corrected  $g_{3d}(r)$  using poly-disperse particles matching the experimental  $St$  distribution. The agreement with the experimental curves is much improved. Finally, we also applied spatial averaging to these  $g_{3d}(r)$  to obtain the one-dimensional counterparts,  $g_{1d}(r)$ , plotted as solid curves in the figure. This is done following the mathematical analysis of Holtzer and Collins

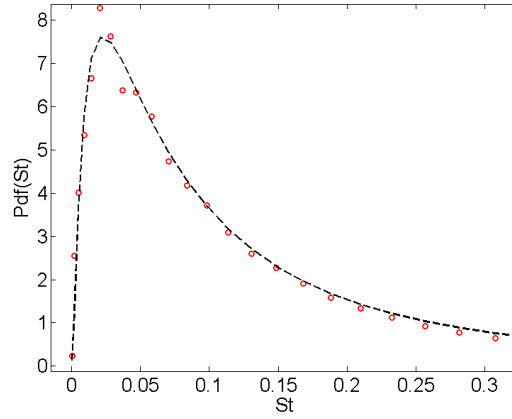


**Figure 6.7:** Probability distribution function of droplet Stokes number for experiment 5m20Hz whose result is discussed in this section. Black line is a log-normal fit.

(2002) using a realistic estimate of the dimensions of our phase-Doppler device’s measurement volume which is roughly  $r_k \times r_k$ . (In many instances, we also took the alternative path of down-sampling the particle position into one-dimension, followed by direct calculation of  $g_{1d}(r)$  and found very good agreement.) One can see that the main differences between  $g_{3d}(r)$  and  $g_{1d}(r)$  are restricted to regions of  $r$  less than the measurement volume size ( $\sim r_k$  in this case), where  $g_{1d}$ ’s are considerably flattened as a result of dimensional averaging (consistent with the findings of Holtzer and Collins). At the length scales that our experiments can resolve, this effect is almost negligible even though it does shift the RDF’s in the direction of better agreement between experiment and DNS.

Let us now focus on the final comparison between DNS and experiment ( $St$ -bin matched  $g_{1d}(r)$ ), plotted in logarithmic axes in Figure 6.8. The most striking

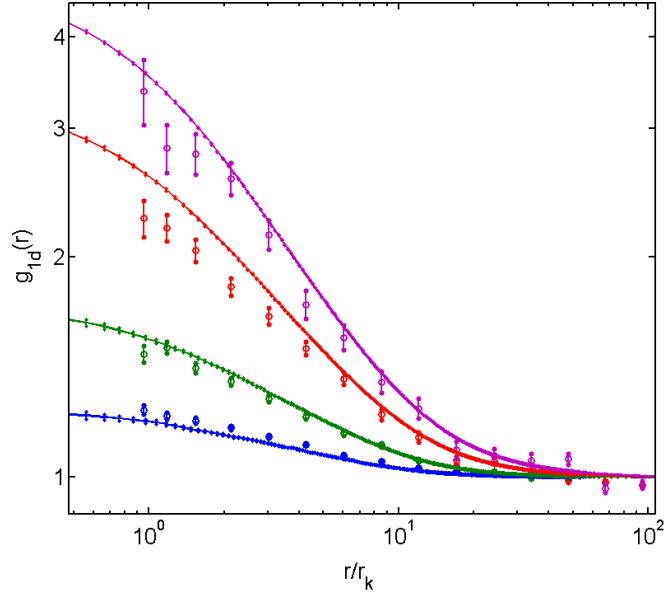


**Figure 6.8:** Poly-disperse RDF on logarithmic axes. Colors represent different  $St$  ranges.  $St$  increases from bottom to top: blue is  $St = 0.01 \rightarrow 0.21$ ; green,  $St = 0.09 \rightarrow 0.29$ ; red,  $St = 0.25 \rightarrow 0.55$ ; purple,  $St = 0.40 \rightarrow 1.0$ . Open circles with error-bars are experimental results  $[g_{1d}(r)]$ ; Solid lines with error-bars are  $g_{1d}(r)$  from DNS (matching experimental  $St$ -bins). The experimental plots are vertically shifted so that only their trends or slopes are of absolute significance.

agreement between the two is that inertial clustering becomes pronounced at small length scales, below  $r/r_k \sim 10$  to  $30$ , and apparently increasing with particle inertia ( $St$ ). A Similar trend was also found for mono-disperse cases (Fig. 6.2). That inertial clustering starts at  $\sim 10r_k$  is consistent with the idea that it is a dissipative scale phenomenon since there are many evidence that  $r_k$  under-estimates the scale of strongest velocity gradients in turbulence (the essence of energy dissipation) by a factor of  $\sim 10$  [see Monin and Yaglom (1975, Sec. 23.4 and Fig. 77) ; and Saddoughi and Veeravalli (1994, Sec. 3.2.1 and Fig. 10)]. Both data also agree on the qualitative trend of increasing clustering (e.g. the steepness of  $g_{1d}$ ) with particle Stokes number in the

range of  $St \leq 1$ . We can not at this time make clear conclusion about larger  $St$  due to limited statistical convergence and other problems in the experiments.

Quantitative agreement between the experiment and DNS, again in terms of the average steepness of RDF, is also very good at the experimentally resolvable scales. This is especially true at the small  $St$  limit. However, it may be apparent that the experimental curves tend to lie below the DNS at higher  $St$ , especially in the case of red curves. Note that the experimental error-bars only capture statistical (sampling) errors, thus this implies there is systematic deviation, albeit small, between the two at larger Stokes.

The explanation for this deviation is still unknown. Some speculations includes the sizing error of the PDI instrument, over-estimation of kinetic energy dissipation rate and the effect of gravity not simulated in DNS. However we choose not dwell on it here since it is a small deviation considering the state of knowledge of turbulent phenomenology. To begin, the concept of Stokes number is not a sharply defined quantity. Here it is defined as  $\tau_p/\tau_k$ , where  $\tau_k$  is understood as representing coherence time scale of dissipative (smallest) scale of turbulence, a quantity that may not have a sharply defined value. Further,  $\tau_k$  is always taken as  $(\nu^3/\bar{\varepsilon})^{1/4}$  via dimensional analysis, which could easily be subjected to a dimensionless factor of order unity. Lastly  $\varepsilon$  is a strongly fluctuating quantity in turbulence whose mean value may not capture fully the physics in the problem (this intermittency is known to increase with

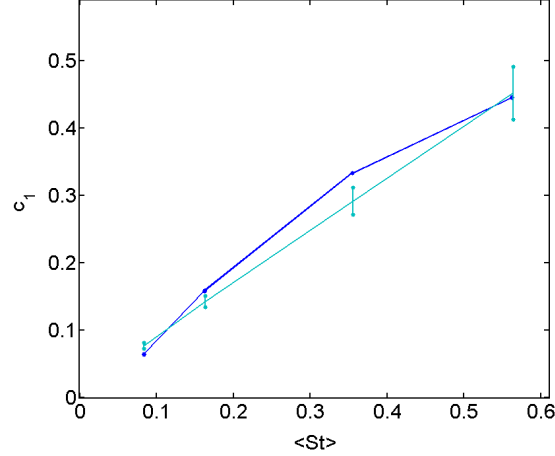


**Figure 6.9:** The average steepness of the (poly-disperse) RDF's in Fig. 6.8,  $c_1$  as function of average Stokes number,  $\langle St \rangle$ . Blue is the DNS results; cyan, empirical.  $c_1$  is obtained by fitting power-law (straight line in logarithmic axes) to RDF in the window of  $r/r_k = 2 \rightarrow 10$ , using the same fitting algorithm used for in Fig. 6.3.

Reynolds number). In view of this, we found that if we increase the experimental value of  $\tau_k$  by about 9% (equivalent to reducing  $\varepsilon$  by 30%) then the agreement between the two results would be nearly perfect.

Although the experimental RDF's do not have a clear power-law like region as the mono-disperse case, in order to illustrate the trend of the steepness of RDF with respect to  $St$ , we did a power-law fit on these RDF in the window:  $r/r_k = 2 \rightarrow 10$  where the slope are fairly constant. The results are shown in Figure 6.9.

We thus conclude that there is good agreement between experiment and DNS despite some small unresolved deviations. Together with the good agreement found in Sec. 6.2.1 between theory and DNS data (from exactly the same run used here),

we have shown, indirectly, that there is some level of consistency between theory and experiment. Specifically, if we assume that the agreement between DNS and experiment found here can be extrapolated to the limit of  $\Delta St \rightarrow 0$  (mono-disperse), then we can claim that there is a good agreement between experiment and theory for inertial clustering of mono-disperse particles.

Further, in light of Eq. 6.5, if we can also show that the DNS and theory agree in the case of bi-disperse RDF, then by the same token, we may conclude that the theoretical prediction for poly-disperse RDF (using Eq. 6.5) is indirectly consistent with the experimental results. However, we will show that this is not the case, when we compare DNS and theory in the bi-disperse setting in Sec. 6.2.6.

#### 6.2.4 Relationship between $c_1$ and $c_0$

That the RDF's in all cases (regardless of dispersity and dimensionality) become horizontal at larger  $r$ , with onset within a narrow region of  $r/r_k \sim 10 \rightarrow 30$ , has an interesting and perhaps important consequence. It implies a close numerical relation between the pre-factor ( $c_0$ ) and the power-law exponent ( $c_1$ ) in the power-law model of the RDF (cf. Eq. 1.7).

To illustrate, we first need to generalize  $c_1$  to refer, in cases where a clean power-

law that extends to  $r \rightarrow 0$  is not observed<sup>†</sup>, to the slope of the RDF near the inflection point (e.g. the region of  $r/r_k = \mathcal{O}(1)$  in Fig. 6.8), where the curve is quasi-straight. Then, given any  $c_1$ , our empirical findings imply that the value of  $c_0$  is constrained such that the power-law, being a straight line in logarithmic axes, crosses the line of ( $y = 1$ ) at  $r/r_k \simeq 10 \rightarrow 30$ . This gives us a fuzzy relation of:

$$\frac{\ln c_0}{c_1} \simeq \ln 10 \sim \ln 30 = 2.3 \sim 3.4, \quad (6.6)$$

or alternatively:

$$c_0^{1/c_1} \simeq 10 \sim 30. \quad (6.7)$$

Since  $c_1$  was also found empirically to have upper-bound of  $\sim 0.8$  (cf. Fig. 6.3, Fig. 6.12 and Sec. 6.2.3), this allows us to estimate  $c_0$  from  $c_1$  within a factor of three. We have tested this on the DNS results (by obtaining  $c_0$  and  $c_1$  via power-law fitting as describe in the previous sections) and found that in almost all cases  $c_0^{1/c_1}$  falls within 7 to 30.

Further improvement can be made with the observation that  $c_0^{1/c_1}$  increases gradually with  $St$  within that range of 10 to 30. This observation might have a physical explanation along the line of clustering of large particles ( $St > 1$ ) in the inertial subrange of turbulence.

---

<sup>†</sup>e.g. when  $St$  is large, poly-disperse, etc.

Apart from practical implication of this relation, the important lesson we learn from this is that  $c_0$  and  $c_1$  are not independent quantities. They are linked through the fact that inertial clustering must cease at order of ten times Kolmogorov length, which has been consistently found to be the scales where velocity gradient is maximum [see Monin and Yaglom (1975, Sec. 23.4 and Fig. 77) ; Saddoughi and Veeravalli (1994, Sec. 3.2.1 and Fig. 10.)].

If we substitute  $c_0^{1/c_1} = r_s/r_k$ , where  $r_s$  is the starting scale of inertial clustering, into the power-law model  $c_0(r_k/r)^{c_1}$ , we get:

$$g(r) = \left(\frac{r_s}{r}\right)^{c_1} \quad (6.8)$$

a power-law with a single parameter,  $c_1$ , only if  $r_s$  is sharply defined and universal. However, our results suggest that  $r_s$  is weakly dependent on  $St$ .

### 6.2.5 Asymptotic behavior at large Reynolds number

There have been questions about the behavior of inertial clustering with the increase of Reynolds number. Recently Collins and Keswani (2004) showed DNS results (of mono-disperse particles) at various Reynolds numbers up to  $R_\lambda = 152$  and concluded that both the clustering exponent,  $c_1$ , and the pre-factor,  $c_o$ , approach saturated values as  $R_\lambda$  increases. On the other hand Falkovich and Pumir (2004), in exact



disagreement, present DNS results showing linear (or faster) increase of  $c_1$  (called  $\alpha$  in their paper) with  $R_\lambda$  in the same range (up to  $R_\lambda = 130$ ). This was interpreted as a consequence of increased intermittency in turbulent velocity gradient as Reynolds number increases.

Our results (experimental and from DNS) strongly support saturation of  $c_1$  in the limit of large Reynolds number. In Sec. 5.3 (specifically Fig. 5.2), our results from different sets of experiments covering  $R_\lambda$  from 440 to 660<sup>‡</sup> showed strong Stokes similarity in the steepness of the RDF (equivalent to  $c_1$ ). This implies that any Reynolds dependence of  $c_1$  is within the error-bars and thus much weaker than the dependence on Stokes. Besides this, the good agreement between experiments ( $R_\lambda = 440$ ) and DNS ( $R_\lambda \sim 140$ ) found in Sec. 6.2.3 clearly supports this conclusion<sup>§</sup>.

Further, since  $c_0$  is intimately linked to  $c_1$  (in light of Sec. 6.2.4), our results imply that  $c_0$  is also saturated at high Reynolds.

## 6.2.6 Comparing DNS with theory: bi-disperse RDF

Figure 6.10 shows the general behavior of the quasi<sup>¶</sup> bi-disperse RDF. Each RDF reflects the spatial correlation between two sets of particles with different Stokes

---

<sup>‡</sup>We actually have data up to  $R_\lambda \sim 800$  showing consistent trend.

<sup>§</sup>In fact, the experimental RDF was slightly lower than the DNS at larger  $St$ .

<sup>¶</sup>See discussion in Sec. 6.2.1 for details

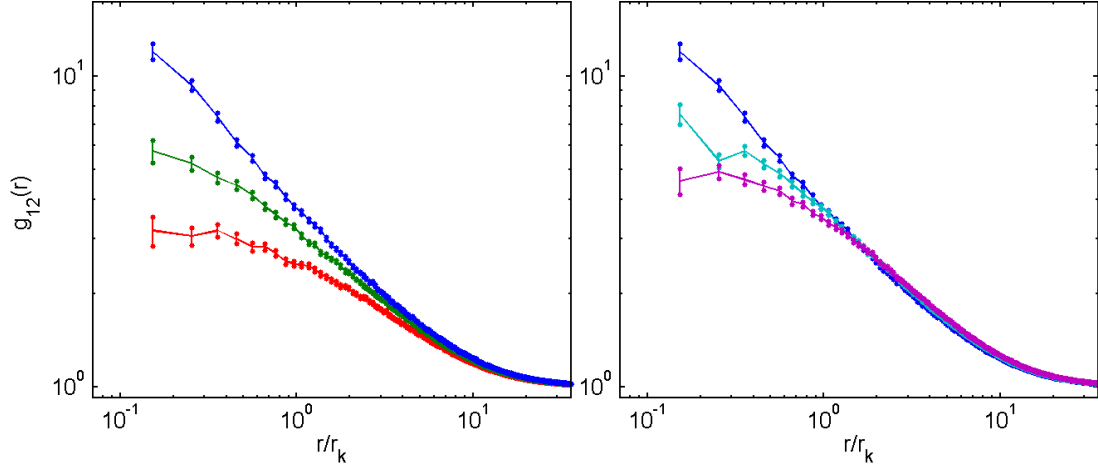


**Figure 6.10:** Bi-disperse RDF from DNS, with one Stokes number fixed,  $St_1 = 0.40$ , while the other,  $St_2$ , varied. **Left)** Blue,  $St_2 = 0.40$  (mono-disperse); green,  $St_2 = 0.34$ ; red,  $St_2 = 0.28$ . **Right)** Blue,  $St_2 = 0.40$  (mono-disperse); cyan,  $St_2 = 0.46$ ; purple,  $St_2 = 0.52$ . General trend representative of cases at other Stokes numbers studied.

numbers,  $St_1$  and  $St_2$ . Here the value of  $St_1$  is fixed while  $St_2$  is varied for each RDF in order to show the effect of bi-dispersity. (RDF's are invariant with respect to exchange of  $St_1$  with  $St_2$  as anticipated). The general trend is similar to those found with respect to poly-dispersity in Sec. 6.2.2. This is of course not surprising since the two cases are intimately connected through Eq. 6.5. However, as can be seen in the plots, the behavior of  $g_{12}$  is asymmetric when one Stokes number ( $St_1$ ) is fixed while the other ( $St_2$ ) is varied away from it. When  $St_2$  is lowered with respect to  $St_1$ , the slope of  $g_{12}$  (at the inflection point) diminishes and a plateau starts to appear. On the hand when  $St_2$  is increased from  $St_1$ , the slope of  $g_{12}$  remain nearly constant. The magnitude of  $g_{12}$  at  $r$  above the scale corresponding to the the inflection point, becomes slightly larger than the mono-disperse case. We will come back to this point later.

Chun et al. (2005) proposed a model for  $g_{12}$  of the form:

$$g_{12}(r) = c_0 \left( \frac{r_k^2 + r_c^2}{r^2 + r_c^2} \right)^{c_1/2}, \quad (6.9)$$

where  $r_c$  is the scale below which flattening of  $g_{12}$  occurs;  $c_0$  and  $c_1$  has the same interpretation as in the mono-disperse case. Note that this reduces to the mono-disperse RDF (Eq. 1.7) when  $r_c = 0$ , thus it is a generalization that encompasses both cases. The Chun et al. theory also predicts (in the limit of  $St \ll 1$ ), with semi-empirical input from DNS (at  $R_\lambda = 47$ ), that:

$$r_c \simeq 5.0 |St_2 - St_1| \quad (6.10)$$

and

$$c_1(St_1, St_2) \simeq 6.6 St_1 St_2. \quad (6.11)$$

We will now compare our DNS results with these predictions with DNS values for  $r_c$  and  $c_1$  obtained by fitting Eq. 6.9 to the RDF's (all the fits are very good by inspection).

Figure 6.11 shows a comparison of theory (Eq. 6.10) and DNS for the trend of the flattening scale,  $r_c$ . The agreement is surprisingly good especially at higher Stokes numbers (e.g.  $St \geq 0.4$ ), considering that the theory was developed in the limit of  $St \ll 1$ . It is clear that  $r_c$  behaves symmetrically with respect to the point

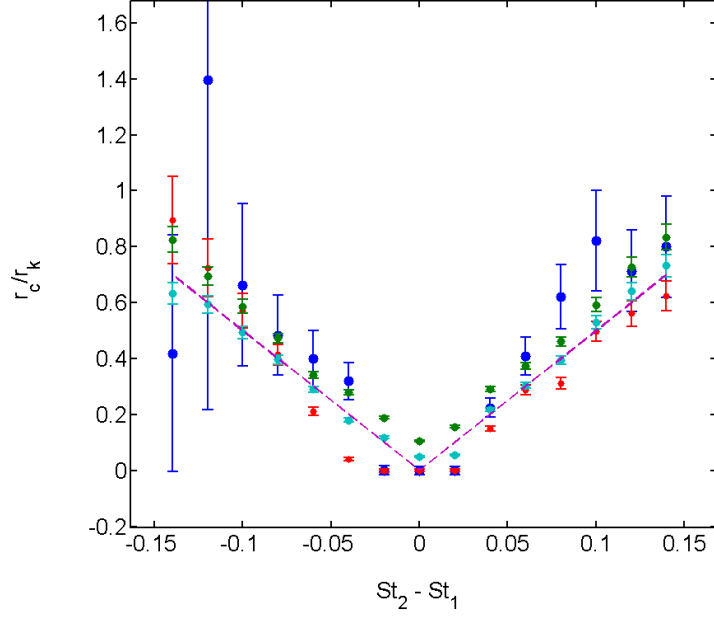


**Figure 6.11:** The normalized flattening scale  $r_c/r_k$  versus  $St_2 - St_1$ . For each color,  $St_1$  is fixed while  $St_2$  is varied. Blue,  $St_1 = 0.2$ ; red,  $St_1 = 0.4$ ; cyan,  $St_1 = 0.7$ ; green,  $St_1 = 1.0$ . Magenta dashed line is the theoretical prediction ( $5.0 |St_2 - St_1|$ ). All  $r_c$ 's were obtained by fitting Eq. 6.9 to  $g_{12}(r)$  in the window  $r/r_k = 0.1 \rightarrow 4$ .

of  $St_2 - St_1 = 0$  (hereafter we define  $\Delta St_{21} \equiv St_2 - St_1$ ). This implies that  $r_c$  only depends on the absolute value of  $\Delta St_{21}$ .

Figure 6.12 shows the comparison of theory and DNS for the exponent  $c_1$ . It is clear that even at Stokes number as small as  $St_1 = 0.2$ , the theory fails to account for the asymmetric nature of  $c_1$  with respect to sign of  $\Delta St_{21}$  (with  $St_1$  fixed). For instance in the  $St_1 = 0.2$  case, when  $\Delta St_{21}$  is negative ( $St_2 < St_1$ )  $c_1$  is linear with  $St_2$  but when  $St_2 > St_1$ ,  $c_1$  becomes almost constant. This can be understood as a bottle-neck effect where  $c_1$  is always strongly limited by one of the Stokes numbers which corresponds to less clustered particles (note that this is not always the smaller

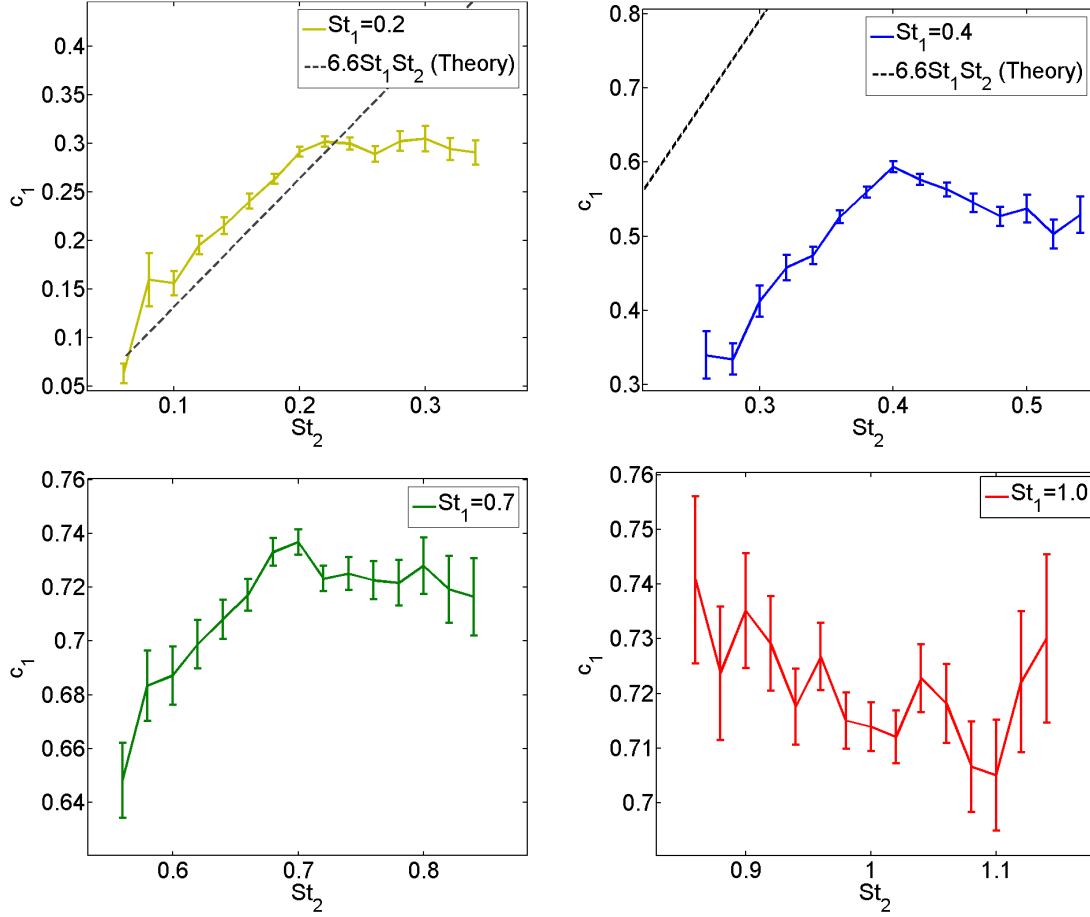


**Figure 6.12:**  $c_1$  versus  $St_2$  with  $St_1$  fixed at various values. Theoretical prediction of linear dependence of  $c_1$  on  $St_2$  is not correct (see text).

$St$ ). Starting with any mono-disperse case ( $\Delta St_{21} = 0$ ), changing only one of the two  $St$  in the direction of increased clustering does not introduce a significant increase in  $c_1$ .

Taking everything together, the bi-disperse trends of  $g_{12}$  can be interpreted as follows. Particles of different  $St$  cluster with sharpness characteristic of their  $St$ . The ‘clustering sites’ of different Stokes numbered particles are still in the vicinity of each

other (e.g. in the regions of high low vorticity) however they are slightly offset.  $r_c$  reflects an isotropic average of these offsets. These offsets presumably have isotropic statistics over the particle field, at least when there is no effect of gravity or other non-isotropic factors. The bottleneck behavior of  $c_1$  can be deduced from the relative cluster-sharpness of different  $St$  given the mathematical nature of RDF.

We conclude that the bi-disperse theory captures the behavior of the clustering offset,  $r_c$ . However, the theory does not predict the behavior of  $c_1$  correctly. To make a better prediction that reflects the observed bottleneck effect,  $c_1$  can be approximated (to the lowest order) by the smaller of the two mono-disperse  $c_1$ , each corresponding to one of  $St_1$  and  $St_2$ :

$$c_{1,bi}(St_1, St_2) = \min [c_1(St_1), c_1(St_2)], \quad (6.12)$$

where  $c_1(St_i)$  refer to the power-law exponents of the RDF of mono-disperse particles with the corresponding Stokes number. Based on observations in Fig. 6.12, this empirical model is accurate to within twice the error-bars for Stokes number in the range of 0 to 1.2.

With the failure of accurately predicting  $c_1$ , the Chun et al. theory is not expected to accurately predict the poly-disperse RDF (cf. Eq. 6.5).

### 6.2.7 Comparing Experiment with DNS: bi-poly-disperse RDF

Figure 6.13 shows the comparison of various  $g_{1d}(r)$  obtained from DNS and experiment (run 5m20Hz). Each curve measures the spatial correlation between two sets of particles with different ranges of  $St$ . Here we keep  $St_1$  fixed at 0.2 to 0.3 while  $St_2$  is varied (corresponding to different colors). The simple poly-disperse case ( $St_1 \equiv St_2$ ) is shown as purple colored lines. From the DNS (top-left plot), the general trend with respect to  $St_2$  is similar to the bi-disperse case (Fig. 6.10) described in Sec. 6.2.6 and will not be repeated here. The experimental RDF's (top-right) show a similar trend albeit the trend at larger  $St_2$  is hardly discernable due to statistical noise (lack of statistical convergence). The quantitative agreement for the slopes of these RDF's between DNS and experiment is very good when  $St_2$  is small, as seen in the top-left panel. At larger  $St_2$ , the two results remain close but the experimental curves seem to be consistently less steep. Here again, due to statistical noise, there is no clear evidence of RDF flattening at small  $r$  in the empirical curves.

We conclude here that good agreement between experiment and DNS albeit some ambiguities from statistical noise. Further, the experimental results clearly support the asymmetric dependence of the RDF slopes,  $c_1$ , on  $St_2$  when  $St_1$  is fixed (the bottleneck effect discussed in Sec. 6.2.6). A corollary of this coupled with the conclusion of Sec. 6.2.6, is that the theory and experiment disagree on the trend of  $c_1$ .

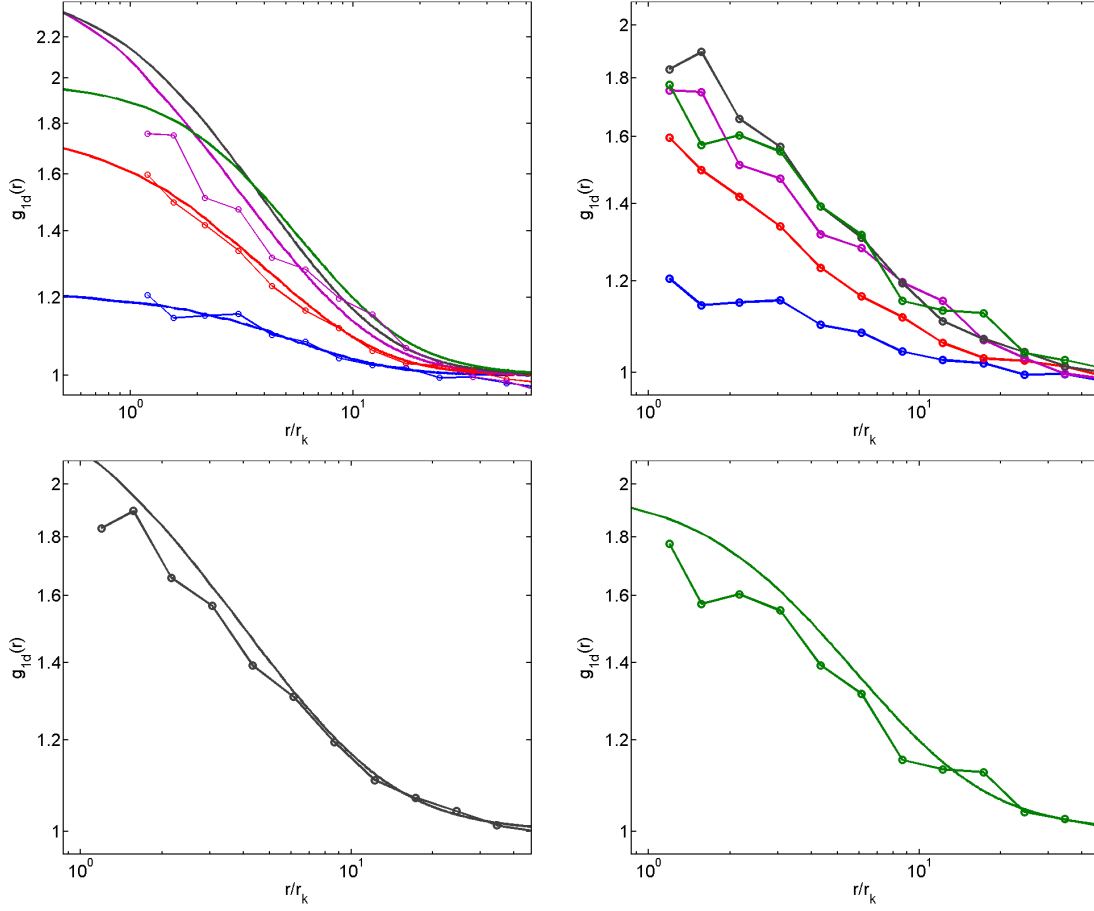


**Figure 6.13:** Bi-polydisperse RDF with  $St_1 = 0.2 \rightarrow 0.3$  (fixed).  $St_2$  is varied: blue is  $St_2 = 0.01 \rightarrow 0.1$ ; red,  $St_2 = 0.1 \rightarrow 0.2$ ; purple,  $St_2 = 0.2 \rightarrow 0.3$  (mono-disperse); black,  $St_2 = 0.3 \rightarrow 0.5$ ; green,  $St_2 = 0.5 \rightarrow 1.2$ . Smooth solid lines are from DNS; circles are from experiments (5m20Hz). Statistical error of experimental points are very well represented by the apparent fluctuation in each curve (which become larger at small  $r$ ). Top-left and bottom panels show comparison between DNS and experiment (separated for clarity); top-right panel shows only the experimental results.



## 6.3 Further discussions

### 6.3.1 Consistency of data between Cornell-1 and Cornell-2.

It is worth pointing out that the experimental data used throughout this chapter (with flow condition 5m20Hz) was collected much later in time compared to those used in Chap. 5. The two experimental campaign were called Cornell-1 and Cornell-2 respectively following their chronological sequence\*. Although most of the experimental setup are kept the same, there were two potentially significant changes. Firstly, the PDI instrument used in Cornell-2 experiments were of a newer and much improved version, this is the one that we described and characterized in Chap. 2. The older probe (which was a loaned system) is no longer accessible to us for detailed characterization.

Secondly, the spray pressure setting was changed in the Cornell-2 experiment in order to have droplets of smaller sizes (cf. Fig. 4.3). However we are fully confident that this does not have a significant consequence on the experiment since the impact of the sprays on the turbulence is negligible (Sec. 4.2.3) and because droplets have enough time to equilibrate with the small scale dynamics (Sec. 4.2.3).

Here we show a representative comparison of the results from both experimental

---

\*Cornell-1 was done in Dec. 2004 while Cornell-2 was done in June 2006.

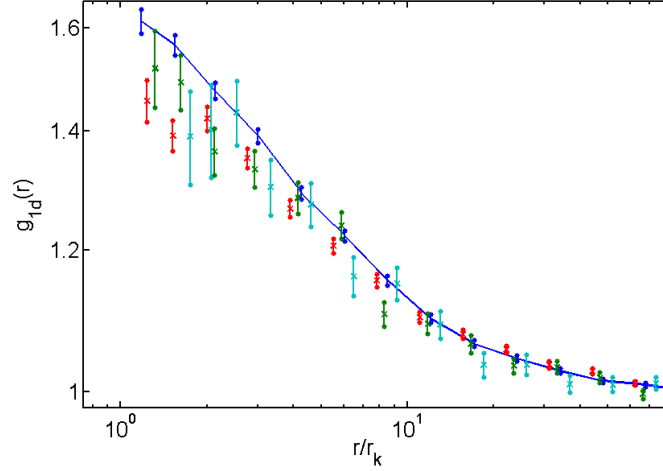


**Figure 6.14:** Comparing RDF from Cornell-1 and Cornell-2 experiments. All RDF are for  $St = 0.1 \rightarrow 0.5$ . Blue solid line is from Cornell-2, 5m20Hz run. The others are from Cornell-1: red is 3m20Hz; cyan, 3m40Hz; green, 5m30Hz. All plots are vertically shifted to match at  $r/r_k = 80 \sim 120$ . Note that Cornell 1 and 2 has different drop Stokes distribution (see Fig. 6.15).

periods (Cornell-1 and 2) in Figure 6.14. Shown were  $g_{1d}$  from various experimental run for particles with  $St = 0.1$  to  $0.5$ . The Cornell-1 RDF's (the  $\times$ 's) are found to be consistently slightly less steep than that the Cornell-2 RDF's (solid blue). Although the extents of the error-bars (due sampling noise) would challenge such a conclusion, comparison between the blue and the red plot certainly favors it.

This inconsistency between Cornell-1, 3m20Hz and Cornell-2, 5m20Hz is more pronounced when one takes into account the different Stokes distribution of these two experiments, shown in Figure 6.15. Here we see that the droplet Stokes distribution of the 3m20Hz data-set is flatter and thus contains more large drops than that of the Cornell-2 data-set. We thus expect that the 3m20Hz RDF should be steeper than the Cornell-2 RDF (cf. Sec. 6.2.2). Thus the resultant RDF of the 3m20Hz data being

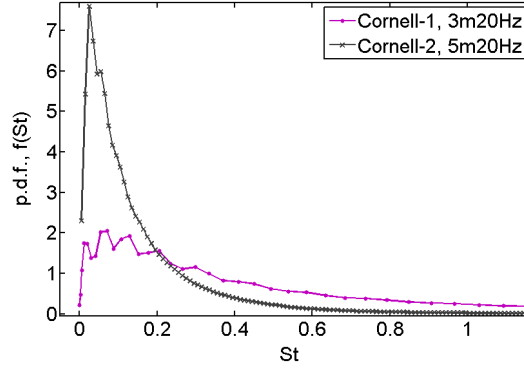


**Figure 6.15:** Comparing Stokes number distribution of droplets from Cornell-1, 3m20Hz with that from Cornell-2, 5m20Hz. Alternatively, for size distributions see Fig. 4.3.

systematically below the Cornell-2 RDF implies that the two sets of data are not exactly consistent in term of the Stokes dependence of RDF.

Apart from that, we see again (in Fig. 6.14) that all RDF from Cornell-1 (arguably even Cornell-2) collapse well within their error-bars signifying Stokes-similarity. We speculate that the slight disagreement between Cornell-1 and 2 could be the result of less accurate droplet size measurement of the old PDI instrument.

Figure 6.16 shows another comparison between Cornell-1 and 2. In this case both data sets were collected under the 5m20Hz condition. The Cornell-1 result in this case shows some periodic fluctuations at small  $r$  with period of roughly  $250\mu m$  (which is close to  $r_k$  and the measurement volume size). The origin of this oscillation is not clear to us and it only affects a few of our experiments in Cornell-1. In the other cases, either such oscillations do not occur or they have much weaker magnitude such that we could not resolve them. Those RDF's shown earlier in Fig. 6.14 were

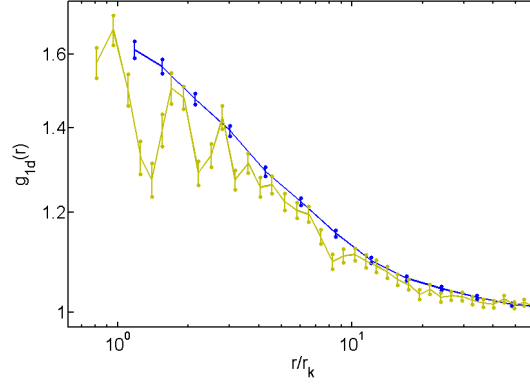


**Figure 6.16:** Comparing RDF from Cornell-1 and Cornell-2 experiments. All RDF are for  $St = 0.1 \rightarrow 0.5$ . Blue solid line is from Cornell-2, 5m20Hz run. Yellow is from Cornell-1, 5m20Hz. All plots are vertically shifted to match at  $r/r_k = 80 \sim 120$ . Note that Cornell 1 and 2 has different drop size distribution (see Fig. 4.3).

selected from these apparently clean cases.

All these observations seems to suggest that at least some of the results from Cornell-1 are questionable. This challenges our conclusions in Chapter 5. We thus stress the importance of future experiments, either of the same kind or otherwise, in corroborating our results.



# Chapter 7

## Summary and conclusions

We have described a wind tunnel experiment that allows us to study inertial particle clustering in turbulence, utilizing a novel phase Doppler interferometer (Chap. 2 and 4). We have introduced the radial distribution function (RDF) as a way of quantifying inertial particle clustering and presented some original works on foundational and practical considerations related to it (Chap. 3). These include methods of treating finite sampling size, interpretation of the magnitude of RDF and the possibility of isolating RDF signature of inertial clustering from that of large scale mixing.

In Chapter 5, we showed experimental evidence for Stokes similarity of inertial clustering. We also found that the influence of Reynolds number and gravitational settling parameter ( $S_g$ ) is weak in the range studied ( $R_\lambda \simeq 400 \sim 700$ ;  $S_g \lesssim 1$ ).

There was also evidence for other qualitative agreements between the experimental data and theory (detailed below).

We have also studied inertial clustering by comparing our experimental results with direct numerical simulation (DNS) of particle laden turbulence, and also indirectly with theory using the DNS data as a ‘bridge’ (Chap. 6). The DNS was performed mimicking key realistic conditions found in experiments, in order for these comparisons to be free of ambiguities. Good agreement among experiment, DNS and theory were found in the followings (cf. Sec. 6.2.1 and 6.2.3):

1. The RDF arising from inertial clustering is power-law like and extends to the limit of very small length scales ( $r \ll r_k$ ) for mono-disperse particles (the latter was only addressed by DNS and theory, the experiment has scale resolution limit of  $\sim r_k$  ).
2. The RDF, and thus inertial clustering, is found to show dynamical similarity with respect to particle Stokes number. The RDF is flat ( $c_1 = 0$ , no clustering) when  $St = 0$  and becomes steeper as  $St$  increases from zero.
3. For non-zero  $St$ , the RDF becomes larger than unity (signature of clustering) at length scales  $r < 10 \sim 30 r_k$ . This is found to be true for all cases (mono-disperse, bi-disperse, poly-disperse). This finding supports the understanding that inertial clustering is driven by dissipation scale fluid motions and corrobo-

rates the long standing consensus among researchers that turbulent vorticity is maximum around the scales of 10 to 20 Kolmogorov lengths ( $r_k$ ).

Apart from these, good quantitative agreement was found between DNS and the mono-disperse theory for  $St \lesssim 0.3$ . Good quantitative agreement was also found (albeit minor deviations at large  $St$ ) between DNS and experiment in the poly-disperse setting. Taken together, this implies that there is consistency between theory and experiment regarding the Stokes number scaling of mono-disperse RDF's (see Sec. 6.2.3 for details).

In Section 6.2.2, we showed, using the DNS data, that the effect of poly-dispersity is to diminish clustering. Specifically, as poly-dispersity is increased, the RDF slope is lowered and a plateau region appears below a small length scale that grows with poly-dispersity. We further found that the reduction of the slope ( $c_1$ ) becomes significant ( $\geq 10\%$ ) when  $\Delta St \simeq St_{mid}/5$ . In the same section, we also provided a mathematical relation that allows one to predict any general poly-disperse RDF given the mono-disperse and bi-disperse RDF's (Eq. 6.5).

For the case of spatial correlation between two sets of particles with different Stokes numbers, we found disagreement between theory and DNS (Sec. 6.2.6). Specifically, when comparing the bi-disperse RDF's, we found that the theory was able to predict the trend of the flattening scale,  $r_c$ , very well but fails to account for the



bottleneck effect found in the trend of  $c_1$ . Since the experiment and DNS agree on this bottleneck effect (Sec. 6.2.7), experiment and theory are thus qualitatively inconsistent. In view of that, we have proposed a corrected, first order, empirical model for the bi-disperse  $c_1$  based on empirical observation (Eq. 6.12).

In Section 6.2.4, we presented, based on DNS and experimental data, evidence for an intriguing (semi-exact) relation between the pre-exponential factor of the RDF,  $c_0$ , and the power-law exponent,  $c_1$ . This finding led us to propose an alternative form for the RDF of inertial clustering that is approximately controlled by a single parameter,  $c_1$  (see discussion around Eq. 6.8 for details).

In Section 6.2.5, using the experimental and DNS data, we showed evidence that inertial clustering becomes saturated once the Reynolds number is increased beyond a certain level ( $R_\lambda \sim 140$ ).

Finally we end this thesis by pointing out that the work presented here, like any work of science, is not without subtleties or shortcomings (see e.g. Sec. 6.3) and thus should be subjected to tests and improvements by future studies, experimental or otherwise.

# Appendix A

## Details on characterization of active grid turbulence

The turbulence generated by the present (and similar) active grid setup (cf. Sec. 4.2.1) has been carefully characterized and used for various turbulence studies [see e.g. Mydlarski and Warhaft (1996, 1998), hereafter as M&W-*year*; and Ayyalasomayajula et al. (2006)]. In M&W (1996), a similar but scaled down system (about half the size) was extensively studied to determine the performance of the active grid. It was found that the turbulence generated was slightly less isotropic ( $\sim 10\%$  less) compared to that generated by passive grids. However the anisotropy was restricted to the large scale turbulence motion and thus the flow was concluded to be well suited for studies of fine scale turbulence dynamics. It was also found that the velocity p.d.f. (probability

distribution function) is slightly non-gaussian (skewed) due to the high intensity and rapid decay of the turbulence. This was argued to be ignorable since it is very small compared to the highly non-gaussian statistics of velocity differences and derivatives in the small scale fluid motions. Other than these, the generated turbulence shows highly promising flow statistics including a clear scaling range (inertial subrange) in the spectra. Many of the results in that work were found to be in line with results of earlier studies using passive grids.

In M&W (1998), a larger active grid, identical with the present, was built and used in a wind tunnel of nearly the same cross-section as the present. The generated turbulence was found to be qualitatively similar (details in the paper) with that of the smaller system in M&W (1996) and closely follow all the trends.

Finally, the turbulent flow in the present setup was also characterized and found to be in good agreement with the aforementioned systems (Gylfason, 2006, Chap. 5).

# Appendix B

## Copyright information

The author has obtained permission for the use of each copyrighted materials this thesis. In some cases, the permission is automatically granted since the author of this thesis is also an author of the published works. Detailed copyright documentations can be found in the corresponding supplementary document submitted to the graduate school of Michigan Technological University.



# References

- Albrecht, H.-E., Borys, M., Damaschke, N., and Tropea, C. (2002). *Laser Doppler and Phase Doppler Measurement Techniques*. Springer-Verlag, Berlin.
- Aliseda, A., Cartellier, A., Hainaux, F., and Lasheras, J. C. (2002). Effect of preferential concentration on the settling velocity of heavy particles in homogeneous isotropic turbulence. *J. Fluid Mech.*, 468:77.
- Ayyalasomayajula, S., Gylfason, A., Collins, L. R., Bodenschatz, E., and Warhaft, Z. (2006). Lagrangian measurements of inertial particle accelerations in grid generated wind tunnel turbulence. *Phys. Rev. Lett.*, 97:144507.
- Balkovsky, E., Falkovich, G., and Fouxon, A. (2001). Intermittent distribution of inertial particles in turbulent flows. *Phy. Rev. Lett.*, 86:2790.
- Bec, J., Biferale, L., Cencini, M., Lanotte, A., Musacchio, S., and Toschi, F. (2007). Heavy particle concentration in turbulence at dissipative and inertial scales. *Phy. Rev. Lett.*, 98(8):084502.

- Berrut, J. P. and Trefethen, L. N. (2004). Barycentric lagrange interpolation. *SIAM Rev.*, 46:501–517.
- Brenguier, J.-L., Bourrianne, T., de Araujo Coelho, A., Isbert, J., Peytavi, R., Trevarin, D., and Weschler, P. (1998). Improvements of droplet size distribution measurements with the fast-fssp (forward scattering spectrometer probe). *J. Atmos. Ocean. Tech.*, 15:1077.
- Brucker, K. A., Isaza, J. C., Vaithianathan, T., and Collins, L. R. (2007). Efficient algorithm for simulating homogeneous turbulent shear flow without remeshing. *J. Comput. Phys.*, 225:20–32.
- Cencini, M., Bec, J., Biferale, L., Boffetta, G., Celani, A., Lanotte, A., Musacchio, S., and Toschi, F. (2006). Dynamics and statistics of heavy particles in turbulent flows. *Journal of Turbulence*, 7:N36.
- Chen, L., Goto, S., and Vassilicos, J. C. (2006). Turbulent clustering of stagnation points and inertial particles. *J. Fluid Mech.*, 553:143.
- Chuang, P., Saw, E., Small, J., Shaw, R., Sipperley, C., Payne, G., and Bachalo, W. (2008). Airborne phase doppler interferometry for cloud microphysical measurements. *Aerosol Sci. & Tech.*, 42:685–703.
- Chun, J., Koch, D. L., Rani, S. L., Ahluwalia, A., and Collins, L. R. (2005). Dynamics and statistics of heavy particles in turbulent flows. *J. Fluid Mech.*, 536:219–251.

- Collins, L. R. and Keswani, A. (2004). Reynolds number scaling of particle clustering in turbulent aerosols. *New J. Phys.*, 6:119.
- Cuzzi, J., Hogan, R., Paque, J., and Dobrovlskis, A. (2001). Size-selective concentration of chondrules and other small particles in protoplanetary nebula turbulence. *Astrophys. J.*, 546:496–508.
- Duncan, K., Mehlig, B., Östlund, S., and Wilkinson, M. (2005). Clustering by mixing flows. *Phys. Rev. Lett.*, 95:240602.
- Eaton, J. K. and Fessler, J. R. (1994). Preferential concentration of particles by turbulence. *Int. J. Multiphase Flow*, 20:169.
- Elperin, T., Kleeorin, N., L’vov, V. S., Rogachevskii, I., and Sokoloff, D. (2002). Clustering instability of the spatial distribution of inertial particles in turbulent flows. *Phys. Rev. E*, 66:036302.
- Elperin, T., Kleeorin, N., and Rogachevskii, I. (1996). Self-excitation of fluctuations of inertial particle concentration in turbulent fluid flow. *Phys. Rev. Lett.*, 77:5373.
- Falkovich, G., Fouxon, A., and Stepanov, M. G. (2002). Acceleration of rain initiation by cloud turbulence. *Nature*, 419:151.
- Falkovich, G. and Pumir, A. (2004). Intermittent distribution of heavy particles in a turbulent flow. *Phys. Fluids*, 16(7):L47.



- Geiss, S., Dreizler, A., Stojanovic, Z., Chrigui, M., Sadiki, A., and Janicka, J. (2004). Investigation of turbulence modification in a non-reactive two-phase flow. *Experiments in Fluids*, 36:344–354.
- Ghosh, S., Dávila, J., Hunt, J. C. R., Srdic, A., Fernando, H. J. S., and Jonas, P. R. (2005). How turbulence enhances coalescence of settling particles with applications to rain in clouds. *Proc. R. Soc. A*, 461:3059.
- Goto, S. and Vassilicos, J. C. (2008). Sweep-stick mechanism of heavy particle clustering in fluid turbulence. *Phys. Rev. Lett.*, 100(5):054503.
- Gylfason, A. (2006). *Particles, passive scalar and the small scale structure of turbulence*. Ph.d. dissertation, Cornell Univ., Ithaca, NY.
- Holtzer, G. and Collins, L. (2002). Relationship between the intrinsic radial distribution function for an isotropic field of particles and lower-dimensional measurements. *J. Fluid Mech.*, 459:93–102.
- Kerstein, A. R. and Krueger, S. K. (2006). Clustering of randomly advected low-inertia particles: A solvable model. *Phys. Rev. E*, 73:025302(R).
- Kolmogorov, A. N. (1941). The local structure of turbulence in incompressible viscous fluid for very large reynolds numbers. *Dokl. Akad. Nauk SSSR*, 30:299–303.
- Kostinski, A. and Shaw, R. (2001). Scale-dependent droplet clustering in turbulent clouds. *J. Fluid Mech.*, 434:389–398.

Larsen, M. L. (2006). *Studies of Discrete Fluctuations in Atmospheric Phenomena*.

Ph.d. dissertation, Michigan Tech. Univ., Houghton, MI.

Lehmann, K., Siebert, H., Wendisch, M., and Shaw, R. A. (2007). Evidence for inertial droplet clustering in weakly turbulent clouds. *Tellus. Ser. B*, 59:57.

Lumley, J. L. and Panofsky, H. A. (1964). *The Structure of Atmospheric Turbulence*. John Wiley & Sons, New York.

Makita, H. (1991). Realization of a large-scale turbulence field in a small wind tunnel. *Fluid Dyn. Res.*, 8:53–64.

Maxey, M. R. (1987). The gravitational settling of aerosol particles in homogeneous turbulence and random flow fields. *J. Fluid Mech.*, 174:441.

Maxey, M. R. and Riley, J. J. (1983). Equation of motion for a small rigid sphere in a nonuniform flow. *Phys. Fluids*, 26:883–889.

McQuarie, D. A. (2000). *Statistical Mechanics*. University Science Books, Sausalito, CA, 2nd edition.

Monin, A. S. and Yaglom, A. M. (1975). *Statistical Fluid Mechanics: Mechanics of Turbulence*. MIT Press, Cambridge, MA.

Mydlarski, L. and Warhaft, Z. (1996). On the onset of high reynolds number grid-generated wind-tunnel turbulence. *J. Fluid Mech.*, 320:331–368.

- Mydlarski, L. and Warhaft, Z. (1998). Passive scalar statistics in high-peclet-number grid turbulence. *J. Fluid Mech.*, 358:135–175.
- Pinsky, M. and Khain, A. (1997). Turbulence effects on the collision kernel. i: Formation of velocity deviations of drops falling within a turbulent three-dimensional flow. *Quart. J. Roy. Meteor. Soc.*, 123:165.
- Pinsky, M. and Khain, A. (2003). Fine structure of cloud droplet concentration as seen from the fast-fssp measurements. part ii: Results of in situ observations. *J. Appl. Meteor.*, 42:65.
- Pope, S. B. (2000). *Turbulent Flows*. Cambridge Univ. Press, Cambridge, UK.
- Reade, W. C. and Collins, L. R. (2000). Effect of preferential concentration on turbulent collision rates. *Phys. Fluids*, 12:2530.
- Saddoughi, S. G. and Veeravalli, S. V. (1994). Local isotropy in turbulent boundary layers at high reynolds number. *J. Fluid Mech.*, 268:333.
- Salazar, J. P. L. C., Jong, J. D., Cao, L., S. H. Woodward, H. M., and Collins, L. R. (2008). Experimental and numerical investigation of inertial particle clustering in isotropic turbulence. *J. Fluid Mech.*, 600:245–256.
- Saw, E. W., Shaw, R. A., Ayyalasomayajula, S., Chuang, P. Y., and Gylfason, A. (2008). Inertial clustering of particles in high-reynolds-number turbulence. *Phys. Rev. Lett.*, 100:214501.

- Shaw, R., Kostinski, A., and Larsen, M. (2002). Towards quantifying droplet clustering in clouds. *Quarterly Journal of the Meteorological Society*, 128(582):1043.
- Shaw, R. A. (2003). Particle-turbulence interactions in atmospheric clouds. *Ann. Rev. Fluid Mech.*, 35:183.
- Shinbrot, M. (1973). *Lectures on Fluid Mechanics*. Taylor and Francis, USA.
- Strogatz, S. (2001). *Nonlinear Dynamics and Chaos*. Westview Press, Cambridge, MA.
- Sundaram, S. and Collins, L. (1997). Collision statistics in an isotropic particle-laden turbulent suspension. part 1. direct numerical simulations. *J. Fluid Mech.*, 335:75–109.
- Taylor, G. (1938). The spectrum of turbulence. *Proceedings of the Royal Society of London. Series A, Mathematical and Physical Sciences*, 164(919):476–490.
- Tennekes, H. and Lumley, J. (1972). *A First Course in Turbulence*. MIT Press, Cambridge, MA.
- Villermaux, E., Innocenti, C., and Duplat, J. (2001). Short circuits in the corr-sin $\tilde{U}$ obukhov cascade. *Phys. of Fluids*, 13(1):284.
- Wang, L. P. and Maxey, M. R. (1993). Settling velocity and concentration distribution of heavy particles in homogeneous isotropic turbulence. *J. Fluid Mech.*, 256:27.

- Witkowska, A., Brasseur, J. G., and Juvé, D. (1997). Numerical study of noise from isotropic turbulence. *J. Comput. Acoust.*, 5:317–336.
- Wood, A. M., Hwang, W., and Eaton, J. K. (2005). Preferential concentration of particles in homogeneous and isotropic turbulence. *Int. J. Multiphase Flow*, 31:1220.
- Yang, T. S. and Shy, S. S. (2005). Two-way interaction between solid particles and homogeneous air turbulence: particle settling rate and turbulence modification measurements. *J. Fluid Mech.*, 526:171–216.
- Zaichik, L. I. and Alipchenkov, V. M. (2003). Pair dispersion and preferential concentration of particles in isotropic turbulence. *Phys. of Fluids*, 15:1776.